Geometrical and topological properties of CMB polarization fields

A Thesis

Submitted For the Degree of

Doctor of Philosophy

in the Faculty of Science

by

Vidhya Ganesan

Department of Physics

Indian Institute of Science

BANGALORE – 560 012

July, 2017

Declaration

I hereby declare that the work contained in this thesis titled, "Geometrical and topological properties of CMB polarization fields", is the result of research work carried out by me, in the supervision of Dr. Pravabati Chingangbam at Indian Institute of Astrophysics, Bangalore, and Dr. Prateek Sharma at Indian Institute of Science, Bangalore, under the Joint Astronomy Programme (JAP) of the Department of Physics, Indian Institute of Science, Bangalore. I further declare that this thesis has not been submitted for the award of any degree, diploma, associateship, fellowship etc. of any university or institute. In accordance to the general practice, due acknowledgements have been made wherever the work described is based on other investigations.

Vidhya Ganesan

Date:

S. R. Number: 01-07-00-10-11-11-1-08678

Department of physics,
Indian Institute of Science,
Bangalore - 560 012
India

Dedicated to my father, Ganesan
who taught me an unique and wonderful point of view
of observing the intricate mechanisms of nature

Acknowledgements

I am very thankful to my supervisor Dr. Pravabati Chingangbam for her patience and guidance. I would like to express my immense gratitude to her for everything I have learnt from her, and for helping me academically and personally in so many ways.

I would like to thank Dr. Patta Yogendran for all the interesting arguments and discussions. I also thank Dr. Changbom Park for all his insightful comments for our publications.

I am grateful to Indian Institute of Astrophysics (IIA) for providing all the facilities for my research work. I would like to thank Anish and all the people of Data center for all their help. A special thanks to all the instructors during the course work of the Joint Astronomy Programme.

I would like to express my deepest gratitude to Prof. B. P. Das. He is the sole reason that I have managed to reach this point, who persistently encouraged and made me pursue Ph.D. I thank Dr. Prateek Sharma, my official guide at Indian Institute of Science (IISc) for all his help and support. I also thank Mrs. Meena and other administrative staff of IISc for all their help. I am extremely grateful to my friend Akansha for her constant support during my stressful times. I also thank my very few but extremely valuable

friends Prasanna, Megha, Susmitha, Joby, and Priya for all their support.

Finally, a very special thanks to my parents Ganesan and Subbulakshmi, my brothers Kannan and Arun, my sister-in-laws Uma and Razmi, and my niece Anjana for all their patience and support.

List of Publications

- *Primordial non-Gaussian signatures in CMB polarization*,
  Vidhya Ganesan, Pravabati Chingangbam, K. P. Yogendran, and Changbom Park,
  J. Cosmol. Astropart. Phys. **02** 028 (2015).

- *On Minkowski Functionals of CMB polarization*,
  Pravabati Chingangbam, **Vidhya Ganesan**, K. P. Yogendran, and Changbom Park,
  Phys. Lett. B **771** pp.67-73 (2017).

- *Tensor Minkowski Functionals: first application to the CMB*,
  Vidhya Ganesan, and Pravabati Chingangbam,
  J. Cosmol. Astropart. Phys. **06** 023 (2017).

- *Tensor Minkowski Functionals for random fields on the sphere*,
  Pravabati Chingangbam, K. P. Yogendran, P. K. Joby, **Vidhya Ganesan**, Stephen Appleby, and Changbom Park,
  arXiv:1707.04386, submitted to J. Cosmol. Astropart. Phys.

Abstract

C*osmic* M*icrowave* B*ackground* (CMB) is a relic from the early Universe. It was generated due to the physical processes in the early Universe during an epoch known as the recombination or decoupling epoch. The CMB has highly uniform temperature over the entire sky but with small variations in different directions. Due to the Thomson scattering between photons and electrons and also because of the quadrupole anisotropies induced in the cosmic plasma during the decoupling epoch, the CMB is linearly polarized. The CMB radiation in each line of sight is associated with temperature (T) and polarization. The polarization can be decomposed into Stokes parameters Q/U, or E mode (E) and B mode (B) fields. Here, Q/U fields transform as spin ± 2 objects under rotation transformation while the E/B fields remain invariant. The fluctuations observed in CMB is due to the quantum fluctuations generated during the inflationary phase, which is a period of exponential expansion moments after the Big Bang in the early Universe. The CMB fluctuations will have statistical properties similar to this primordial fluctuations only for the linear evolution of fluctuations. Statistical observable can be used to capture the morphological properties of the CMB fluctuations. Then these morphological properties can be studied in relation to the parameters describing the physical mechanisms of

the inflationary phase. In this research work, we use the geometrical and topological observables to study the CMB polarization fields and we also introduce a novel statistical observable for the analysis of CMB fields.

The models about the inflationary phase predict that the P*robability* D*istribution* F*unction* (PDF) of primordial fluctuations are close to the Gaussian distribution but with small deviation. The information about the exact form of deviation in the PDF of primordial fluctuation will be encapsulated in the CMB fields. We investigate the local type non-Gaussian features in the CMB polarization fields, which is parametrized by $f_{\rm NL}$. We derive the analytic expression for the PDF of any general local type non-Gaussian field such as the T and E fields of CMB, and also for the local type non-Gaussian polarization intensity (I_P) constructed from local type non-Gaussian Q and U fields. We use the analytic expression and simulations of local type non-Gaussian CMB fields, namely T, E and I_P, and study the deviation in their PDF relative to the Gaussian PDF. We found from the analytic expression that the non-Gaussian deviation in the PDF of the T and E fields are proportional to $(f_{\rm NL}\sigma)$ while that of I_P field is proportional to $(f_{\rm NL}\sigma)^2$. The numerical calculations show that the non-Gaussian deviation in the PDF of E field is similar to that of the T field. While the non-Gaussian deviation corresponding to the I_P field has smaller amplitude and large error bars in comparison to that of T field. This analysis was repeated using the geometrical and topological observables, namely S*calar* M*inkowski* F*unctionals* (SMFs) and Betti numbers of fields. These observables capture different morphological features of a given field. The results obtained using these observables are similar to those from the PDF of the fields. Hence from the theoretical point of view, these results imply that the E field can provide an independent constraint on $f_{\rm NL}$ similar to the T field. Further, the results also show that when

the I_P field is used independently for such analysis, it cannot provide any statistically significant information. In the realistic scenario, the observational data contains instrumental systematics which will lead to the reduction in the statistical significance of the above results.

The CMB polarization is usually analyzed using the E/B fields as they are scalar fields. We investigate the theoretical aspects of using the Q/U fields as a complementary analysis of CMB polarization. We show that the variance of Q/U and its gradient fields are invariant under rotation transformation, and hence the invariance of the SMFs of a Gaussian Q/U fields. However, this statement breaks down for incomplete sky. Then we studied the non-Gaussian deviation in Q/U fields constructed from the simulations of local type non-Gaussian E field. These simulations use the same $x-y$ coordinates along each line of sight. We found that its amplitude is about an order of magnitude lower than that of T field and has different shape. This finding will be useful for distinguishing different non-Gaussian signals in the observational data from future experiments. Further, we studied the effect of the presence of primordial tensor perturbation, which is parametrized by r, on the SMFs of Q/U and I_P fields, and the number density of singularities in I_P field. Here, a singularity is a point on the CMB field where $I_P = 0$. We found that the amplitude of SMFs of these fields are sensitive to the presence of primordial tensor perturbation and it decreases with r. We also show that the number density of singularities in I_P field decreases with r. This finding will be useful for the searches of primordial tensor perturbation in the future experiments. The instrumental systematics in the observational data will decrease the statistical significance of the above results.

We introduce T*ensor* M*inkowski* F*unctionals* (TMFs), which are tensor generalization of Minkowski Functionals, as a new statistical observable for the analysis of CMB data. Since these are tensor quantities, they are capable of capturing more morphological properties in a given field than their scalar counterparts. We have developed a code, referred as TMFCode, to compute the TMFs for any general field on an Euclidean plane. In order to apply the TMFs, specifically $W_2^{1,1}$ which is a tensor of rank 2, to CMB fields which lies on a 2-d spherical surface, we map each point on the sphere with a point on a plane using stereographic projection. The code computes $W_2^{1,1}$, and then the net anisotropy (β) and net orientation (α) of the structures are estimated. We investigated the numerical error in this computation due to pixelization. We found the error in β increases with the increasing curvature of the boundaries of the structure. The error in α is negligible when the structures are completely unoriented with each other and it increases as the structures become more and more aligned with each other. We present the numerical calculation of the systematic variation of α and β with the threshold value for the simulated Gaussian and isotropic CMB T and E fields. We found that the value of β shows a characteristic variation with the threshold value while α is flat. We show that according to the standard model, $\beta = 0.62$ for T and $\beta = 0.63$ for E, where the values are corrected for pixelization. The value of α is one for both the fields, which is as expected for an isotropic field.

We applied $W_2^{1,1}$ for the analysis of PLANCK data as an illustration of its application. The instrumental systematics and the gravitational lensing due to large scale structure affects the morphological features of the CMB fields. We study the effect of these factors on the value of α and β using the simulations of CMB frequency bands, namely 44GHz and 70GHz provided in PLANCK data,

which contains the respective instrumental characteristics. We found that the percentage difference in α and β due to these factors are less than 2% and it significantly increases the size of their error bars. We use the CMB simulations corresponding to the frequency band 44GHz as the basis for testing the consistency of different PLANCK data sets with theoretical expectations. We estimated the deviation in α and β for the foreground cleaned CMB maps namely SMICA, COMMANDER, SEVEM and NILC corresponding to full mission, half mission 1, half mission 2, half ring 1 and half ring 2 provided in the PLANCK data. These calculations showed that β is consistent with the standard model within $2-\sigma$ for all data sets, except the T map of NILC half mission 2 which has slightly higher deviation. We found the values of α for T map of different data sets to be in excellent agreement with the standard model within $1.2-\sigma$. The deviation in α of E map of all data sets are higher than $3-\sigma$ except the SMICA full mission data. Further, α for E map corresponding to the half mission 1 of all data sets showed consistently higher deviation of $5-\sigma$. These results imply that the structures in the E map has an extent of alignment with each other. This alignment could be cosmological or due to instrumental systematics. Since we are comparing the PLANCK maps which are obtained by co-adding all frequency bands with that of the simulations with the instrumental characteristics of a specific frequency band, namely 44GHz, the instrumental systematics is more probable reason for the alignment measured in E map.

Contents

List of Tables

List of Figures

Chapter 1

Introduction

1.1 Cosmic Microwave Background and the historical developments

The C*osmic* M*icrowave* B*ackground* (CMB) is a thermal background radiation observed in all directions of the sky. The discovery of CMB paved the way for major advancements in the field of cosmology. It firmly established the hot Big Bang model. The statistical properties of the CMB fluctuations gave credibility to the idea of "cosmic inflation," which proposes a brief period of exponential expansion of the Universe in the moments following the Big Bang. Further development of experiments which can accurately measure CMB will allow us to test cosmological models, develop fundamental theory of inflation, and it may eventually reveal the nature of fundamental laws at high energies which cannot be achieved by our present day particle accelerators.

In 1950s, there were two competing theories for the origin of the Universe. One was the Steady State theory, according to which our Universe is static

and existed in the current state for eternity [1]. An alternative model was the Big Bang theory which suggested that the Universe began from a hot and dense initial state, then it gradually expanded and cooled [2]. Edwin Hubble's discovery of expansion of the Universe [3] supported the latter model. However at the time, the model was not completely accepted among the scientific community. Meanwhile, George Gamow and collaborators had shown as early as 1948 that the Big Bang model predicts the existence of a remnant thermal background radiation [4, 5, 6]. Finally in 1965, Arno Penzias and Robert Wilson detected this background radiation, with a temperature of about 3K [7], which was inferred to be the CMB by Robert Dicke *et al.* (1965) [8]. Penzias and Wilson received the Nobel Prize for physics in 1978 for the discovery.

According to the Big Bang model, the light nuclei like deuterium, helium, and lithium were created in the very early phase of the Universe through the B*ig* B*ang* N*ucleosynthesis* (BBN) [9, 10]. While the nuclei heavier than lithium originated from the stellar nuclear reactions or supernova explosions. The calculations of mass abundances using BBN gives 25% of helium-4 (^{4}He), 0.01% of deuterium (^{2}H), and small traces of helium-3 and lithium-7 (^{3}He,^{7} Li). These predictions were later tested through observations of astronomical objects, such as dwarf galaxies and quasars, where primordial abundances are preserved since it has not yet been significantly altered by stellar nucleosynthesis. The abundance measurement of deuterium and helium using these observations were found to be in good agreement with the theoretical expectations [11], which provided a very strong confirmation of the Big Bang model. But the abundance in lithium shows a discrepancy between the prediction and observation, which is referred to as Lithium problem [12, 13, 14, 15]. This discrepancy can only be resolved through a better understanding of BBN and stellar nucleosynthesis.

The CMB observations so far has shown that it is very isotropic. The scale of the causal horizon at the epoch when the CMB was generated subtends an angle which is less than a degree on the sky. However, the CMB photons coming from the direct opposite points of the sky, which are separated by 180°, also have similar temperature. This is referred to as the horizon problem. Similar to this example, the CMB observations also lead to other paradoxes like the flatness problem and magnetic monopole problem. In order to explain such paradoxes the idea of inflation was introduced. The inflation model was proposed by Alan Guth in 1981 [16] and it was developed further in [17, 18, 19, 20]. During the inflationary phase, a causally connected region was blown up to the size of the observable Universe. This resolved the paradoxes.

The CO*smic* B*ackground* E*xplorer* (COBE) satellite was launched aboard a Delta rocket in 1989 to investigate the CMB radiation. It carried three instruments, namely, D*ifferential* M*icrowave* R*adiometer* (DMR), F*ar*-I*nfra*Red A*bsolute* S*pectro photometer* (FIRAS) and D*iffuse* I*nfra*R*ed* B*ackground* (DIRBE). The FIRAS instrument measured the spectrum of CMB radiation to be a black body distribution [21]. The DMR instrument measured temperature fluctuations about the order of 10^{-5} with 7° sky resolution [22]. The DIRBE instrument surveyed the diffuse infrared sky [23]. COBE's principal investigators, George Smoot and John Mather, received Nobel Prize for physics in 2006. This project is regarded as the starting point for precision cosmology. A number of ground and balloon based experiments were used to measure the temperature anisotropies at different scales. A list of such experiments is FIRS, ATCA, MSAM, Python, Saskatoon experiment, CAT, TRIS, APACHE, BAM, QMAP, SuZIE, TOCO, BOOMERanG, MAXIMA etc.

The D*egree* A*ngular* S*cale* I*nterferometer* (DASI), a telescope located in

Antarctica, first detected the gradient component of CMB polarization anisotropies known as E mode polarization [24]. The curl component is called the B mode polarization. DASI was also the first to detect the second and third acoustic peaks of the power spectrum of CMB temperature [25, 26, 27]. The first acoustic peak of temperature was detected by TOCO, BOOMERanG and MAXIMA [28, 29]. The ground based experiment CBI measured the small scale anisotropies in temperature and E mode [30, 31]. It also obtained the detailed power spectrum of E mode. The B mode polarization due to the primordial origin is yet to be detected. Secondary effects such as gravitational lensing, foreground also has an impact on the CMB. The B mode polarization induced due to the gravitational lensing was first measured by SPTpol [32]. This was later confirmed by POLARBEAR [33], PLANCK [34] and BICEP2 [35]. A list of a few polarization anisotropy experiments is: POLAR, COMPASS, QUaD, BICEP, AMiBA etc.

The *Wilkinson Microwave Anisotropy Probe* (WMAP) was launched from Florida in 2001, which succeeded the COBE mission. This was followed by the PLANCK mission by ESA in 2009. These missions have provided us with high precision temperature maps, and polarization map [36, 37]. Overall, the CMB observations so far are consistent with the standard model of cosmology and cosmic inflation. But a few anomalies have been seen in the CMB temperature that are not consistent with the standard model [38]. A few of these anomalies are: low variance at lower resolutions, hemispherical asymmetry, point parity asymmetry, mirror parity asymmetry, and a large cold spot. Since these were observed by both WMAP and PLANCK experiments, these anomalies are not likely to be due to the systematics in these experiments. The analysis of large scale polarization anisotropies in the PLANCK team's final data release, will either increase or decrease the significance of these detected anomalies.

1.2 Thermal history of the Universe

In this section, we describe the stages in the evolution of the Universe. The early Universe was in a plasma state, which consisted of different elementary particles in thermal equilibrium. As the Universe expanded, the temperature of the cosmic plasma also dropped. Further, the wavelength of photons also gets stretched and hence red-shifted. Therefore, the cosmic time line can be specified by either temperature or redshift.

The early Universe went through a phase of cosmic inflation, an exponential expansion, about 10^{-36} seconds after Big Bang. This was driven by the inflaton scalar field, that filled the Universe at the time. Quantum fluctuations were generated during this phase. The scale of these fluctuations gets stretched outside the Hubble horizon scale, cH^{-1}, due to the exponential expansion. After it crosses the horizon, the amplitude of the fluctuations remain constant in time. Once the inflationary phase is over, the Universe starts to decelerate and the fluctuations again enter the Hubble horizon. These form the primordial seeds which eventually evolve into the anisotropies observed in the CMB and the large scale structures in the Universe. Further, the inflaton energy density condense to form the standard model particles through a process known as "reheating". This also results in the transfer of fluctuations, from the initial energy density into the energy density of these particles.

When the temperature of the cosmic plasma was above 200GeV, the Universe was made up of quarks and gluons, which were unbounded and free, and dark matter. Around this time, it is expected that dark matter decoupled from the plasma. The elementary particles that mediate weak interactions, namely $W^{\pm}$ and Z bosons, were massless and also the weak interactions were

as strong as the electromagnetic interactions. As the temperature dropped below 200GeV, the electroweak symmetry was broken and the Higgs mechanism gave masses to the elementary particles. Therefore, the weak interactions became weak. At temperatures below 100MeV, corresponding to the redshift of $z > 10^{12}$, hadrons begin to form. When the temperature falls to about 1.4MeV, the weak interaction rate becomes slower than the expansion rate and the neutrinos decouple from the plasma. Neutrinos follow Fermi-Dirac distribution with a temperature decreasing with time due to the expansion. Hence there must be a neutrino background with a temperature of about 1.95K. However, this background has not been detected till now. At a slightly lower temperature, electrons and positrons annihilated each other. The photons were heated due to this annihilation process, while the neutrinos were not affected as they had already decoupled from the plasma. Therefore, the photons will be at a higher temperature than the neutrinos.

At a later stage, the cosmic plasma mainly consisted of photons, electrons, protons, and a few neutrons. The number of photons with energies larger than the binding energy of deuterium (2.2MeV) were sufficient so as to prevent the survival of any deuterium nuclei that formed. Only when the temperature dropped below 0.08MeV, deuterium nuclei was able to survive. Then the `BBN`, described in the previous section, lead to the formation of light nuclei, He^4, with traces of deuterium, He^3, and Li^7 in the Universe.

When the temperature dropped to slightly above 0.3eV, and redshift of $z > 1100$, the cosmic plasma consisted of photons, electrons and protons in thermal equilibrium. These particles were interacting with each other through Thomson and Coulomb scattering. There were sufficient number of photons in the plasma, which were energetic enough to destroy any neutral hydrogen

that formed. Once the temperature falls below 0.3eV, protons and electrons combine to form the neutral hydrogen. The photons then decoupled from the plasma and the Universe became transparent to it. The CMB photons have black body distribution with a temperature decreasing with time due to the expansion. This is the CMB radiation that appears to come from a spherical surface around the observer which is known as the last scattering surface. This surface is the farthest we can see in the Universe. The phase of the Universe during which the photons decoupled from the cosmic plasma is referred to as the recombination era. The subsequent epochs like the reionization era will also have an impact on the CMB radiation.

1.3 Polarization of CMB

The fact that the Thomson scattering during the recombination phase can polarize the CMB radiation was realized in 1968 [39]. If we consider an unpolarized light ray traveling along the x axis, which gets scattered from an electron and gets deflected along the y axis (refer to Fig. 1.1). The incident light ray has equal intensity in y and z axes. Since the outgoing direction is along y axis, the intensity along z axis is transmitted while that along the y axis is not transmitted. Therefore, the scattered light ray is linearly polarized with intensity along the z direction.

In a realistic situation, the incoming radiation is incident on an electron from all directions. Consider an isotropic incoming radiation, which in the present case we consider to be along two directions x and z axis. The outgoing ray will have intensity along x axis which comes from the incoming radiation along the z direction while the intensity along z axis comes from the incoming

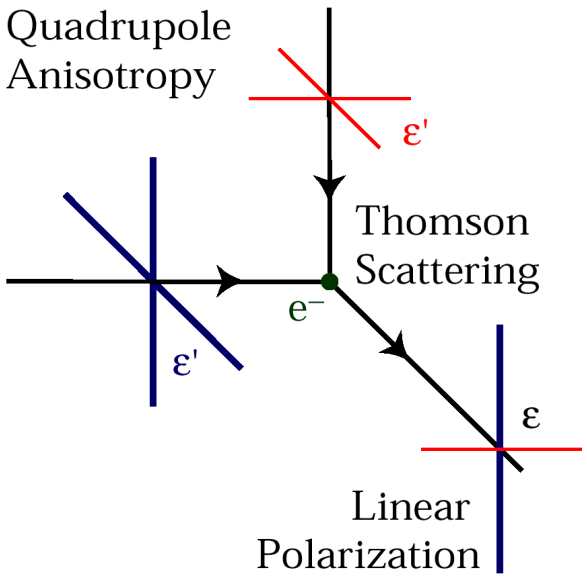

Figure 1.1: Image showing the Thomson scattering of radiation with an electron. Horizontal line is the x direction, vertical line is the z direction and other line is the y direction. Image from http://web.stanford.edu/$\sim$schurch/quad_science.html.

radiation along the x direction. So the outgoing ray is unpolarized. In the case of dipole anisotropic pattern, which indicates that the temperature along $\pm$ x direction are different while the temperature along $\pm$ y direction are the same. Now the intensity along z axis of the outgoing ray is average from $\pm$ x direction, and hence the scattered radiation is again unpolarized. Finally, let us consider the case of quadrupolar anisotropic pattern, which implies that the temperature along the x direction is different from the z direction. The intensity of scattered ray along the x axis is due to the incident radiation along the z direction, while that along z axis is due to the incident radiation along x direction. Due to the distinct temperature along x and z directions, the outgoing radiation is linearly polarized. Therefore, the Thomson scattering generates polarization only when the incoming radiation has quadrupole anisotropy.

The condition for polarization of CMB is Thomson scattering between the photons and electrons, and the quadrupole anisotropy in the cosmic plasma. Before the recombination era, the interaction rate of photons and electrons were so high that it erased any anisotropies present in the cosmic plasma. While there were no Thomson scatterings after the recombination phase. Hence the CMB photons cannot get polarized before or after the recombination. However during the recombination period, quadrupole anisotropies were generated which lead to the polarization of CMB [40, 41, 42, 43, 44]. Therefore, only about 10% of CMB radiation are polarized. Since polarization is a weak signal, even though the existence of CMB polarization was known as early as 1968, its actual detection was made by DASI much later in 2002 after a lot of experimental efforts [45, 46, 47, 48, 49, 50]. Further, this polarization will get modified during the epoch of reionization and also due to gravitational lensing by the large scale structures.

The polarization map obtained by PLANCK satellite confirms the standard cosmological model [51]. Further, the angular power spectrum at small scales of the polarization map has been used to better constrain the parameters of standard cosmological model. Currently, an important goal in cosmology is the detection of B mode polarization. In 2014, BICEP2 collaboration reported a significant detection of B mode polarization [52]. Later, the collaboration of BICEP2 and PLANCK team revealed that it was due to the contamination from dust [53]. The experiments on CMB polarization are still in the evolving stage. While anisotropies in the temperature component has been accurately measured and its consistency with the standard model has been extensively tested. Just as the CMB temperature has revolutionized our ideas about the early Universe, the information contained in the polarization is expected

to lead to important advancement in our understanding. The future experiments such as C*osmic* Or*igins* E*xplorer* (COrE) and P*olarized* R*adiation* I*maging* and S*pectroscopy* M*ission* (PRISM) are being planned to study the polarization anisotropies.

1.4 Statistical tools

The statistical properties of CMB anisotropies contain information about the physical mechanism of inflationary phase and also about the later epochs. In order to capture different features in the CMB anisotropies, different statistical observables are required. Then the various aspects, such as the non-Gaussian features, of CMB fluctuations can be studied in relation to the physical mechanism which induced these fluctuations.

Important statistical tools used for analyzing cosmological data are power spectrum, bispectrum, and Minkowski Functionals. Genus, which is one of the Minkowski Functionals has been used extensively for analyzing large scale structure of the Universe and CMB [54, 55, 56, 57, 58, 59]. A more generalized form known as Minkowski Functionals was introduced into cosmological literature in [60], where it was applied to galaxy surveys. Then it was used to study statistical properties of large scale structure and CMB [61, 62, 63, 65, 66, 67, 68, 69]. Further, it was applied to the observed CMB data in order to constrain the extent of primordial non-Gaussianity [70, 71, 72, 73, 74, 75, 76]. It has been applied to study other aspects of CMB, namely, to identify traces of residual foreground contamination [77, 78], cold spot anomaly [79] and modified gravity theories through lensing of CMB [80]. A topological observable known

as "Betti numbers", was introduced as a statistical observable for the analysis of large-scale structures [81, 82, 83]. It was then used to study different non-Gaussian signals in CMB [84, 85].

Tensor Minkowski Functionals [86, 87] are tensor generalization of Minkowski Functionals. Since these quantities have more degrees of freedom, these are very useful for quantifying different morphological features in a field. This has been used to study a variety of phenomena such as neuronal cells in the brain [88], ice crystals in Antarctica [89], and galaxies and clusters of galaxies in our Universe [90]. This is a new statistical observable that we will be introducing for the analysis of CMB.

1.5 Aim of the thesis

The aim of the thesis is to study the statistical properties of primordial fluctuations using the geometrical and topological statistical tools on the polarization of CMB radiation. This study was conducted along the following lines of investigation:

- CMB temperature has been extensively used for the analysis of non-Gaussian features in the primordial fluctuations and to constrain the extent of non-Gaussianity. We expect that the inclusion of polarization data will lead to better constrain on non-Gaussianity. We investigate the non-Gaussian features in the E mode polarization, using probability distribution function, geometrical, and topological properties, to investigate and quantify its ability to constrain primordial non-Gaussianity. The PLANCK team analysis which included the polarization data confirmed our expectations.

- The analysis of CMB polarization is usually done using E and B mode polarization. We study the prospect of analysis using the Stokes parameters Q and U. Due to their spin-2 nature, which implies that they transform under rotation transformation, they are not widely used for CMB analysis. We theoretically investigate the affect of rotation transformation on the geometrical and topological properties of Q and U. Further, we study the affect due to the various aspects of primordial fluctuations, such as the presence of primordial non-Gaussianity and tensor perturbation, on the geometrical and topological properties of Q and U.

- We introduce a new statistical tool, Tensor Minkowski Functionals which are extensions of the Scalar Minkowski Functionals, for the analysis of CMB. This can capture features such as net anisotropy and net orientation in the structures of a field. We develop a numerical code which can estimate these features for a given field. We estimate the expected values for net anisotropy and net orientation of CMB fields according to the standard model of cosmology. As an illustration of its application, we do a simple study to test the consistency of various PLANCK data sets with the standard model of cosmology.

The thesis is organized as follows:

- A brief introduction about CMB was presented in this chapter.

- Aspects of CMB anisotropies are given in Chapter 2, where we describe the CMB observables, origin of perturbations, and the primordial non-Gaussian fluctuation.

- In Chapter 3, the derivation and the numerical analysis of probability distribution of CMB observables are shown and its implications are discussed.

- An introduction to topology and different topological properties of a random field are described in Chapter 4.

- The numerical analysis of non-Gaussian features in the E mode polarization using the geometrical and topological observables and its implications are discussed in Chapter 5.

- The theoretical aspects of the prospect of the usage of the Stokes parameters of CMB for the analysis of primordial fluctuation are studied in Chapter 6.

- Chapter 7 introduces a new statistical tool, Tensor Minkowski Functionals, for the analysis of CMB. We have developed a code to compute these quantities. The numerical method used by this code is described. Then the theoretical prediction for the net anisotropy and net orientation according to the standard model of cosmology is presented.

- The results from the analysis of PLANCK data sets is presented and its implications are discussed in Chapter 8.

- The conclusion and the future course of work are discussed in Chapter 9.

Chapter 2

Anisotropies in Cosmic Microwave Background

2.1 CMB observables

The CMB radiation is specified by temperature and polarization along each line of sight. The temperature is expressed as

$$\frac{\Delta T}{T_0}(\hat{n}) = \frac{T(\hat{n}) - T_0}{T_0}, \tag{2.1}$$

where $T(\hat{n})$ is the temperature along each direction, and T_0 is the average temperature over the entire sky. While the polarization is described in terms of the Stokes parameters Q, U and V. Since the Thomson scattering during the recombination era cannot induce circular polarization, the quantity V is taken to be zero. The values of Q and U along any given direction, $\hat{n}$, on the sphere are defined in the spherical coordinate system. Further, these transform

under rotation by an angle α about the line of sight as

$$\begin{pmatrix} Q' \\ U' \end{pmatrix} = R(2\alpha) \begin{pmatrix} Q \\ U \end{pmatrix} = \begin{pmatrix} \cos 2\alpha\ Q + \sin 2\alpha\ U \\ -\sin 2\alpha\ Q + \cos 2\alpha\ U \end{pmatrix}. \tag{2.2}$$

Hence the transformation of complex quantities $Q + iU$ and $Q - iU$ can be written as

$$(Q \pm iU)'(\hat{n}) = e^{\mp 2i\alpha}(Q \pm iU)(\hat{n}). \tag{2.3}$$

These are spin -2 and spin 2 objects respectively. Further, all of the above described quantities can be expressed in terms of spin weighted harmonic functions as

$$\begin{aligned} \frac{\Delta T}{T_0}(\hat{n}) &= \sum_{\ell m} a^T_{\ell m} Y_{\ell m}(\hat{n}), \\ (Q + iU)(\hat{n}) &= \sum_{\ell m} a_{2,\ell m} Y_{2,\ell m}(\hat{n}), \\ (Q - iU)(\hat{n}) &= \sum_{\ell m} a_{-2,\ell m} Y_{-2,\ell m}(\hat{n}). \end{aligned} \tag{2.4}$$

The CMB polarization can be re-expressed in terms of gradient and curl component, which are known as E mode and B mode respectively. These are scalar quantities or spin 0 objects. The distinction between the E and B component of a polarization field is in the property of the pattern in the polarization orientation surrounding a particular point. The E mode polarization field has an orientation which is diverging from the point while the B mode polarization field has an orientation which is curling around the point. Further, the B mode polarization changes sign under parity transformation while E mode is invariant .

The spin of an object can be lowered or raised using the spin lowering and

spin raising operators, ∂ and $\bar{\partial}$ respectively, which are given by

$$
\begin{aligned}
{}_{s+1}f(\theta,\phi) &= \partial\ {}_sf(\theta,\phi) = -(\sin\theta)^s \left[\frac{\partial}{\partial\theta} + \frac{i}{\sin\theta}\frac{\partial}{\partial\phi}\right]\left[(\sin\theta)^{-s}\ {}_sf(\theta,\phi)\right], \\
{}_{s-1}f(\theta,\phi) &= \bar{\partial}\ {}_sf(\theta,\phi) = -(\sin\theta)^{-s} \left[\frac{\partial}{\partial\theta} - \frac{i}{\sin\theta}\frac{\partial}{\partial\phi}\right]\left[(\sin\theta)^{s}\ {}_sf(\theta,\phi)\right],
\end{aligned}
\tag{2.5}
$$

where ${}_sf(\theta,\phi)$ is a field and the subscript 's' indicates the spin of the field. The E mode and B mode fields can be constructed by using the above operators on the quantities $Q \pm iU$ as follows

$$
\begin{aligned}
E(\hat{n}) = \bar{\partial}^2(Q+iU)(\hat{n}) &= \sum_{\ell m}\left(\frac{\ell+2}{\ell-2}\right)^{1/2} a^E_{\ell m}Y_{\ell m}(\hat{n}), \\
B(\hat{n}) = \partial^2(Q-iU)(\hat{n}) &= \sum_{\ell m}\left(\frac{\ell+2}{\ell-2}\right)^{1/2} a^B_{\ell m}Y_{\ell m}(\hat{n}),
\end{aligned}
\tag{2.6}
$$

where $a^E_{\ell m}, a^B_{\ell m}$ are related to $a_{2,\ell m}, a_{-2,\ell m}$ as

$$
\begin{aligned}
a^E_{\ell m} &= -(a_{2,\ell m} + a_{-2,\ell m})/2, \\
a^B_{\ell m} &= i(a_{2,\ell m} - a_{-2,\ell m})/2.
\end{aligned}
\tag{2.7}
$$

The CMB polarization can also be expressed in terms of polarization intensity and polarization angle. The polarization intensity is invariant under coordinate transformation while the polarization angle varies. We will represent the polarization intensity as I_P and the mean shifted polarization intensity, $\tilde{I}_P$, as

$$
\tilde{I}_P = I_P - \langle I_P \rangle. \tag{2.8}
$$

The power spectrum of the CMB fields are calculated as

$$C_\ell^{XY} = \frac{1}{2\ell+1} \sum_{m=-\ell}^{\ell} a_{\ell m}^{X} a_{\ell m}^{*Y}, \tag{2.9}$$

where $X, Y = T, E, B$. Since the B mode field has odd parity, the cross correlation of B mode with either E mode or temperature vanishes. Hence the CMB fluctuations are described by four power spectra, which are the auto correlation of T, E, B and the cross correlation between T and E. A convenient form of power spectrum, D_ℓ, can be defined as

$$D_\ell^{XY} = \frac{\ell(\ell+1)}{2\pi} C_\ell^{XY}. \tag{2.10}$$

The Fig. 2.1 shows the plots of D_ℓ for all the four power spectrum.

The H*ierarchical* E*qual* A*rea iso*L*atitude* Pix*elization* (HEALPix)[1] [107] is used for pixelization of CMB maps. A base map is constructed with twelve pixels on three rings of constant latitude as shown in top left map in the Fig. 2.2. The resolution is defined in terms of the parameter $N_{\rm side}$, which is the number partitions on the side of a pixel of the base map required to build a map of higher resolution. The base map corresponds to the $N_{\rm side} = 1$. The maps in Fig. 2.2 shows the construction of higher resolution map for $N_{\rm side} = 2$ (top right map), 4 (bottom right map), and 8 (bottom left map). For example, to obtain a map of $N_{\rm side} = 4$ the sides of each of the pixels in the base map are partitioned into 4 and hence a single pixel in the initial map will now contain 16 pixels. The pixel centers lie on a ring of constant latitude (θ). The rings in the equatorial zone, defined by $-2/3 < cos\theta < 2/3$, contain equal number of pixels

[1] http://healpix.sourceforge.net

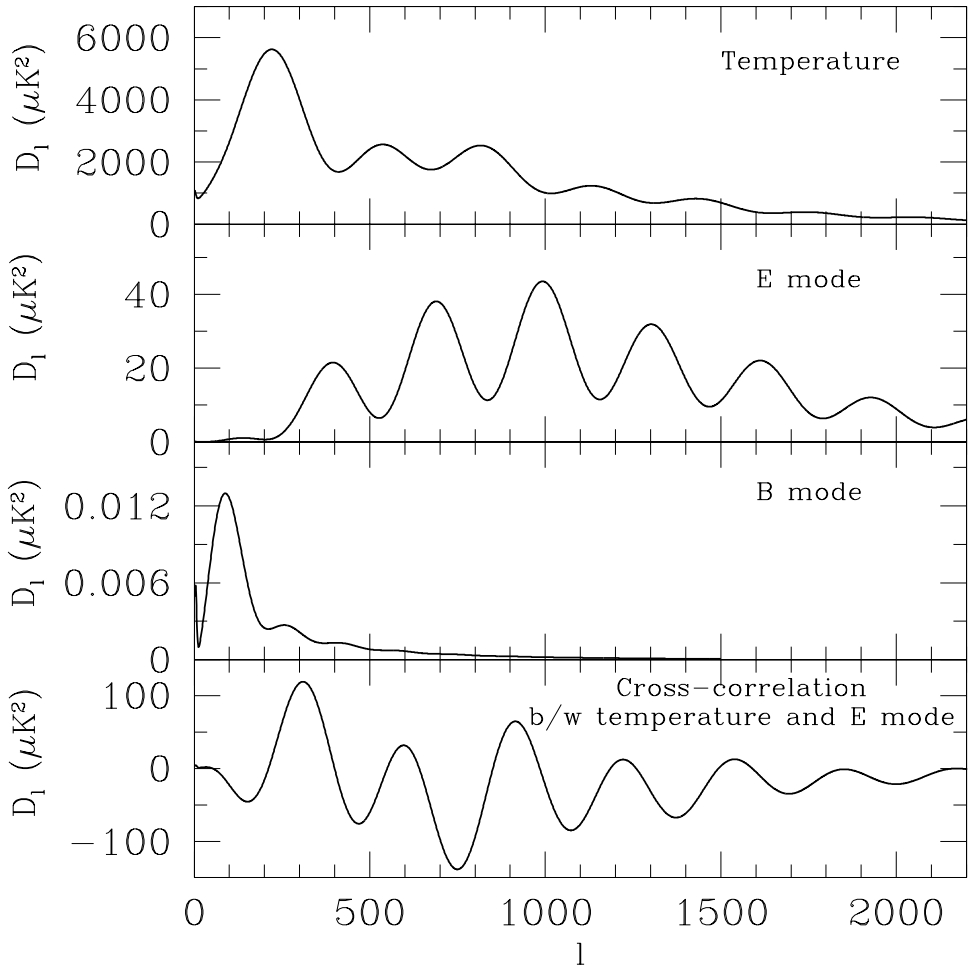

Figure 2.1: Plots in the top three panels show the power spectra, D_ℓ defined in Eq. 2.10, for temperature, E mode, and B mode in units of μK^2. The bottom panel shows the same for the cross correlation between temperature and E mode.

of $4N_{\rm side}$. While other rings contain varying number of pixels, which increases with its increasing distance from the poles. The total number of pixels, denoted as $N_{\rm pix}$, for a higher resolution map is $12N_{\rm side}^2$. Each of these pixels have equal area of $\pi/3N_{\rm side}^2$. Further for the Q/U maps, a coordinate system needs to be defined at each point on the sphere. In the `HEALPix` convention, x direction

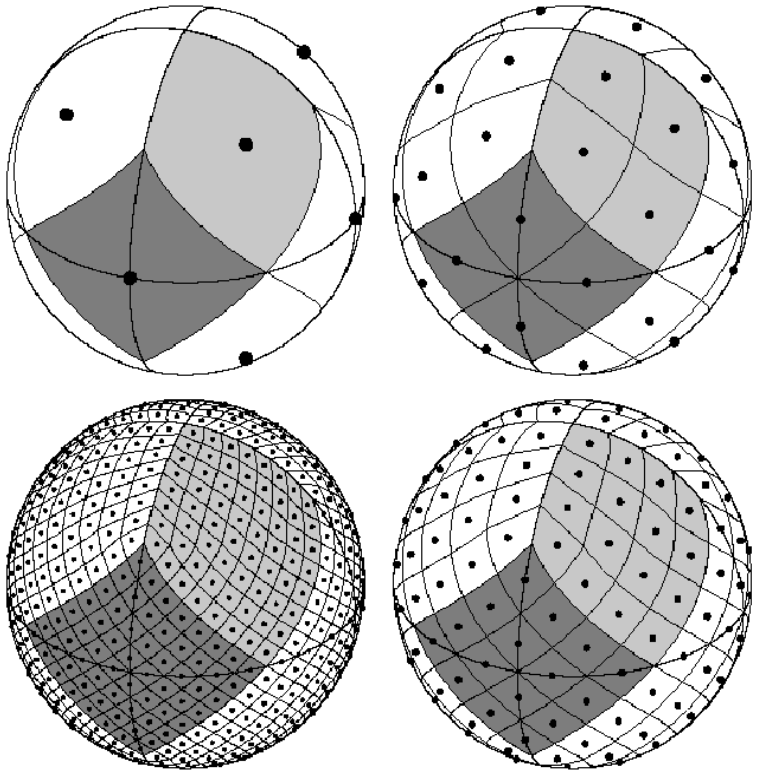

Figure 2.2: Pixelization scheme used by `HEALPix` package. Images show the pixelization for different resolution, with $N_{\text{side}} = 1$ (top left map), 2 (top right map), 4 (bottom right map), and 8 (bottom left map). Image from K. M. Gorski *et al.* (2005), `HEALPix`: A Framework for High-Resolution Discretization and Fast Analysis of Data Distributed on the Sphere - Scientific Figure on ResearchGate, https://www.researchgate.net/1801816_fig3_Fig-4-Orthographic-view-of-the-HEALPix.

at each point is defined such that it is pointing towards the south and the y direction such that it is pointing towards the east. For the analysis of Q/U maps, we use the `HEALPix` convention.

2.2 Origin of CMB fluctuations

The metric of a homogeneous and isotropic Universe is described by the F*riedmann* R*obertson* W*alker* (FRW) metric given by

$$ds^2 = -dt^2 + a^2(t)\gamma_{ij}dx^i dx^j, \tag{2.11}$$

where $a(t)$ is the scale factor. Here, γ_{ij} is the metric of 3D space with constant curvature k, which in polar coordinates (r, θ, ϕ) is given by

$$\gamma_{ij} = \begin{pmatrix} \frac{1}{1-kr^2} & 0 & 0 \\ 0 & r^2 & 0 \\ 0 & 0 & r^2 \sin^2\theta \end{pmatrix}.$$

According to the standard model of cosmology, the Universe is dominated by cosmological constant (Λ) or dark energy and cold dark matter. It is also referred as ΛCDM model. It is described by the cosmological parameters: Λ, cold matter density (Ω_m), Hubble parameter at the present time ($H_0 = 100\ h$ Mpc/kms^{-1}), amplitude of primordial fluctuations (A_s), spectral index of primordial fluctuations (n_s), and optical depth of reionization era (τ). Here, Ω is the ratio of energy density (ρ) and critical energy density (ρ_c), which is energy density corresponding to the flat Universe, $H_0 = \dot{a}(t_0)/a(t_0)$, and the subscript '0' represents that the value corresponds to the present time. The definition of A_s and n_s is given in Eq. 2.17 of the next section. The evolution of the scale factor and the various content of the Universe are related

by the Einstein equation, known as the Friedmann equations given by

$$\left(\frac{\dot{a}}{a}\right)^2 = \frac{8\pi G}{3}\rho - \frac{k}{a^2} + \frac{\Lambda}{3}, \tag{2.12}$$

$$\frac{\ddot{a}}{a} = -\frac{4\pi G}{3}(\rho + 3p) + \frac{\Lambda}{3}, \tag{2.13}$$

where, p is the pressure.

Since the observed CMB fluctuations are small, perturbation theory is used to describe the evolution of primordial fluctuations. The metric perturbations are classified into three types scalar, vector and tensor. At first order, these perturbations evolve independent of each other and hence can be studied independently. The physical processes which induce scalar perturbations, does not induce vector or tensor perturbations, and vice versa. This statement is a manifestation of the decomposition theorem. The general perturbed metric is given by

$$ds^2 = -(1+2\Psi)dt^2 + a^2(t)[(1-2\Phi)\gamma_{ij} + 2h_{ij}]dx^i dx^j, \tag{2.14}$$

where Ψ and Φ are Bardeen potentials, and h_{ij} is a divergenceless, traceless, symmetric tensor. The Bardeen potentials signify the scalar perturbations while h_{ij} describes the tensor perturbations. For a perfect fluid containing non-relativistic particles, the Bardeen potentials are related to each other and it refers to the Newtonian gravitational potential. The density fluctuations can generate scalar perturbations while it is not capable of generating tensor perturbation. The vector perturbations are not included in the above equation, as any such perturbations decays out rapidly. The tensor perturbation gives rise to the gravitational waves generated during the inflationary era. The extent to

which the tensor perturbations are present relative to the scalar perturbations is parameterized by tensor-to-scalar ratio, r.

The polarization of CMB during recombination era can be sourced by primordial density fluctuations and primordial gravitational waves. In both of these cases, the mechanism through which the CMB is polarized is Thomson scattering and the only distinction between the two is in the cause of quadrupole anisotropies. In the case of density fluctuations, velocity gradients in the cosmic plasma create the quadrupole anisotropies which results in the polarization. In the case of gravitational waves, the photons get redshifted or blueshifted as they travel on the metric perturbed by the gravitational waves. This frequency shift has a quadrupolar angular dependence which gives rise to the polarization in CMB. Specifically, the primordial gravitational waves results in B mode polarization of CMB.

The Boltzmann equation is used to describe the evolution of perturbations in each of the elementary particles photons, neutrinos, electrons, protons and also the dark matter, which is given by

$$\frac{df(\vec{x},\vec{p},t)}{dt} = C[f], \tag{2.15}$$

where f is the distribution of the species in phase space, which is a function of its position ($\vec{x}$), momentum ($\vec{p}$) and t, and C is the relevant interaction terms for each species. The above Boltzmann equation for each species, together with the Einstein equation are solved simultaneously, in order to find the distribution of CMB temperature and polarization. These equations are numerically solved using the publicly available package C*ode for* A*nisotropies*

in the Microwave Background (CAMB)[2] [91] provided by Antony Lewis and Anthony Challinor. This code gives the radiation transfer function $\Delta_l^X(r)$ for $X = T, E, B$, which encapsulates the information about the evolution from the primordial perturbation to the CMB fluctuations for different scales. It also computes the power spectrum of CMB fields, which in terms of radiation transfer function is given by

$$C_\ell^{XY} = \int dk k^2 P_\Phi(k) |\Delta_\ell^X(k) \Delta_\ell^Y(k)|, \tag{2.16}$$

for $X, Y = T, E, B$. Here, $P_\Phi(k)$ is the power spectrum of primordial gravitational potential given by

$$P_\Phi(k) = A_s \left(\frac{k}{k_s}\right)^{n_s - 1}, \tag{2.17}$$

with $k_s = 0.002 \text{Mpc}^{-1}$, as predicted by the inflation model

2.3 Non-Gaussian fluctuations

In literature, there are a variety of inflation models that have been proposed [16, 19, 20, 92, 93, 94]. Currently observations [95, 96] support the range of inflation models, according to which the probability distribution of primordial fluctuations are very close to Gaussian. Different classes of models have their own characteristic non-Gaussian deviation [97, 98, 99]. They provide us with a method, which will help in isolating the inflation model that accurately describes our Universe.

[2] http://camb.info/

We focus on a particular type of non-Gaussian distribution known as local type non-Gaussianity [100, 101, 102, 103]. We construct non-Gaussian primordial gravitational potential Φ, which is defined in Eq. 2.14, as a function of conformal distance by adding a non-linear term as

$$\Phi(r) = \Phi_{\rm L}(r) + f_{\rm NL}\Phi_{\rm NL}(r), \tag{2.18}$$

where $\Phi_{\rm NL}$ is defined as

$$\Phi_{\rm NL}(r) = (\Phi_{\rm L}(r))^2 - \left\langle (\Phi_{\rm L}(r))^2 \right\rangle, \tag{2.19}$$

and $f_{\rm NL}$ is a measure of the extent of non-Gaussianity in the field. The quantity Φ sets the initial conditions for the theoretical calculation of CMB temperature and polarization fluctuations. Hence the information about primordial non-Gaussianity will be encoded in the CMB fluctuations.

The analysis of CMB observations so far indicate that the value of f_{NL} are very small [76], hence the second term in Eq. 2.18 is much smaller in comparison to the first term. However foreground contamination, instrumental noise, and secondary sources of anisotropy also generate non-Gaussian features in the CMB. Cosmic variance also introduces some non-Gaussianity due to the uniqueness of the observed CMB sky. Due to this factor the search for primordial non-Gaussianity is a challenging task.

The search for primordial non-Gaussianity requires statistical observables, which are capable of detecting the presence of any non-Gaussian features in the CMB fields. A few examples of statistical observables in Fourier space are power spectrum, bispectrum, and trispectrum. While the statistical observables such

as Betti numbers, Minkowski functionals, Tensor Minkowski Functionals are defined in real space, whose description is given in Chapter. 4. Since each of these statistical observables get affected differently by different non-Gaussian sources, they are useful for distinguishing the non-Gaussian signal of primordial origin from those of other sources. In order to study these statistical observables and to probe the non-Gaussianity in CMB, one requires high resolution simulations of CMB containing non-Gaussian features. Here, we describe a method first proposed by Liguori *et al.* [104] and then developed further in [105, 106] to simulate CMB maps with local type non-Gaussian features. The following are the step by step procedure, to simulate a single realization corresponding to a given cosmological model:

- Fine shells of conformal distances $\mathbf{r} = [r_1, r_2, \ldots r_n]$ are constructed from the origin to the last scattering surface.

- The covariance matrix ($\mathbf{P}_{\Phi,\ell}$) is a n x n matrix, whose components are radial correlations of multipole moment $\Phi_{\mathrm{L},\ell m}(r)$ (spherical harmonic coefficients of Φ_{L}) between different conformal distances. The $(r_1, r_2)^{\mathrm{th}}$ component is estimated as

$$\langle \Phi_{\mathrm{L},\ell_1 m_1}(r_1) \Phi^*_{\mathrm{L},\ell_2 m_2}(r_2) \rangle = \frac{2}{\pi} \delta^{\ell_2}_{\ell_1} \delta^{m_2}_{m_1} \int dk k^2 P_\Phi(k) j_{\ell_1}(k r_1) j_{\ell_2}(k r_2), \quad (2.20)$$

  where δ^i_j is the Kronecker delta function, and j_ℓ is the spherical Bessel function of order ℓ.

- The vector $\mathbf{\Phi}_{\mathrm{L},\ell m}(\mathbf{r}) = [\Phi_{\mathrm{L},\ell m}(r_1), \Phi_{\mathrm{L},\ell m}(r_2), \ldots \Phi_{\mathrm{L},\ell m}(r_n)]$ is estimated as

$$\mathbf{\Phi}_{\mathrm{L},\ell m}(\mathbf{r}) = \mathbf{P}^{1/2}_{\Phi\ell} . \mathbf{g}, \quad (2.21)$$

where $\mathbf{g}$ is a complex vector. The components of $\mathbf{g}$ are independent Gaussian random variables with zero mean and unit variance.

- The spherical harmonic transform, $\Phi_{\rm L}(r)$, is obtained using the multipole moments $\Phi_{{\rm L},\ell m}(r)$.

- Square the linear term $\Phi_{\rm L}(r)$ and subtract its variance as shown in Eq. 2.19, to obtain the corresponding non-linear term $\Phi_{\rm NL}(r)$.

- Spherical harmonic transform the non linear term $\Phi_{\rm NL}(r)$, to obtain the corresponding multipole moments $\Phi_{{\rm NL},\ell m}(r)$.

- The linear term of spherical harmonic coefficients of the map are obtained as

$$a^X_{{\rm L},\ell m} = \frac{(-i)^\ell}{2\pi^2}\int dk k^2 \Phi_{{\rm L},\ell m}(k)\Delta^X_\ell(k), \tag{2.22}$$

  where $\Delta^X_\ell(k)$ is the radiation transfer function, in Fourier space, of temperature for $X = T$ and E mode for $X = E$. It is obtained using the `CAMB` package for a given cosmological model. Similar to the calculation of linear term, the non-linear term of spherical harmonic coefficients ($a^X_{{\rm NL},\ell m}$) are obtained by replacing the linear term, $\Phi_{{\rm L},\ell m}$, with the non-linear term $\Phi_{{\rm NL},\ell m}$.

- The spherical harmonic coefficients of a map with local-type non-Gaussianity, $f_{\rm NL}$, can be calculated as

$$a^X_{\ell m} = a^X_{{\rm L},\ell m} + f_{\rm NL}\cdot a^X_{{\rm NL},\ell m}. \tag{2.23}$$

- Finally, the temperature and E mode maps are constructed, by spherical

harmonic transform of $a^T_{\ell,m}$ and $a^E_{\ell,m}$ respectively.

We use the publicly available simulations provided by Elsner and Wandelt[3], for the non-Gaussian studies in the subsequent chapters. The resolution of these map is fixed by the maximum multipole $\ell_{\rm max} = 1024$ and $N_{\rm side} = 512$. These maps were simulated with the cosmological parameters obtained from `WMAP5+BAO+SN` data[4]: $\Omega_\Lambda = 0.721$, $\Omega_c h^2 = 0.1143$, $\Omega_b h^2 = 0.02256$, $A_{s(0.002{\rm Mpc}^{-1})} = 2.457$ x 10^{-9}, $h = 0.701$, $n_s = 0.96$ and $\tau = 0.084$. We use the `HEALPix` package, which also provides various codes for processing of the `CMB` maps, for the pixelization and the analysis of these maps. In order to study the behavior of a given field at different scales, we use Gaussian smoothing described by either smoothing angle, θ_s, or FWHM. These are related to each other as $\theta_s = {\rm FWHM}/\sqrt{8{\rm ln}2}$.

[3] http://planck.mpa-garching.mpg.de/cmb/fnl-simulations

[4] http://lambda.gsfc.nasa.gov/product/map/dr3/parameters.cfm

Chapter 3

Probability distribution function of local type non-Gaussian CMB fields

3.1 Introduction

The primordial non-Gaussian features in CMB temperature field has been studied extensively [73, 108, 109, 75]. Here, we extend such studies to the CMB polarization fields. We use P*robability* D*istribution* F*unction* (PDF) of the field as it is a simple and direct observable. We derive analytic expressions for PDF of Gaussian and local type non-Gaussian CMB fields such as temperature, E mode, and polarization intensity. We numerically compute and analyze the non-Gaussian deviation in the PDF of CMB fields. In the analysis, issues in observational data such as incomplete sky coverage and instrumental systematics are neglected. The non-Gaussian signal in CMB fields is studied relative to the

cosmic variance.

This chapter is organized as follows. In Sec. 3.2, we derive the analytic formula for PDF of CMB fields. In Sec. 3.3, the results from the numerical calculations of non-Gaussian deviation, which is obtained using the simulations of Gaussian and non-Gaussian CMB maps, are presented. Finally, we summarize and discuss the implication of these results in Sec. 3.4.

3.2 Analytic formula for PDF

The statistical properties of primordial fluctuations, Φ defined in Eq. 2.14, and CMB fluctuations are the same only when the evolution of fluctuations during the intermediate epochs are linear. If linear evolution of fluctuation is assumed then this would imply that the PDF of temperature and E mode fields will be Gaussian when the PDF of Φ is Gaussian. In the alternative case, where the PDF of Φ is non-Gaussian, then these fields will also have similar non-Gaussian distribution. Similarly, the Q and U fields will also have PDF same as the Φ, which will then decide the PDF of the polarization intensity field, I_P.

3.2.1 PDF of local type non-Gaussian field

In this section, we derive the PDF of a general local type non-Gaussian field, which is parametrized by $f_{\rm NL}$. Let X denote a field having the Gaussian PDF with zero mean. Then a local type non-Gaussian field Y can be constructed as

$$Y = X + f_{\rm NL}(X^2 - \sigma^2), \tag{3.1}$$

where $\sigma^2 = \langle X^2 \rangle$. Consider $P(X), P(Y)$ to be the PDF of random variables X, Y respectively.

Let $F(Y)$ be some arbitrary function, then its expectation value can be written as

$$\begin{aligned} \langle F \rangle &= \int dX P(X) F\left(X + f_{\rm NL}(X^2 - \sigma^2)\right) \\ &= \int dX P(X) \int \frac{dk}{\sqrt{2\pi}} e^{ik\left(X + f_{\rm NL}(X^2-\sigma^2)\right)} \tilde{F}(k). \end{aligned} \tag{3.2}$$

In the second step, we have expressed the function F in terms of its Fourier transform. Expanding the exponential term in terms of $f_{\rm NL}$, we get

$$\langle F \rangle = \int dX P(X) \int \frac{dk}{\sqrt{2\pi}} e^{ikX} \left(1 + ikf_{\rm NL}(X^2 - \sigma^2) - k^2 f_{\rm NL}^2 (X^2 - \sigma^2)^2 + \dots\right) \tilde{F}(k). \tag{3.3}$$

Simplification of 0^{th} order term:

$$\begin{aligned} &\frac{1}{\sqrt{2\pi}} \int dk \int dX \; P(X) \; e^{ikX} \; \tilde{F}(k) \\ &\quad = \frac{1}{\sqrt{2\pi}} \int dk \int dX \; \frac{1}{\sqrt{2\pi}\sigma} \; e^{-X^2/2\sigma^2} \; e^{ikX} \; \tilde{F}(k) \\ &\quad = \frac{1}{\sqrt{2\pi}} \int dk \; \tilde{F}(k) \; e^{-k^2\sigma^2/2} \\ &\quad = \frac{1}{\sqrt{2\pi}} \int dk \;\; e^{-k^2\sigma^2/2} \frac{1}{\sqrt{2\pi}} \int dY e^{-ikY} F(Y) \\ &\quad = \frac{1}{\sqrt{2\pi}\sigma} \int dY \;\; e^{-Y^2/2\sigma^2} \; F(Y) \\ &\quad = \int dY P^0(Y) F(Y), \end{aligned}$$

$$P^{(0)}(Y) = \frac{1}{\sqrt{2\pi}\sigma} e^{-\frac{Y^2}{2\sigma^2}}. \tag{3.4}$$

Similarly, the first and second order correction term are obtained to be

$$P^{(1)}(Y) = -\frac{f_{\rm NL}\sigma}{\sqrt{2\pi}\sigma} e^{-\frac{Y^2}{2\sigma^2}} \frac{Y(Y^2-3\sigma^2)}{\sigma^3}, \tag{3.5}$$

$$P^{(2)}(Y) = \frac{(f_{\rm NL}\sigma)^2}{\sqrt{2\pi}\sigma} e^{-\frac{Y^2}{2\sigma^2}} \frac{(Y^6-11Y^4\sigma^2+23Y^2\sigma^4-5\sigma^6)}{2\sigma^6}. \tag{3.6}$$

Now Eq. (3.3) can be written as

$$\langle F \rangle = \int dY F(Y) \left(P^{(0)}(Y) + P^{(1)}(Y) + ... \right). \tag{3.7}$$

The PDF of non-Gaussian field Y is given by

$$P(Y) = P^{(0)}(Y) + P^{(1)}(Y) + P^{(2)}(Y) + \ldots, \tag{3.8}$$

where the first term is the PDF of Gaussian part of Y and the higher order terms give corrections to the zeroth order. Hence, substituting these terms in Eq. 3.8, we get

$$P(Y) = \frac{1}{\sqrt{2\pi}\sigma} e^{-\frac{Y^2}{2\sigma^2}} - \frac{f_{\rm NL}\sigma}{\sqrt{2\pi}\sigma} e^{-\frac{Y^2}{2\sigma^2}} \frac{Y(Y^2-3\sigma^2)}{\sigma^3} \tag{3.9}$$

upto first order correction. The non-Gaussian deviation in the PDF is defined as

$$\frac{\Delta P}{P^{(0),max}} = \frac{P(Y) - P^{(0)}(Y)}{P^{(0),max}}. \tag{3.10}$$

By substituting the analytic formula, Eq. (3.9), in the above equation, we get

$$\frac{\Delta P}{P^{(0),max}} = -f_{\rm NL}\sigma e^{-\frac{Y^2}{2\sigma^2}} \frac{Y(Y^2-3\sigma^2)}{\sigma^3}. \tag{3.11}$$

3.2.2 PDF of polarization intensity field

Here, we calculate the PDF of polarization intensity. Let us consider X and Y to be two independent random variables. These two variables can be imagined to form a two dimensional space, where each point is specified by these two random variables and also has an associated probability. Then X, Y is just one way of naming the points on the space. It can also be expressed in terms of R and θ, given by

$$R = \sqrt{X^2 + Y^2}, \quad \tan\theta = \frac{Y}{X}. \tag{3.12}$$

The total probability of an infinitesimal area ($dRd\theta$ or $dXdY$) remains invariant in both of the coordinate system, hence

$$P(R,\theta)dRd\theta \equiv P(X)P(Y)dXdY, \tag{3.13}$$

where $X = R\cos\theta$ and $Y = R\sin\theta$.

Case 1. X and Y have Gaussian PDF:

Gaussian PDF for X and Y are substituted in Eq. 3.13, then all the terms are expressed in terms of R and θ, and finally it is integrated over θ, as follows

$$\begin{aligned}
P(R,\theta)dRd\theta &= \frac{1}{\sqrt{2\pi}\sigma} e^{\frac{-X^2}{2\sigma^2}} \frac{1}{\sqrt{2\pi}\sigma} e^{\frac{-Y^2}{2\sigma^2}} dXdY \\
P(R,\theta)dRd\theta &= \frac{1}{2\pi\sigma^2} e^{\frac{-R^2}{2\sigma^2}} dRRd\theta \\
\int d\theta P(R,\theta)dR &= \frac{1}{2\pi\sigma^2} \int d\theta \; Re^{\frac{-R^2}{2\sigma^2}} dR \\
P^{(0)}(R)dR &= \frac{R}{\sigma^2} e^{-\frac{R^2}{2\sigma^2}} dR,
\end{aligned} \tag{3.14}$$

where $P^{(0)}(R) = \int d\theta P(R,\theta)$, the superscript (0) indicates that it is zeroth

order and $R \subset [0, \infty)$. The above form of PDF is known as Rayleigh distribution.

Case 2. X and Y have local type non-Gaussian PDF:
We use $P(X) = P^{(0)}(X) + P^{(1)}(X) + P^{(2)}(X) + \ldots$ in Eq. 3.1 for PDF of X and Y, where $P^{(0)}(X)$, $P^{(1)}(X)$ and $P^{(2)}(X)$ are given by Eqs. (3.4), (3.5) and (3.6) respectively. These are then substituted in Eq. (3.13) to obtain the PDF for non-Gaussian R. Progressing similar to the previous case, we get

$$P(R) = \frac{R}{\sigma^2} e^{-\frac{R^2}{2\sigma^2}} \left(1 + \frac{f_{\rm NL}^2 \sigma^2}{16\sigma^6}(5R^6 - 66R^4\sigma^2 + 184R^2\sigma^4 - 80\sigma^6) + \ldots\right). \tag{3.15}$$

The first order correction $P^{(1)}(X)$ is proportional to odd power of X, hence the PDF of R does not receive any contribution at first order in $f_{\rm NL}\sigma$.

The polarization intensity, I_P, is a field similar to R and hence will have the similar PDF as R for both the Gaussian and non-Gaussian cases. The non-Gaussian deviation in the PDF of polarization intensity is given by

$$\frac{\Delta P}{P^{(0),max}} = \frac{f_{\rm NL}^2 \sigma^2}{16\sigma^6} e^{-\frac{R^2}{2\sigma^2}} \left(5R^6 - 66R^4\sigma^2 + 184R^2\sigma^4 - 80\sigma^6\right). \tag{3.16}$$

From the expressions in Eq. (3.11) and Eq. (3.16), we expect the non-Gaussian deviation of polarization intensity to be much smaller in comparison to that of E mode field.

3.3 Non-Gaussian deviation of the PDF

We present the numerically calculated non-Gaussian deviation in temperature, E mode, and polarization intensity fields in this section. We use simulation

of Gaussian and local type non-Gaussian CMB fields provided by Elsner and Wandelt (see Sec. 2.3 for a description of the simulation of data).

The temperature and E mode fields are constructed with $f_{\rm NL} = 10$, and smoothed with Gaussian smoothing angle, $\theta_s = 20'$. The non-Gaussian deviation in the PDF of these fields are expected to have the form in Eq. (3.11), whose characteristics such as the amplitude and RMS of distribution depend on the physical processes in the recombination era and the evolution of fluctuations in the later epochs. The plot of PDF and non-Gaussian deviation, which are average over 1000 realizations, are shown in Fig. 3.1. The Gaussian and non-Gaussian PDF are shown in upper panels, while the difference between these two, ΔP, divided by the amplitude of the Gaussian PDF, $P^{(0),\rm max}$, are given in the lower panels. We find that the shape of the non-Gaussian deviation follows the form given by Eq. (3.11). We observe that the non-Gaussian deviation of temperature and E mode fields show similar amplitudes.

The linear and non-linear part of the non-Gaussian map, used for the calculations in Fig. 3.1, are constructed from a single realization. This leads to the cancellation of significant part of the cosmic variance, while only the sample variance due to the higher order non-Gaussian term is retained which is shown in the bottom panels of Fig. 3.1. We can estimate the full cosmic variance by calculating

$$\Delta P_{i,j}(X) = P_i(X) - P_j^{(0)}(X), \tag{3.17}$$

where $\Delta P_{i,j}$ is the difference between the PDF of $i^{\rm th}$ realization of non-Gaussian field and the $j^{\rm th}$ realization of Gaussian field. There are 1000x1000 different (i, j) combination of PDFs. The average of the scaled PDF difference, $\Delta P_{i,j}(X)/P^{(0),\rm max}$, over the i's and j's will be same as the mean value in the

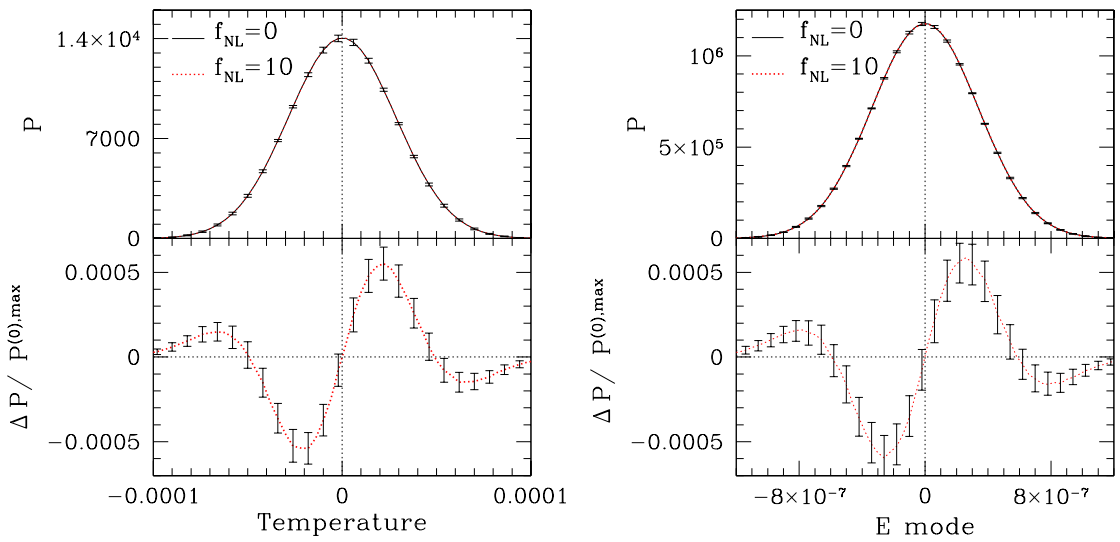

Figure 3.1: Upper panels show the PDF for temperature fluctuations (left panel) and E mode (right panel) with smoothing angle $\theta_s = 20'$. The lower panels show the corresponding non-Gaussian deviations. These are obtained by averaging over 1000 simulations of CMB. Error bars are the sample variance calculated using these simulations.

lower panels of Fig. 3.1. While we expect the sample variance to increase considerably. The non-Gaussian deviation calculated using this method is shown in Fig. 3.2. We observe that the error bars in this case are about two orders of magnitude larger than the previous case.

In order to calculate the non-Gaussian deviation in the real data, a corresponding Gaussian map is needed. The Gaussian maps can be generated by randomizing the phase of $a_{\ell m}$'s while maintaining a constant amplitude. In this statement, we assume the smoothing angle to be small enough so that the temperature or E mode map are made up of a large number of $a_{\ell m}$'s, then the central limit theorem would be applicable since the $a_{\ell m}$'s are uncorrelated in this case. The non-Gaussian deviation of the observed CMB map can be

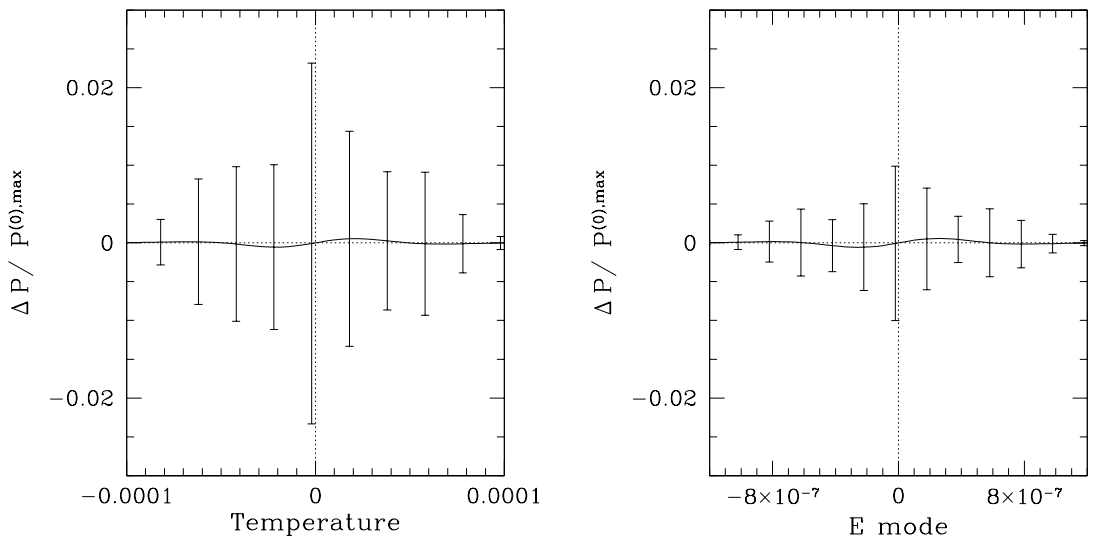

Figure 3.2: The non-Gaussian deviation in PDF, $\Delta P/P^{(0),\max}$, for temperature (left panel) and E mode (right panel). Error bars are the sample variance from 1000x1000 different combination of $\Delta P_{i,j}(X)$ given in Eq. (3.17).

computed by using the PDF obtained by averaging over many Gaussian maps. Further, the error bars can be estimated by dividing this map into many regions.

The PDF of I_P when the Q and U fields are Gaussian distributed, is given in the last line of Eq. (3.14). The procedure we follow to construct an I_P map is as follows: we first Gaussian smooth the E mode map, transform into Q, U maps and then the I_P map is computed. The tensor-to-scalar ratio, r, is assumed to be zero in this case. The numerically computed PDF of I_P is shown in the left panel of Fig. 3.3. This corresponds to the Gaussian distributed E mode field. We note that the shape of PDF computed are in good agreement with Eq. (3.14).

In order to investigate the effect on I_P due to the presence of tensor perturbation, we plot the PDF of I_P in the right panel, which includes B mode with tensor-to-scalar ratio of $r = 0.2$ with the smoothing angle same as the left panel. In this case, the E mode and B mode fields both are Gaussian smoothed, transformed into Q, U maps, and then the I_P map is constructed. We find that the amplitude of the PDF is lower when the tensor perturbations are included and this effect becomes noticeable at large smoothing angles. For the calculations in Fig. 3.3, we use the CMB simulations with the cosmological parameters obtained from the PLANCK data [111].

The PDF of I_P becomes nearly Gaussian in shape when the Gaussian smoothing is performed on the I_P field itself. This is due to the central limit theorem. As the smoothing is a linear process, the order of the non-Gaussian deviation which is about $(f_{\rm NL}\sigma)^2$ remains unaltered. The PDF of $\tilde{I}_P$ and the corresponding non-Gaussian deviation are shown in Fig. 3.4, where the I_P field is first computed, the smoothing process is performed on it, and then $\tilde{I}_P$ is calculated by subtracting the mean. Here, the tensor perturbations are not included and the non-Gaussian calculations corresponds to $f_{\rm NL} = 10$. The amplitude of non-Gaussian deviation is an order of magnitude lower than the temperature and E mode, while the error bars are twice as large. For the calculations using the polarization intensity in the subsequent chapters, we use $\tilde{I}_P$ with smoothing performed on I_P.

3.4 Discussion

We investigated the primordial local type non-Gaussian features that are imprinted in the CMB polarization using their PDF. Analytic expressions for the PDF of Gaussian and local type non-Gaussian CMB fields were obtained. We

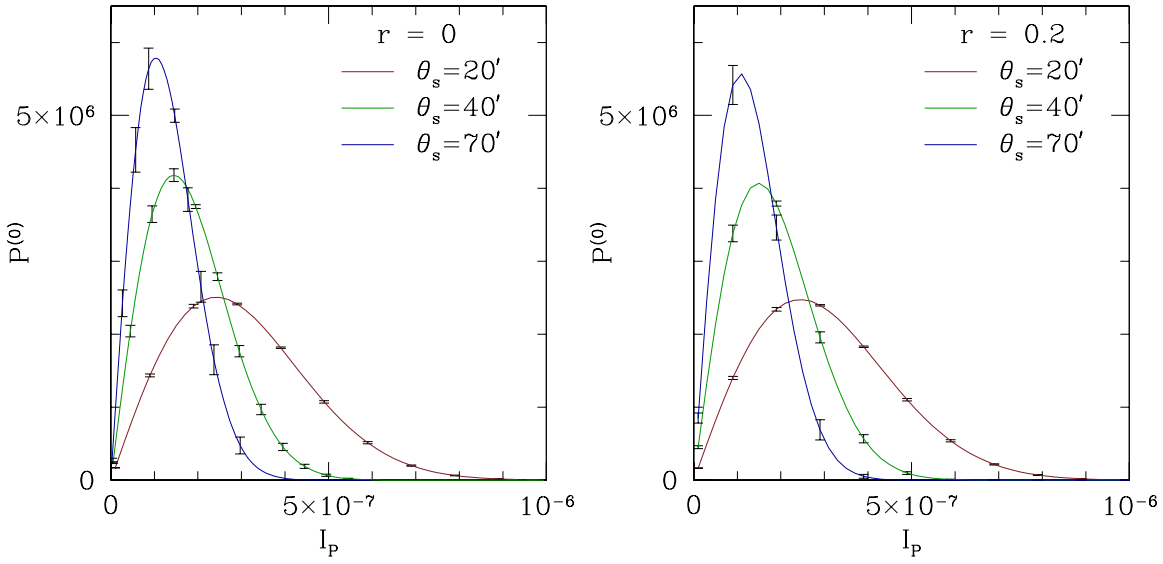

Figure 3.3: *Left panel:* PDF of I_P using the Gaussian distributed E mode, which is smoothed for various smoothing angles θ_s. This case assumes the tensor-to-scalar ratio r to be zero. *Right panel:* PDF of I_P which includes B mode with $r = 0.2$. The corresponds to the Gaussian distributed E mode and B mode, where each of these fields are smoothed. These plots are average over 1000 realization of simulated CMB fields. Error bars are sample variances from these simulations.

analyzed the non-Gaussian deviation of the PDF for E mode and polarization intensity fields in relation to the temperature field.

From the analytic expressions, we find that the non-Gaussian deviation of the PDF for E mode and temperature is about $(f_{\rm NL}\sigma)$ while for polarization intensity it is about $(f_{\rm NL}\sigma)^2$. The numerical computation of the non-Gaussian deviation showed that their shape, amplitude and size of error bars for temperature and E mode are same. While for the polarization intensity field, the amplitude is about an order of magnitude smaller and the error bars are twice as large compared to that of temperature or E mode field. From the theoretical

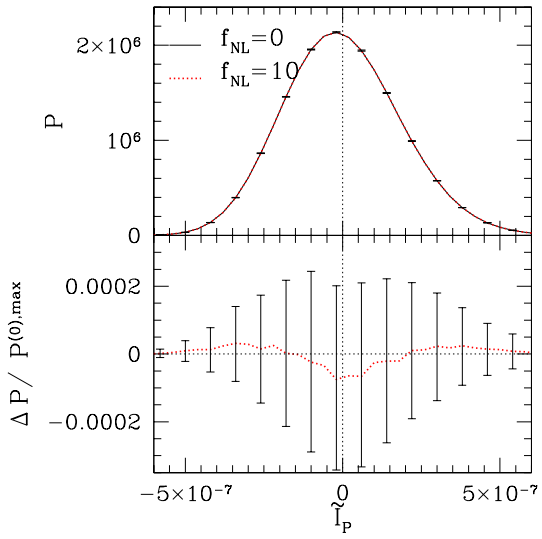

Figure 3.4: *Upper panel:* PDF of $\tilde{I}_P$ using E mode field with the Gaussian distribution and the non-Gaussian distribution with $f_{\rm NL} = 10$, where I_P map is smoothed. *Lower panel:* Non-Gaussian deviation of $\tilde{I}_P$.

perspective, these analysis indicates that the E mode field is capable of providing an independent and equally powerful constraint on $f_{\rm NL}$ as the temperature field, while the polarization intensity field is not very useful for such analysis. But as we have neglected issues related to observational data, this will reduce the usefulness of E mode field in constraining $f_{\rm NL}$. The PLANCK collaboration obtained tighter constraint on the local type non-Gaussianity, $f_{\rm NL}$, using both the temperature and polarization data [75]. But the inclusion of polarization did not lead to tight enough constraint on $f_{\rm NL}$ as our calculations suggested because of the high noise levels in the polarization data from the observation.

Chapter 4

Geometrical and topological properties of a random field

4.1 What is Topology?

Topology is the study of geometrical properties and spatial relations of a mathematical object, that remains unaltered by the continuous change of shape or size. These properties are preserved under the action of deformation, twisting, and stretching of the object. While tearing or gluing changes its topology. For example, topologically a circle is equivalent to a square or a triangle. A circle can be stretched to form the corners and then the rest of the points can be straightened out to form the sides of either a triangle or a square. Example of two objects which are not topologically equivalent to a circle are straight line and the figure 8. In order to transform a circle into a straight line segment, the circle needs to be teared at a point and then straightened out. But as tearing changes the topology, the straight line segment is topologically distinct from

the circle. Similarly for the figure 8, where we are required to glue the two points of a circle, which again changes the topology of the object.

One of the historical problem which laid the foundations of topology was *Königsberg bridge puzzle* by Euler. The city of Königsberg in Prussia (now at Kaliningrad, Russia) which was located on both sides of the Pregel river. It included two islands which were connected to each other, and to the two mainlands of the city by seven bridges, which is illustrated in the left image of Fig. 4.1. The problem was to devise a path through the city that would cross each of these bridges only once. Euler published a paper entitled *"Solutio problematis ad geometriam situs pertinentis"* which translates into *"The solution of a problem relating to the geometry of position"* [112]. The only important information in the problem are the connections between the land masses. Hence the problem can be reformulated in terms of abstract terms, each land mass can be replaced with a vertex or node and each bridge with an edge. This mathematical structure is known as graph which is shown in the right image. The shape of the graph can be deformed in any way without effecting its basic structure. The only significant factor is the number of edges connecting any pair of vertices or nodes.

Euler observed that when one enters a land mass by a bridge, as any bridge can only be crossed once hence he/she needs to leave by another bridge. Hence each land mass except the ones which are the starting or ending point, must have even number of bridges. However in the above problem all the land masses have odd number of bridges and hence it is impossible to strategize a path which satisfies the condition required by the problem. The number of edges connected to a node is known as its degree. Euler showed that the condition to traverse such a path is that the graph should have exactly zero or

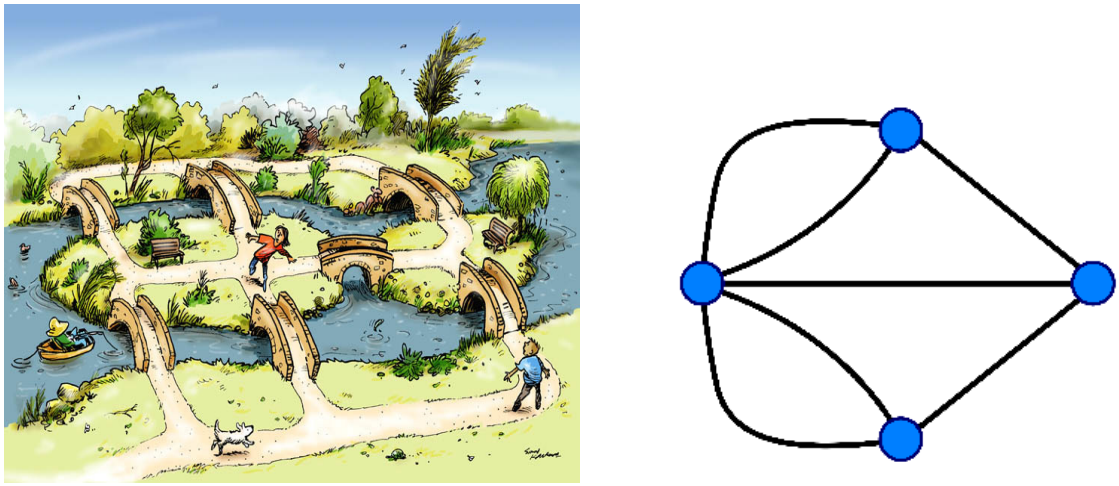

Figure 4.1: Left image is an illustration of the Königsberg bridge puzzle. Right image is the problem written using the mathematical structure called graph. Left image from Simon Kneebone, https://simonkneebone.com/2011/11/29/konigsberg-bridge-puzzle/. Right image from CC BY-SA 3.0, https://commons.wikimedia.org/w/index.php?curid=851840.

two nodes with odd degree. Such a path has been named as *Euler walk* in his honour.

One of the important application of topology is to quantitatively study the morphology of spacial structures induced by physical processes. An example is the study of microstructured materials. When intricate structures develop in the material as a consequence of interactions such as self assembly in liquid crystals, we need to understand how the spatial patterns are related to physical properties such as elasticity, permeability and conductance. Here observables are required to capture the morphological features of the spatial pattern, which can then be used to quantitatively study the spatial patterns in relation to the physical processes.

In this chapter, we introduce geometrical and topological observables, namely,

Betti numbers, Minkowski Functionals, and Tensor Minkowski Functionals. We use these quantities to study 2-dimensional random fields. In particular, we use these observables to quantify various morphological features of the CMB fields and use them to study the statistical properties of CMB fields in relation to different parameters of standard model of cosmology. A description for each of these observables will be presented in the subsequent sections. Simple definitions and notations that we will be using are as follows:

- A random field that lies on a two dimensional Euclidean plane $\mathbb{E}^2$ will be denoted as $p(x, y)$.

- A random field that lies on a two dimensional surface of a sphere $\mathbb{S}^2$ will be denoted as $s(\theta, \phi)$, where θ is latitude and ϕ is longitude.

- A threshold value is chosen among the range of values taken by a given random field. This is then expressed in terms of the RMS, denoted as σ_0, of the random field. This is denoted as ν.

- The excursion set is the set of all points with the field value greater than or equal to $\nu\sigma_0$. This set is denoted as K. The set of all points where the field value is equal to $\nu\sigma_0$ is denoted as ∂K, which is a subset of K. The left image in Fig. 4.2 shows an example of excursion set on an Euclidean plane. The points of white region belong to the excursion set while the points of black region do not belong to the set. In this example, ∂K is a set of all the points on the boundaries of the white region. Similarly, the right image in Fig. 4.2 shows an example of excursion set on a sphere.

- An excursion set may contain one or more connected regions. Further, each of these connected regions may be simply connected, which implies

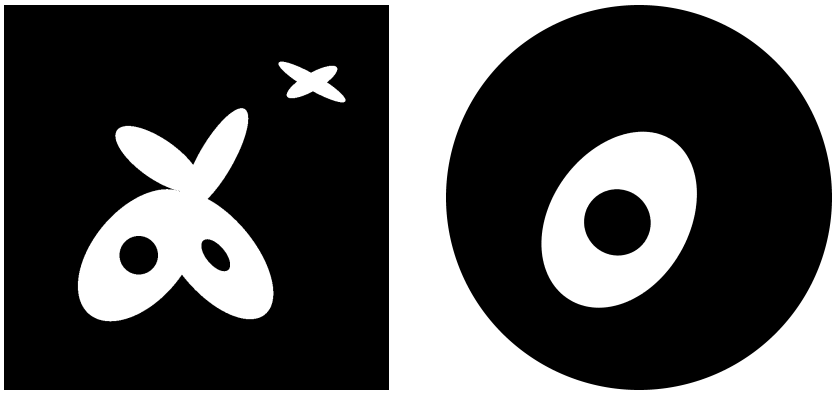

Figure 4.2: Images show the excursion sets on a plane (left image) and sphere (right image). White region are points that belong to the set while black region are points that do not belong to the set. In the left image, an excursion set lying on a plane is shown, which contains two hot spots and two cold spots. In the right image, the excursion set lying on a sphere is shown, which contains one hot spot and one cold spot.

that it does not contain any holes, or it may be multiply connected, which means that it contains one or more number of holes in them. The left image in Fig. 4.2 shows two connected regions in the excursion set. The connected region of smaller size located on the right corner of the image is an example of a simply connected region with no holes. On the other hand, the larger one located at the center of the image is a multiply connected region with two holes within it. Similarly, the right image in Fig. 4.2 contains one multiply connected region with one hole. We refer to a connected region as hot spot and a hole as cold spot. We refer to either hot spot or cold spot as structure.

4.2 Betti numbers

4.2.1 Definition

Consider a 2-dimensional mathematical object. It can be associated with two Betti numbers, denoted as β_0 and β_1, based on whether the points within the object are connected or disconnected with each other. β_0 is the number of connected regions within the object while β_1 is the number of disconnected regions within it. Consider for example a disc, all the points within a disc are connected with each other and there are no disconnected regions within it. Hence, $\beta_0 = 1$ and $\beta_1 = 0$. For a disc with a hole within it, the points of the object surrounding the hole are connected with each other while the points within the hole are disconnected from the points of the objects. Therefore, it has one connected region and one disconnected region, so $\beta_0 = 1$ and $\beta_1 = 1$. If the disc has two holes, then as the two holes are disconnected with each other, they form two disconnected regions. So, $\beta_0 = 1$ and $\beta_1 = 2$. Note that any deformation of the object does not affect these quantities and hence these are topological observables.

The above idea can be extended to define Betti numbers for an excursion set. The excursion set is the set of all points within the mathematical object. The connected region of the object is nothing but a hot spot in the excursion set while a hole is a cold spot. Note that the excursion set may contain more than one connected regions. Then the definition of Betti numbers for an excursion set, K, of either $p(x, y)$ or $s(\theta, \phi)$ becomes

- β_0 = number of hot spots
- β_1 = number of cold spots.

For example, the Betti number for the excursion sets shown in Fig. 4.2 are $\beta_0 = 2$ and $\beta_1 = 2$, for the case where the excursion set lies on a plane, and $\beta_0 = 1$ and $\beta_1 = 1$, for the case where the excursion set lies on a sphere.

The boundary of the excursion set, i.e. ∂K, is made up of a number of closed contours. An orientation can be assigned to each of the closed contours. A closed contour which is enclosing a hot spot is given a positive sign, and a closed contour which is enclosing a cold spot is given a negative sign. Then β_0 and β_1 are the number of positive and negative orientation closed contours respectively. Mathematically, the Betti numbers for an excursion set K with smooth boundary ∂K can be written as

$$\beta_0 = \frac{1}{2\pi}\int_{C_+} \kappa d\ell, \quad \beta_1 = \frac{1}{2\pi}\int_{C_-} \kappa d\ell, \tag{4.1}$$

where $d\ell$ is the line element and κ is the curvature at each point of the closed contours. C_+ denotes positive orientation closed contours while C_- denotes negative orientation closed contours. Here, the curvature κ is defined as

$$\kappa(\ell) = \frac{d\tau}{d\ell}, \tag{4.2}$$

where τ is the angle between the tangent vector at point ℓ of the closed contour and a fixed direction. The Betti numbers expressed in terms of τ is given by

$$\beta_0 = \frac{1}{2\pi}\int_{C_+} d\tau, \quad \beta_1 = \frac{1}{2\pi}\int_{C_-} d\tau. \tag{4.3}$$

4.2.2 Numerical computation of Betti numbers

Here, we describe a numerical method to compute Betti numbers [84]. This is based on the method for computing genus (see Sec. 4.3.1 for definition) used in Gott *et al.* (1990) [55].

In the case of a field $s(\theta, \phi)$, each point on the sphere is mapped onto a plane. We use stereo-graphic projection to implement this mapping. The image in Fig. 4.3 shows the implementation of stereo-graphic projection. For this projection, we take the equator as the projection plane. First, each point on the southern hemisphere is mapped onto the projection plane with the north pole as projection point as shown in the figure. A line (dashed black line) is drawn connecting the north pole and any point on the southern hemisphere (solid green ball), then the field value at this point is mapped onto a point (green circle) where the line intersects with the projection plane. Then this procedure is repeated to map each point on the northern hemisphere onto the projection plane with the south pole as projection point.

In a realistic case, the contours in an excursion set on a plane are approximated by line segments due to pixelization. For example in Fig. 4.4, left image shows an excursion set with a circular structure. Its contours are approximated by line segments shown in black line. The right image in Fig. 4.4 shows the final structure, which is a square shaped structure. Note that the closed polygon has positive orientation. In general, the contour of a irregular shaped structure will become a irregular shaped polygon due to pixelization.

The Betti numbers of a pixelized excursion set is given by

$$\beta_0 = \frac{1}{2\pi}\sum_{i_+}(\Delta\tau)_{i_+}, \quad \beta_1 = \frac{1}{2\pi}\sum_{i_-}(\Delta\tau)_{i_-}, \tag{4.4}$$

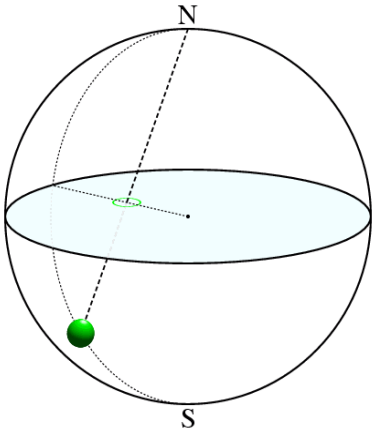

Figure 4.3: Image shows the mechanism of stereo-graphic projection with equator as the projection plane. Here, the north pole is chosen as the projection point. Each point (solid green ball) on the southern hemisphere is mapped onto a point (green circle) on the equator by connecting a line from the north pole to points on the southern hemisphere (dashed black line). Image from http://pd.chem.ucl.ac.uk/pdnn/symm2/proj3a.htm.

where $(\Delta\tau)_i$ are the exterior angles, which is the angle between the tangent vectors at i^{th} and $(i+1)^{\text{th}}$ vertex of the polygon, and i_+ represents the vertices of the positive orientation closed polygons while i_- represents the vertices of the negative orientation closed polygons. For example, Betti numbers of the polygon shown in the right image of Fig. 4.4 can be computed by calculating the exterior angles at all the vertices. The exterior angle at all the vertices of a square is $\pi/2$. Hence we get, $\beta_0 = \frac{1}{2\pi}(\pi/2+\pi/2+\pi/2+\pi/2) = 1$ and $\beta_1 = 0$.

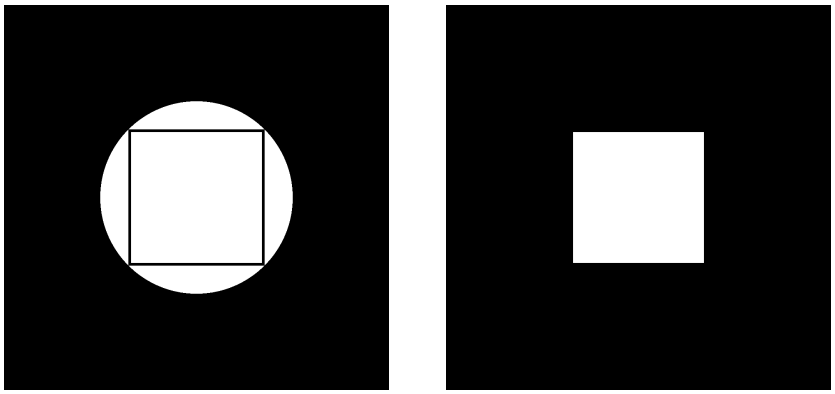

Figure 4.4: Images show the affect of approximation of a structure to a polygon. Left image shows a circular structure, whose contours are approximated to line segments (black line). Right image shows the final polygon obtained after the approximation, which is a square shaped structure. Here, the pixel size is assumed to be comparable to the size of the structure. Note that in general, when the pixel size is much smaller than the size of the structure, then the structure will become a polygon with many sides.

4.3 Minkowski Functionals

4.3.1 Definition

In integral geometry, Hadwiger's theorem [113, 114] states that in d-dimensional Euclidean space, any morphological observable of an excursion set is a linear combination of $d+1$ functionals, which are known as Minkowski Functionals. Hence the morphology of an excursion set on a two dimensional space is completely described by three Minkowski Functionals. This theorem is also valid for curved spaces [64, 65].

The Minkowski Functionals for an excursion set, K, with a smooth boundary ∂K of a field $s(\theta, \phi)$, on a sphere of radius R, are defined as

$$\begin{aligned} \mathbb{V}_0 &= \int_K da, \\ \mathbb{V}_1 &= \frac{1}{4}\int_{\partial K} d\ell, \\ \mathbb{V}_2 &= \frac{1}{2\pi}\int_{\partial K} d\ell\ \kappa, \end{aligned} \tag{4.5}$$

where da is the surface element. Each of these Minkowski Functionals has a simple physical interpretation:

- $\mathbb{V}_0$ = total area of the excursion set
- $\mathbb{V}_1$ = total length of the contours or boundaries of the excursion set
- $\mathbb{V}_2$ = number of hot spots - number of cold spots.

The functional $\mathbb{V}_2$ is equal to the difference between the Betti numbers $\mathbb{V}_2 = \beta_0 - \beta_1$. For example, $\mathbb{V}_2$ for the excursion sets shown in Fig. 4.2 are $\mathbb{V}_2 = 2 - 2 = 0$, where the excursion set lies on a plane, and $\mathbb{V}_2 = 1 - 1 = 0$, where the excursion set lies on a sphere. Further, $\mathbb{V}_2$ is a topological observable while $\mathbb{V}_0$ and $\mathbb{V}_1$ are geometrical observables. In standard practice, Minkowski Functionals per unit area are used for the analysis of CMB fields, which is given by

$$V_j = \frac{\mathbb{V}_j}{4\pi R^2}, \tag{4.6}$$

where $j = 0, 1, 2$. These are scalar quantities since they are invariant under coordinate transformations. Hence, we refer to these three functionals as S*calar* M*inkowski* F*unctionals* (SMFs). V_0 is referred as area fraction, V_1 as contour

length, and V_2 as genus.

4.3.2 Minkowski Functionals of a Gaussian field

The excursion set of a field will vary systematically with the threshold value depending on the statistical properties of the field. The SMFs can capture these systematic variation of the excursion set with the threshold value. In this section, we discuss the SMFs of a random field which has a Gaussian distribution.

The SMFs of a Gaussian random fields have been well studied in the literature [115, 116]. Their analytic expressions in arbitrary dimensions was derived by Tomita [117]. Consider $s(\theta, \phi)$ to have a Gaussian distribution. Then the analytic expression for SMFs, in two dimensional space, as a function of ν are given by

$$\begin{aligned} V_0^{\rm an}(\nu) &= \frac{1}{2}\left[1 - \Theta\left(\frac{\nu}{\sqrt{2}}\right)\right], \\ V_1^{\rm an}(\nu) &= \frac{1}{8\sqrt{2}}\frac{\sigma_1}{\sigma_0}e^{-\nu^2/2}, \\ V_2^{\rm an}(\nu) &= \frac{1}{(2\pi)^{3/2}}\left(\frac{\sigma_1}{\sigma_0}\right)^2 \nu e^{-\nu^2}, \end{aligned} \tag{4.7}$$

where the superscript 'an' indicates that it is analytic expression, Θ is the Gaussian error function, given by $\Theta(x) = \frac{2}{\sqrt{\pi}}\int_0^x dt\ \exp(-t^2)$, and $\sigma_1 = \langle \nabla s \cdot \nabla s \rangle$. The amplitude of SMFs depend only on σ_0 and σ_1. These are related to the power spectrum, C_ℓ, as

$$\sigma_j^2 = \frac{1}{4\pi}\sum_\ell (2\ell+1)\ \left[\ell(\ell+1)\right]^j C_\ell W_\ell^2, \tag{4.8}$$

for $j = 0, 1$ [40], where W_ℓ is the smoothing weightage. For a Gaussian smoothing, $W_\ell = e^{-\ell(\ell+1)\theta_s^2/2}$. Hence the SMFs of a Gaussian random field depends only on the power spectrum. However, if there are any non-Gaussian features in the field, then that will show up as deviation in the SMFs from the analytic formula in Eq. (4.7).

4.3.3 Numerical computation of Minkowski Functionals

We describe here two methods for computing SMFs of a random field on a sphere. The first method was introduced by Schmalzing and Gorski [65]. The line integrals in Eq. (4.6) for contour length and genus can be transformed into surface integrals, then the SMFs as a function of ν can be written as

$$V_j(\nu) = \frac{1}{4\pi R^2} \int_{\mathbb{S}^2} da\ I_j. \tag{4.9}$$

Here, I_j's are related to the field $s(\theta, \phi)$ and its covariant derivatives as follows

$$\begin{aligned} I_0 &= \Theta(s-\nu), \\ I_1 &= \frac{1}{4}\delta(s-\nu)\sqrt{s_{;\theta}^2 + s_{;\phi}^2}, \\ I_2 &= \frac{1}{2\pi}\delta(s-\nu)\frac{2s_{;\theta}s_{;\phi}s_{;\theta\phi} - s_{;\theta}^2 s_{;\phi\phi} - s_{;\phi}^2 s_{;\theta\theta}}{s_{;\theta}^2 + s_{;\phi}^2}, \end{aligned} \tag{4.10}$$

where the subscript ';' indicates covariant derivatives. The covariant derivatives are related to partial derivatives as

$$s_{;\theta} = s_{,\theta}, \qquad s_{;\phi} = \frac{1}{\sin\theta} s_{,\phi},$$

$$s_{;\theta\theta} = s_{,\theta\theta}, \qquad s_{;\theta\phi} = \frac{1}{\sin\theta} s_{,\theta\phi} - \frac{\cos\theta}{\sin^2\theta} s_{,\phi}, \qquad s_{;\phi\phi} = \frac{1}{\sin^2\theta} s_{,\phi\phi} + \frac{\cos\theta}{\sin\theta} s_{,\theta}. \tag{4.11}$$

In a realistic situation, there are only finite number of sample points or pixels in the excursion set. The delta function is replaced with a function of finite bin width $\Delta\nu$ as

$$\delta(s-\nu) \approx \frac{1}{\Delta\nu} d(s-\nu), \tag{4.12}$$

where

$$d(s-\nu) = \begin{cases} 1 & \nu - \dfrac{\Delta\nu}{2} \leq s \leq \nu + \dfrac{\Delta\nu}{2} \\ 0 & \text{otherwise} \end{cases} . \tag{4.13}$$

The bin width $\Delta\nu$ is decided by the spacing between the threshold levels. And the integrals are replaced with the summation over all the pixels as

$$V_j(\nu) \approx \frac{1}{N_{\rm pix}} \sum_{i=1}^{N_{\rm pix}} I_j(\mathbf{x}_i), \tag{4.14}$$

where $\mathbf{x}_i$ is the position vector of $i^{\rm th}$ sample point or pixel on the sphere. We refer to this method of numerical computation of `SMF`s as `S`*chmalzing* and `G`*orski* (`SG`) method.

In the above method, due to the discretization of Eq. (4.6) numerical inaccuracies are introduced in the calculation of V_1 and V_2 [118]. The numerically estimated `SMF`s can be written as $V_j(\nu) = V_j^{\rm an}(\nu) + R_j^{\Delta\nu}(\nu)$, where $R_j^{\Delta\nu}$ is the residual error due to discretization. Here, the superscript $\Delta\nu$ indicates the threshold bin size and the dependency of residual error on it. The residual

error, $R_j^{\Delta\nu}$, is given by

$$R_j^{\Delta\nu}(\nu) = \frac{1}{\Delta\nu}\int_{\nu-\Delta\nu/2}^{\nu+\Delta\nu/2} \mathrm{d}s V_j^{\rm an}(s) \; - \; V_j^{\rm an}(\nu). \tag{4.15}$$

The residual error cannot be estimated without knowing the exact analytic expression, $V_j^{\rm an}(\nu)$, of the random field. While for the case of a Gaussian field, since the exact analytic expression is given by Eq. (4.7), $R_j^{\Delta\nu}$ can be computed as

$$\begin{aligned} R_1^{\Delta\nu}(\nu) &= \frac{1}{8}\sqrt{\frac{\pi}{2}}\,\frac{\sigma_1}{\sigma_0}\frac{1}{\Delta\nu}\left[\mathrm{erf}\left(\frac{\nu+\Delta\nu/2}{\sqrt{2}\sigma_0}\right) - \mathrm{erf}\left(\frac{\nu-\Delta\nu/2}{\sqrt{2}\sigma_0}\right)\right] - V_1^{\rm an}(\nu) \\ R_2^{\Delta\nu}(\nu) &= \frac{1}{(2\pi)^{3/2}}\left(\frac{\sigma_1}{\sigma_0}\right)^2\frac{1}{\Delta\nu}\left[\exp\left(-\frac{(\nu-\Delta\nu/2)^2}{\sqrt{2}\sigma_0}\right)\right. \\ &\quad \left. -\exp\left(-\frac{(\nu+\Delta\nu/2)^2}{\sqrt{2}\sigma_0}\right)\right] - V_2^{\rm an}(\nu). \end{aligned} \tag{4.16}$$

The second method to compute SMFs is a geometrical technique [119, 120]. The area fraction can be obtained by counting the number of pixels which have field value above the threshold value. The contour length is determined by constructing line segments along the boundaries through interpolation of the field values using least square method. This interpolation requires the first derivatives of the field which are obtained using HEALPix package. The Euler characteristics (χ), which is related to V_0 and V_2 as $\chi = V_2 + \frac{1}{2\pi R^2}V_0$ for an excursion set on a sphere, is the integration of the curvature over all the boundaries of the excursion set. As the topological properties are invariant under continuous transformation of the boundary, explicit calculation of the boundary curvature is not required instead the curvature can be considered to be concentrated at the vertices of the boundaries of the pixels. Curvature

weights are assigned at each of the vertices, which is determined by the field value at the pixels surrounding the vertex. Then the summation over these weights gives the Euler characteristic. We refer to this numerical method for computing the SMFs as CND_REG2D method.

4.4 Tensor Minkowski Functionals

4.4.1 Definition

T*ensor* M*inkowski* F*unctionals* (TMFs) are tensor generalization of SMFs [86, 87]. Since these are tensor quantities, they can capture more information about the morphological properties of a given excursion set than the SMFs.

Consider an excursion set K with a smooth boundary ∂K of a field $p(x, y)$. Let K_s be a subset of K which contains only one simply or multiply connected region with a smooth boundary ∂K_s. Then the TMFs of rank $a+b$, with $a+b \geq 0$, for K_s are defined as

$$\begin{aligned} W_0^{a,0} &= \int_{K_s} \vec{r}^{\,a} da, \\ W_j^{a,b} &= \frac{1}{2} \int_{\partial K_s} \vec{r}^{\,a} \otimes \hat{n}^{\,b} G_j d\ell, \end{aligned} \tag{4.17}$$

for $j = 1, 2$ with $G_1 = 1$ and $G_2 = \kappa$, where $\vec{r}$ is the position vector and $\hat{n}$ is the unit normal vector at each point on the contour ∂K_s. The contour which forms the boundary of a hot spot is assigned a counterclockwise direction while that of a cold spot is assigned clockwise direction. The components of tensor product between two vectors, namely $\vec{A}$ and $\vec{B}$, is defined as $(\vec{A} \otimes \vec{B})_{ij} = (A_i B_j + A_j B_i)/2$. When we take $a + b = 0$, then the Eq. (4.17) reduces to

three SMFs, but with different normalization constants, as

$$W_0^{0,0} = \int_{K_s} da,\ W_j^{0,0} = \frac{1}{2}\int_{\partial K_s} G_j\ d\ell. \tag{4.18}$$

The equation yields three Vector Minkowski Functionals with $a = 1$ and $b = 0$ as

$$W_0^{1,0} = \int_{K_s} \vec{r}\, da,\ W_j^{1,0} = \frac{1}{2}\int_{\partial K_s} \vec{r}\, G_j d\ell. \tag{4.19}$$

Seven kinds of Tensor Minkowski Functionals of rank 2 can be constructed with $a + b = 2$, namely $W_0^{2,0}$, $W_1^{2,0}$, $W_1^{1,1}$, $W_1^{0,2}$, $W_2^{2,0}$, $W_2^{1,1}$, and $W_2^{2,2}$.

The Scalar Minkowski Functionals are motion-invariant, which means that they are invariant under translation and rotation transformation. While Vector and Tensor Minkowski Functionals are motion-covariant, which means that they vary under these transformations. Their transformation under the operation of translation and rotation on a single structure, K_s, are given by

$$\begin{aligned} W_\nu^{a,b}(K_s + \vec{t}\,) &= \sum_{c=0}^{a} \binom{a}{c} \vec{t}^{\,c} \otimes W_\nu^{a-c,b}(K_s), \\ W_\nu^{a,b}(\hat{R}\ K_s) &= \hat{R}\ W_\nu^{a,b}(K_s). \end{aligned} \tag{4.20}$$

Here, $K_s + \vec{t}$ denotes that all the points of the structure, K_s, are translated by the vector $\vec{t}$, and $\hat{R}$ is the rotation operator, for clockwise rotation by angle θ, it is given by

$$\hat{R}(\theta) = \begin{pmatrix} \cos\theta & \sin\theta \\ -\sin\theta & \cos\theta \end{pmatrix}. \tag{4.21}$$

The motion-covariant Minkowski Functionals can be divided further based on their more specific behavior under translation operation. Those which satisfy

$W_\nu^{a,b}(K_s+\vec{t}) = W_\nu^{a,b}(K_s)$ are called translation-invariant while others are called translation-covariant. Hence from Eq. 4.20, $W_\nu^{0,b}$ are translation-invariant for any b and ν. Further, $W_1^{1,1}$ and $W_2^{1,1}$ are also translation-invariant [121]. While rest of the motion-covariant Minkowski Functionals of rank 1 and rank 2 are translation-covariant. Translation-invariant Minkowski Functionals capture information about the characteristics of the structure and they are insensitive to the position of the structure. Hence, we are interested in the application of translation-invariant Minkowski Functionals to the `CMB` analysis.

When the structure, K_s, is rescaled in space, which implies that the coordinate of each point on the structure is multiplied with a scaling factor λ, then the Minkowski Functionals transform as

$$W_\nu^{a,b}(\lambda K_s) = \lambda^{2+a-\nu} W_\nu^{a,b}(K_s). \tag{4.22}$$

Another interesting property of the Minkowski Functionals is that they are additive, which implies that for any two structures, say K_{s1} and K_{s2}, the Minkowski Functionals satisfy

$$W_\nu^{a,b}(K_{s1} \cup K_{s2}) = W_\nu^{a,b}(K_{s1}) + W_\nu^{a,b}(K_{s2}) - W_\nu^{a,b}(K_{s1} \cap K_{s2}). \tag{4.23}$$

The Minkowski Functionals are not independent, they have inter-dependencies

$$W_\nu(K_s)E = \nu W_\nu^{0,2}(K_s) + W_{\nu+1}^{1,1}(K_s),$$

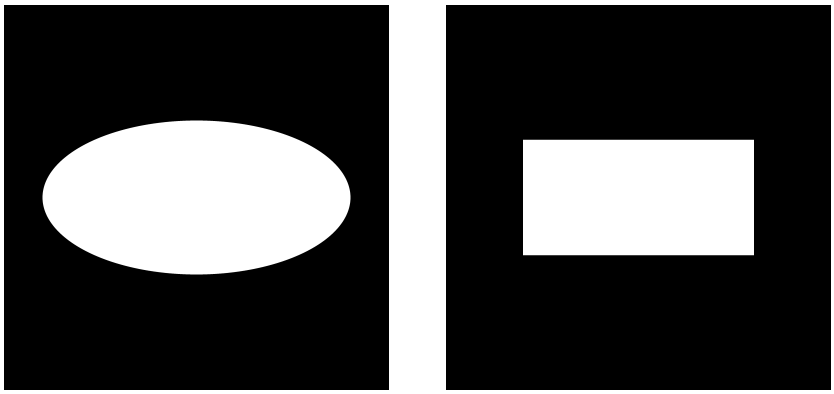

Figure 4.5: The excursion set containing a single elliptically shaped structure is shown in the left image. White region are the points that belong to the excursion set while the black region are points that are not part of the set. The right image shows an excursion set with a rectangle shaped structure.

for any single structure K_s and $\nu = 0, 1, 2$ [122, 87], specifically

$$\begin{aligned} W_0(K_s)E &= W_1^{1,1}(K_s), \\ W_1(K_s)E &= W_1^{0,2}(K_s) + W_2^{1,1}(K_s), \\ W_2(K_s)E &= 2W_2^{0,2}(K_s). \end{aligned} \tag{4.24}$$

We note that from these equations that $W_1^{1,1}$ and $W_2^{0,2}$ does not give any additional information in comparison to the Scalar Minkowski Functionals. While $W_1^{0,2}$ and $W_2^{1,1}$ contain additional information but they are related to each other. This relation can also be written as $W_2^{1,1} = \hat{R}^T(\pi/2)\, W_1^{0,2}\, \hat{R}(\pi/2)$, where $\hat{R}(\pi/2)$ is the rotation operator with an angle of $\pi/2$. Therefore, all the new information is contained in one of these Tensor Minkowski Functionals. Hence, we focus on $W_2^{1,1}$ for the application to `CMB` analysis.

For example, the analytic expression for $W_2^{1,1}$ of an elliptical shaped structure shown in the left image of Fig. 4.5, K_s, is given by

$$W_2^{1,1}(K_s) = \begin{bmatrix} f_2^{1,1}(p,q) & 0 \\ 0 & f_2^{1,1}(q,p) \end{bmatrix}, \tag{4.25}$$

$$\text{with } f_2^{1,1}(p,q) = \frac{1}{2}p^2q^2\int_0^{2\pi} d\varphi \frac{cos^2\varphi}{[p^2-(p^2-q^2)cos^2\varphi]^{3/2}}, \tag{4.26}$$

where p and q are the semi-major and semi-minor axis of the ellipse respectively [123]. For the case of a circle, we take $p = q$ then the above expression reduces to

$$W_2^{1,1}(K_s) = \begin{bmatrix} p/2 & 0 \\ 0 & p/2 \end{bmatrix}. \tag{4.27}$$

4.4.2 $W_2^{1,1}$ for structures in an excursion set of a pixelized field

For a pixelized field, the excursion set, K, will become a set containing a finite number of pixels and the subset K_s will consist of pixels which are part of a single structure. As mentioned before in the case of Betti numbers in Subsection. 4.2.2, the structures in this excursion set are approximated to polygons. Here, we describe $W_2^{1,1}$ for a polygonal structure given by Schröder Turk *et al.* (2010) [123].

A polygonal structure will consist of the vertices $\vec{v}_i$ for $i = 1, \ldots n_v$ and the edges vector $\vec{e}_{(i,i+1)}$ for $i = 1, \ldots n_v - 1$, where n_v is the total number of vertices of the polygon. As mentioned before, the direction of the edges vector are chosen to be counterclockwise around hot spots while clockwise direction around cold spots. The unit normal vector of an edge is given by

$\vec{n}_{(i,i+1)} = \hat{R}(\pi/2)\frac{\vec{e}_{(i,i+1)}}{|\vec{e}_{(i,i+1)}|}$. The exterior angle, $\Delta\tau_i$, is the angle between the unit normals vector of the two adjacent edges vector. Its value ranges from $-\pi$ to π. Further, a polygonal structure is a convex structure if all the exterior angles $\Delta\tau_i$ are greater than zero otherwise it is a concave structure. The left and middle image in the Fig. 4.6 shows example for convex and concave structure respectively.

For a polygonal structure, the curvature κ is discontinuous as: $\kappa = 0$ along the edges while it is undefined at the vertices. Let the polygonal structure, K_s, be a convex structure, then its $W_2^{1,1}$ can be computed using *parallel body construction*. In parallel body construction, a parallel structure $K_{s+\epsilon}$ of K_s is constructed as

$$K_{s+\epsilon} = K_s \uplus B_\epsilon. \tag{4.28}$$

Here, B_ϵ is a disk of radius ϵ and $\uplus$ is the Minkowski sum. The Minkowski sum of K_s and B_ϵ is obtained as follows: A disk B_ϵ is constructed around every point of K_s, the union of all these disks gives $K_{s+\epsilon}$. This process converts the sharp turns at the vertices to a smooth circular boundaries and with well defined curvature as shown in Fig. 4.7. For the calculation of $W_2^{1,1}$, only the circular boundaries at the vertices need to be considered as $\kappa = 0$ on all the line segments. Now the analytic expression for $W_2^{1,1}$ of convex polygonal structure, K_s, is obtained with the limit of $\epsilon \to 0$ by using the definition in Eq. 4.17, which yields

$$W_2^{1,1}(K_s) = \sum_{i=1}^{n_v-1} \frac{1}{2}|e_{(i,i+1)}|^{-1}(\vec{e}_{(i,i+1)} \otimes \vec{e}_{(i,i+1)}). \tag{4.29}$$

Note that since the edges vector are real, and as the tensor product is defined

to be symmetric, the above tensor is a real symmetric matrix. In general, the structures are not convex. For the case of concave polygonal structure, a concave structure can be considered to be the union of two or more convex structures. Consider the concave structure, K_s, shown in the middle image of Fig. 4.6, which can be considered to be the union of two convex structures, say K_{s1} and K_{s2}. It has one vertex where $\Delta\tau_i < 0$, where it has a concave dip. Then the structure is split at the vertex, into two convex structures as shown in the right image of the figure. From the additive property of the Minkowski Functionals, the $W_2^{1,1}$ of concave polygonal structure can be expressed in terms of its convex structure components as

$$W_2^{1,1}(K_s) = W_2^{1,1}(K_{s1} \cup K_{s2}) = W_2^{1,1}(K_{s1}) + W_2^{1,1}(K_{s2}) - W_2^{1,1}(K_{s1} \cap K_{s2}). \tag{4.30}$$

Hence, the analytic expression for $W_2^{1,1}$ in Eq. 4.29 is valid for any general polygonal structure.

As an example, consider a rectangular shaped structure of sides p and q with $p \geq q$, which is an approximation of ellipse, as shown in the right image of Fig. 4.5. Then the $W_2^{1,1}$ can be obtained from Eq. 4.29 as

$$W_2^{1,1}(K_s) = \frac{1}{2}\left(2\begin{bmatrix} p & 0 \\ 0 & 0 \end{bmatrix} + 2\begin{bmatrix} 0 & 0 \\ 0 & q \end{bmatrix}\right), \tag{4.31}$$

$$= \begin{bmatrix} p & 0 \\ 0 & q \end{bmatrix}. \tag{4.32}$$

We introduce TMFs, in particular $W_2^{1,1}$, as a new statistical observable for the analysis of CMB. We have developed a code to compute $W_2^{1,1}$ for polygonal

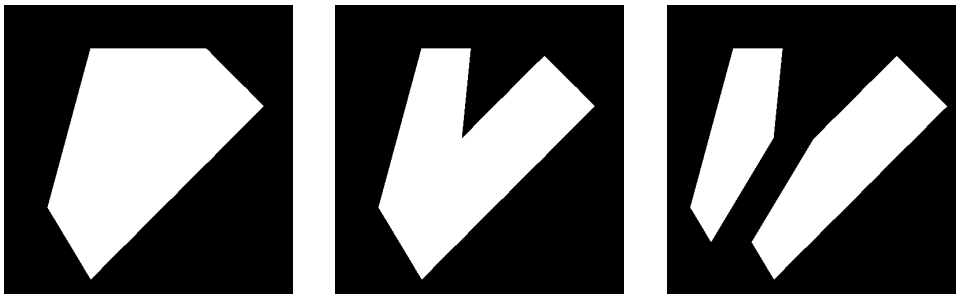

Figure 4.6: Images show a convex polygonal structure (left image), concave polygonal structure (middle image) and the concave structure being split into two convex structure. A structure is convex if the straight line joining any two points in it, also belongs to the structure otherwise it is concave. The structure in the middle image has a concave dip, so a straight line can be drawn connecting the two points which lie on opposite sides of this dip. The points of the straight line that fall on the dip does not belong to the structure and hence the structure is concave. The right image shows the concave structure being split into two convex structures.

Figure 4.7: Images show the process of parallel body construction for a square shaped structure. Left image shows a square structure. Right image shows the square shaped structure after parallel body construction. A disc is constructed at every point of the square, the union of all these discs gives the right image.

structures on an Euclidean plane using the Eq. 4.29. The code uses the algorithm in [123], which will be described in Chapter. 7.

4.4.3 Anisotropy and orientation of structures in an excursion set

The tensor $W_2^{1,1}$ is a real symmetric 2×2 matrix, hence it will have two real eigenvalues. For an excursion set K, each structure can be associated with a tensor $W_2^{1,1}$. Let the corresponding eigenvalues be denoted as λ_1 and λ_2 with $\lambda_1 \leq \lambda_2$. The tensor $\left\langle W_2^{1,1} \right\rangle$ can also be obtained for the excursion set, where $\langle \dots \rangle$ indicates average over all the structures of K for each component of the tensor. Let Λ_1 and Λ_2 with $\Lambda_1 \leq \Lambda_2$, be the eigenvalues of $\left\langle W_2^{1,1} \right\rangle$. Then the ratios of eigenvalues namely α and β are defined as

$$\alpha \equiv \frac{\Lambda_1}{\Lambda_2}, \tag{4.33}$$

$$\beta \equiv \left\langle \frac{\lambda_1}{\lambda_2} \right\rangle. \tag{4.34}$$

The quantity α is estimated as: the tensor $\langle W_2^{1,1} \rangle$ is obtained by averaging over all the structures of the excursion set, its eigenvalues are computed, and then the ratio of eigenvalues are estimated. While β is estimated as: ratio of eigenvalues for $W_2^{1,1}$ of each of the structures in the excursion set is calculated, and then it is averaged over all the structures.

When the excursion set consists of a single structure, the value of β will quantify the intrinsic anisotropy in the shape of the structure. In this case, α will be equal to β. Consider simple isotropic structures like circle and square. For a circle, $W_2^{1,1}$ is given by Eq. 4.27 which gives $\beta = 1$. For a square, we use $W_2^{1,1}$ given in Eq. 4.32 with $p = q$ which again gives $\beta = 1$. Hence for isotropic structures $\beta = 1$. While for a general shape the value of β will lie between 0 and 1. Further, $\beta < 1$ indicates that the shape is anisotropic and the

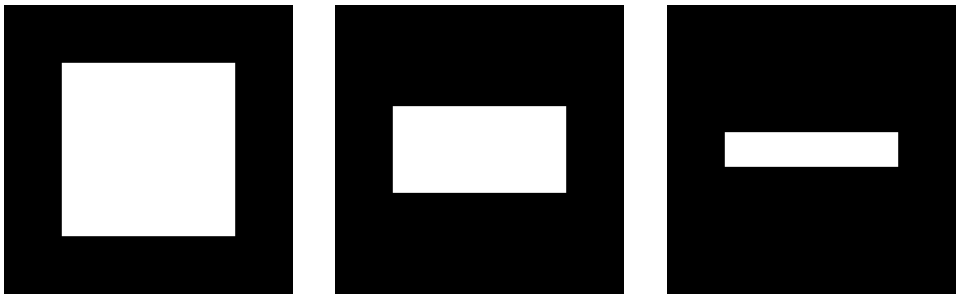

Figure 4.8: Images show rectangles, with sides p and q for $p \geq q$, for different aspect ratios, q/p. Left image shows square shaped structure which is isotropic. Middle image shows a rectangular shaped structure with aspect ratio of 0.5. Rectangular structure with aspect ratio of 0.2 is shown in the right image.

extent of deviation of β from 1 gives a measure of deviation in the shape of the structure from the isotropic shape. For an illustration consider the rectangles, having sides p and q with $p \geq q$, shown in Fig. 4.8. The left image shows a square which is isotropic, the middle image shows a rectangle with the aspect ratio, q/p, of 0.5, and the right image shows a rectangle with the aspect ratio of 0.2. The corresponding β values are obtained from the analytic expression for $W_2^{1,1}$ of a rectangle, which is given in Eq. 4.32. The eigenvalues of $W_2^{1,1}$ from the equation are q and p. Hence for the special case of a rectangle, we get $\beta = q/p$ which is same as the aspect ratio. Therefore, β for the rectangles in Fig. 4.8 are $1, 0.5$ and 0.2 respectively. Note that for a general shape, the β values need not be equal to the aspect ratio. When the excursion set contains many structures, β will give the net anisotropy in the structures.

For an excursion set containing many structures with anisotropic shape, it can be associated with an orientation. The quantity α quantifies the extent of orientation for a given arrangement of structures. When the structures are

randomly oriented then $\alpha = 1$. Alternatively, when the structures are aligned along the same direction then $\alpha = \beta$. In the intermediate case, the value of α will lie between β and 1. As an illustration consider the rectangles with different alignments as shown in Fig. 4.9. All these rectangles have an aspect ratio of 0.5. Left image shows an excursion set with two rectangular shaped structures which are aligned with each other. The value of α can be obtained using the Eq. 4.34 as

$$\langle W_2^{1,1} \rangle = \frac{1}{2} \left(\begin{bmatrix} p & 0 \\ 0 & q \end{bmatrix} + \begin{bmatrix} p & 0 \\ 0 & q \end{bmatrix} \right),$$
$$\Lambda_1 = q, \Lambda_2 = p,$$
$$\alpha = \frac{q}{p}.$$

Hence when the rectangles are completely aligned with each other, the value of α is equal to β, which in the present case is $\alpha = \beta = 0.5$. For the case of rectangles in the middle image of Fig. 4.9, where they are oriented at 45° to each other, we get

$$\langle W_2^{1,1} \rangle = \frac{1}{2} \left(\begin{bmatrix} p & 0 \\ 0 & q \end{bmatrix} + \hat{R}^T(-\pi/4) \begin{bmatrix} p & 0 \\ 0 & q \end{bmatrix} \hat{R}(-\pi/4) \right),$$
$$\Lambda_1 = \frac{p+q}{2}, \Lambda_2 = p,$$
$$\alpha = \frac{1}{2}(1 + \frac{q}{p}).$$

For the aspect ratio of 0.5, we get $\alpha = 0.75$. Similarly, for the case of rectangles aligned at right angle to each other as shown in the right image of Fig. 4.9, we

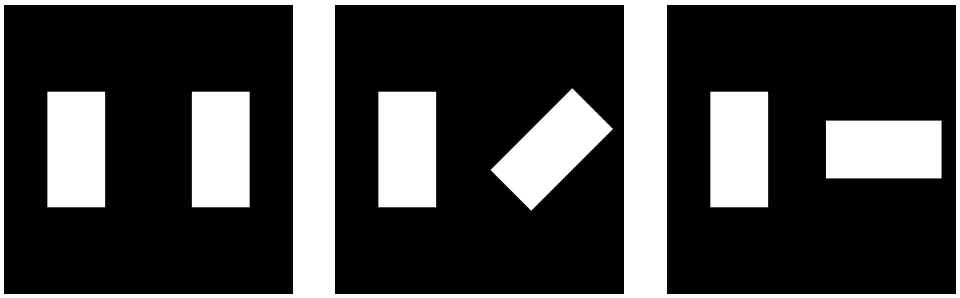

Figure 4.9: Each of the images show two rectangles of same aspect ratio but with different alignments. Left image shows rectangles which are aligned with each other. Middle image shows rectangles which are oriented at 45° with respect to each other. Rectangles which are aligned at right angle to each other are shown in the right image.

get

$$\langle W_2^{1,1} \rangle = \frac{1}{2}\left(\begin{bmatrix} p & 0 \\ 0 & q \end{bmatrix} + \begin{bmatrix} q & 0 \\ 0 & p \end{bmatrix}\right),$$
$$\Lambda_1 = \frac{p+q}{2}, \Lambda_2 = \frac{p+q}{2},$$
$$\alpha = 1.$$

These calculations show the variation of α with different alignment and its ability to capture the information about the alignment in the structures of a given excursion set.

We introduce a quantity $\mathscr{O}$ defined as

$$\mathscr{O} \equiv \frac{1-\alpha}{1-\beta}, \tag{4.35}$$

which is also a measure of orientation in the structures but it is scaled so that its value lies between zero and one. $\mathscr{O} = 1$ indicates that the structures are

completely aligned while $\mathscr{O} = 0$ indicates that the structures are randomly oriented. Consider the example of rectangles in Fig. 4.9, the value of $\mathscr{O}$ are $1, 0.5$, and 0 respectively. This is a useful quantity when comparing two distribution of structures with different net anisotropy β. This is because if these structures have high degree alignment then α is bounded below by the value of β, while $\mathscr{O}$ is not. In the example, the value of $\mathscr{O}$ when the structures are completely aligned is one and is not dependent on β. Hence it captures alignment of the structures independent of the anisotropy of the structures.

Chapter 5

Signature of primordial non-Gaussianity in CMB polarization

5.1 Introduction

Here, we study the effect of the presence of local type primordial non-Gaussianity on the CMB polarization fields using the geometrical and topological observable, namely SMFs and Betti numbers. Specifically, we investigate the local type non-Gaussian features in the E mode and $\tilde{I}_P$ fields. We neglect the instrumental effects and analyze the non-Gaussian deviation of these polarization fields in comparison to the cosmic variance. Further, we quantify the statistical sensitivity of the polarization fields for the presence of non-Gaussianity and comment about their ability to constrain $f_{\rm NL}$.

The organization of this chapter is as follows. In the second section, we analyze the non-Gaussian deviations in SMFs and Betti numbers of the polarization fields. In the third section, we quantify and compare the statistical sensitivity of temperature and polarization fields for detecting the presence of local type non-Gaussian features. Finally, we summarize the results and discuss about its implications in the fourth section.

5.2 Primordial non-Gaussian features in the CMB polarization

We study the non-Gaussian features in CMB polarization. The geometrical and topological observables, SMFs and Betti numbers, are used to capture these non-Gaussian features. Gaussian and local type non-Gaussian simulations of CMB temperature and E mode map provided by Elsner and Wandelt are used for the study.

For a Gaussian field, the exact SMFs are given by the analytic formula Eq. (4.7). While analytic expression for Betti numbers are not known, but it can be numerically calculated for a Gaussian field using the method described in Sec. 4.2.2. Any non-Gaussian features present in a given field will result in the deviation of SMFs and Betti numbers from the Gaussian expectations. The non-Gaussian deviation of SMFs are expressed as

$$\Delta V_i = V_i^{\mathrm{NG}} - V_i^{\mathrm{G}}, \tag{5.1}$$

for $i = 0, 1, 2$. Similarly, Betti numbers are expressed as

$$\Delta\beta_i = \beta_i^{\rm NG} - \beta_i^{\rm G}, \tag{5.2}$$

for $i = 0, 1$.

5.2.1 Scalar Minkowski Functionals

The SMFs of CMB polarization are estimated using the SG method described in Sec. 4.2.2. It was mentioned that the method has numerical error due to the discretization of delta function. In the present case, this does not result in significant error due to the following reason. Since the Gaussian and non-Gaussian maps are constructed from a single realization of Gaussian distributed random numbers and also as we are currently interested in the weakly non-Gaussian case, the numerical errors in the SMFs of both Gaussian and non-Gaussian maps will be similar and hence it will cancel each other when the non-Gaussian deviation is calculated.

In Fig. 5.1, the three top panels show the plots of SMFs calculated for E mode and their non-Gaussian deviations with $f_{\rm NL} = 10$ for various smoothing angles are shown in the lower panels. The chosen threshold values lie in the range $-4.5 \leq \nu \leq 4.5$ with the spacing of $\Delta\nu = 0.75$. The amplitudes of non-Gaussian deviation vary linearly with $f_{\rm NL}$. The plots were obtained by averaging over 1000 realizations of E mode field and the error bars are the corresponding sample variance. The contour length and genus, V_1 and V_2, of E mode field in the figure have larger amplitudes than the temperature field (refer to Fig. 2 in [68]). This implies that there are more structures in the E mode field than the temperature field. The non-Gaussian deviation in each

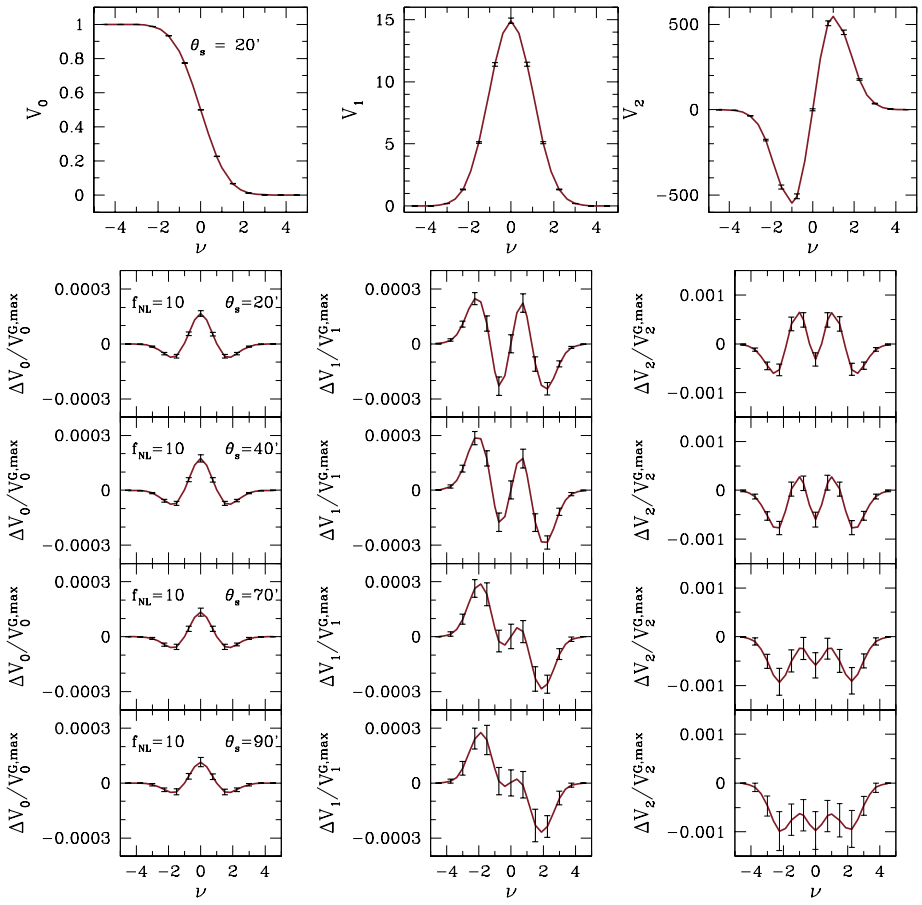

Figure 5.1: *Upper panels:* Plots show SMFs as a function of threshold for E mode. *Lower panels:* The corresponding non-Gaussian deviations in SMFs for $f_{\rm NL} = 10$ with different smoothing scales. The error bars shown are the sample variance calculated using 1000 realization of CMB fields.

of the SMFs shows a characteristic shape and they also vary slightly with the smoothing angle. The size of the error bars increases with the smoothing angle, θ_s, because there are only fewer number of structures which in turn results in the statistical uncertainties. We observe that the non-Gaussian deviation in

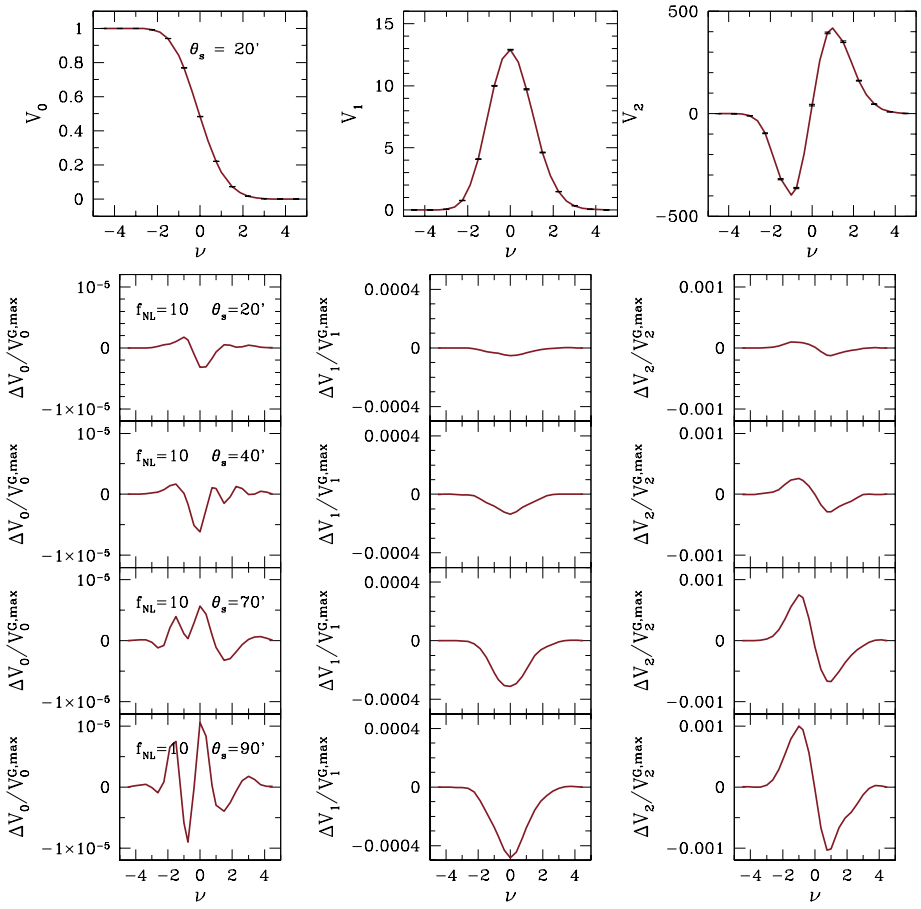

Figure 5.2: *Upper panels:* Plot of SMFs for $\tilde{I}_P$. *Lower panels:* The corresponding non-Gaussian deviation in SMFs with $f_{\rm NL} = 10$ for different smoothing scales.

all three SMFs of E mode have similar shape and comparable amplitude to that of the temperature field. Further, their error bars are also similar in size. Therefore, we can conclude that the E mode carries as much non-Gaussian information as the temperature and hence can provide independent constraint on primordial non-Gaussianity.

The Fig. 5.2 shows the plot of SMFs for $\tilde{I}_P$ in the three top panels. Their

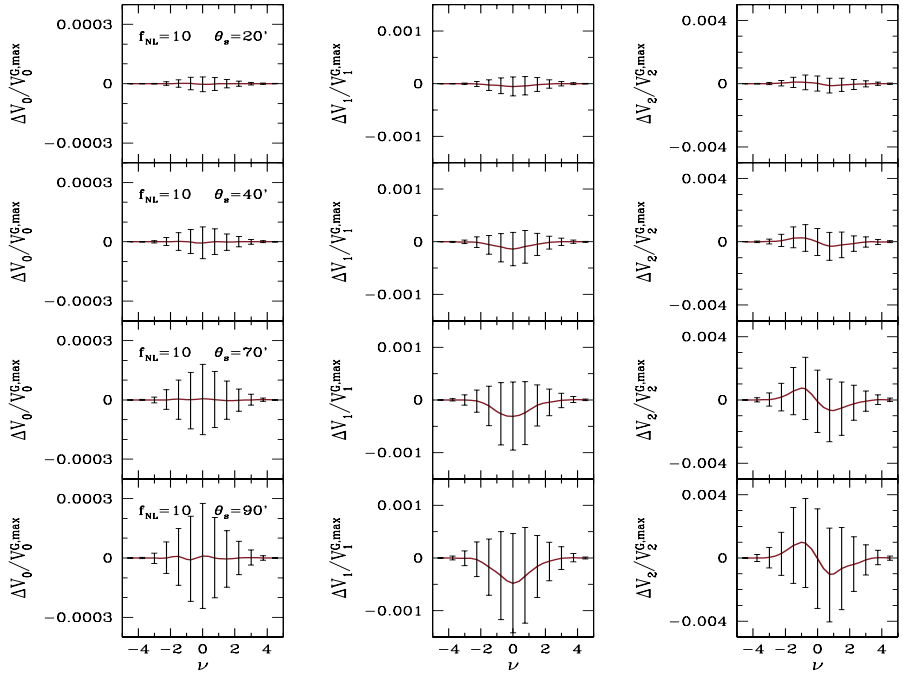

Figure 5.3: Plots show non-Gaussian deviations in SMFs with error bars for $\tilde{I}_P$ with the same $f_{\rm NL}$ value and smoothing angles as lower panels of Fig. 5.2, but are shown on a larger scale to show the large size of the error bars. The error bars are obtained from the sample variance of 1000 simulations.

non-Gaussian deviation for $f_{\rm NL} = 10$ with various smoothing angles without error bars are shown in the lower panels of Fig. 5.2 and the non-Gaussian deviation with error bars are shown in Fig. 5.3. The plots were again obtained by averaging over 1000 realizations and the error bars are the corresponding sample variance. The shapes of SMFs for $\tilde{I}_P$ are similar to the SMFs of a Gaussian field even though it has a Rayleigh distribution shown in Eq. 3.14. This is because of the Gaussian smoothing, which modifies the distribution of $\tilde{I}_P$ as discussed in Sec. 3.3. The amplitude of SMFs for $\tilde{I}_P$ field are similar to E mode

field at the same smoothing angle. The non-Gaussian deviation of $\tilde{I}_P$, shown in the lower panels of Fig. 5.2, shows a shape that is different from that of E mode. Further, the deviations of $\tilde{I}_P$ have much smaller amplitude than that of E mode at lower smoothing angles, while they both become similar to each other at higher smoothing angles. The plots in Fig. 5.3 are the same deviations as the Fig. 5.2, but are shown on a larger scale to highlight the large error bars. The larger error bars in the deviation of $\tilde{I}_P$ in comparison to E mode indicates that the statistical uncertainties in the non-Gaussian deviation of $\tilde{I}_P$ are much larger than that of E mode or temperature. This implies that $\tilde{I}_P$ field has very low capability to detect the primordial local type non-Gaussianity.

5.2.2 Betti numbers

Betti numbers for E mode and $\tilde{I}_P$ are calculated using the method described in Sec. 4.2.2. This method has not been tested for the accuracy that is required for the analysis of the present day high resolution maps. Therefore, the results obtained using this method are correct qualitatively, but are not suitable as yet for the accurate analysis and application to the observed map.

The threshold value ranging from $-4.5 \leq \nu \leq 4.5$ are chosen with the spacing of $\Delta\nu = 0.5$. The Betti numbers, β_0 and β_1, for Gaussian E mode field (left panel) and their corresponding non-Gaussian deviations (middle panel and right panel) are shown in Fig. 5.4. The plot is the average of 1000 realizations of `CMB`. The amplitude, shape, and size of error bars of non-Gaussian deviation for E mode field are again similar to the temperature field (refer to Fig. 3 and 8 of [84]).

The β_0 and β_1 for Gaussian case of $\tilde{I}_P$ (left panel) and their corresponding

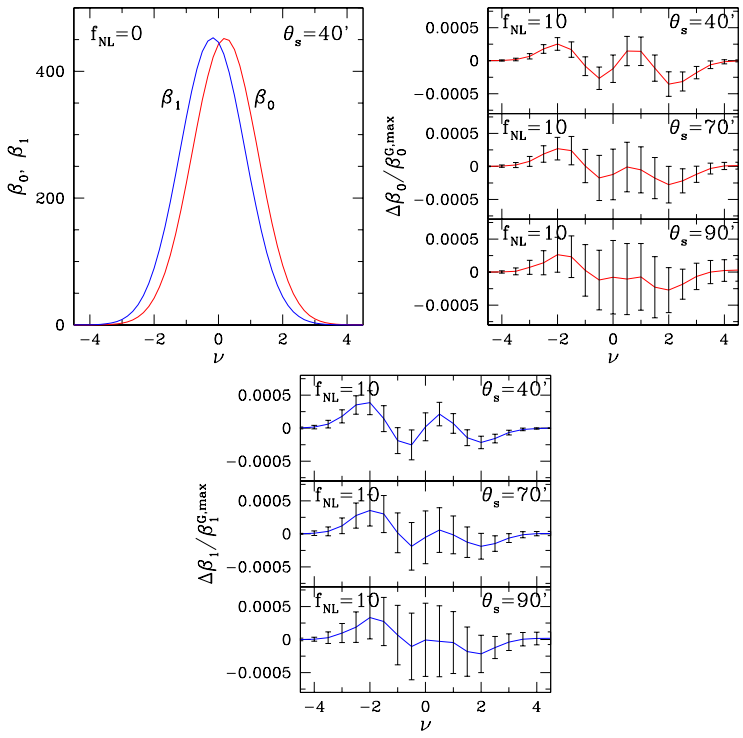

Figure 5.4: Betti numbers and their non-Gaussian deviations for E mode, with $f_{\rm NL} = 10$ and for various smoothing angles.

non-Gaussian deviations (middle and right panels). The plots are average over 1000 realizations. The amplitude of β_0 and β_1 for Gaussian case are similar to that of E mode field. The non-Gaussian deviation has an amplitude much smaller than the E mode for small smoothing angle, while at higher smoothing angle it becomes comparable. The plots shown in Fig. 5.5 are same as the Fig. 5.6 but are shown at larger scale to show the large error bars. This again shows that the $\tilde{I}_P$ field has low statistical power to detect the primordial local type non-Gaussianity.

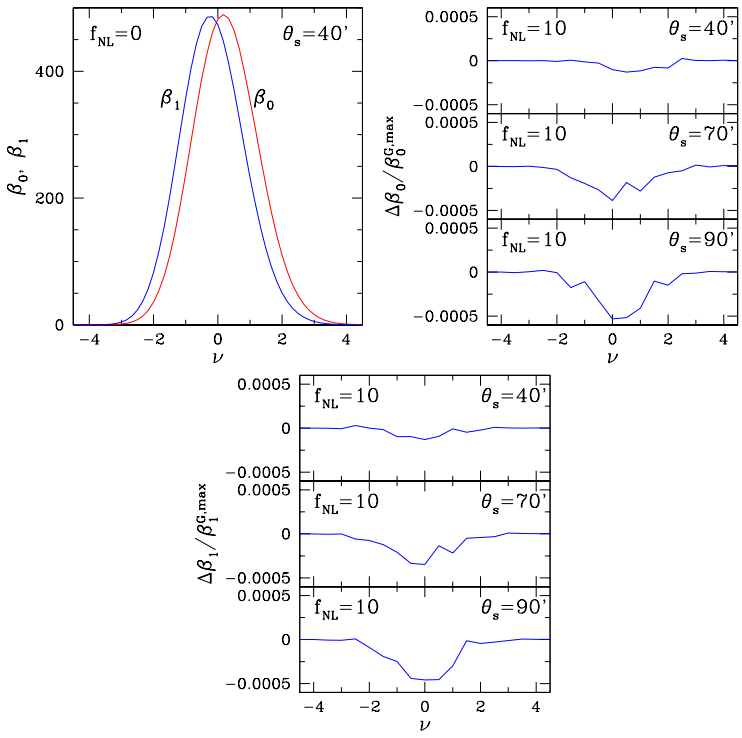

Figure 5.5: Betti numbers and their non-Gaussian deviations for $\tilde{I}_P$, with $f_{\rm NL} = 10$ and for various smoothing angles.

5.3 Statistical sensitivity of T, E and $\tilde{I}_P$ to primordial non-Gaussianity

The statistical sensitivity of temperature, E mode and $\tilde{I}_P$ to the non-Gaussian features present in them can be estimated and compared using the quantity, A, which is calculated by summing the absolute values of the non-Gaussian deviation expressed in terms of the sample variance from $\nu = -4.5$ to 4.5. A is defined as,

$$A = \Delta\nu \sum_{i=1}^{M} \frac{\left(\left|\Delta O(i)\right| / O^{\rm G,max}\right)}{\sigma_s(i)}, \tag{5.3}$$

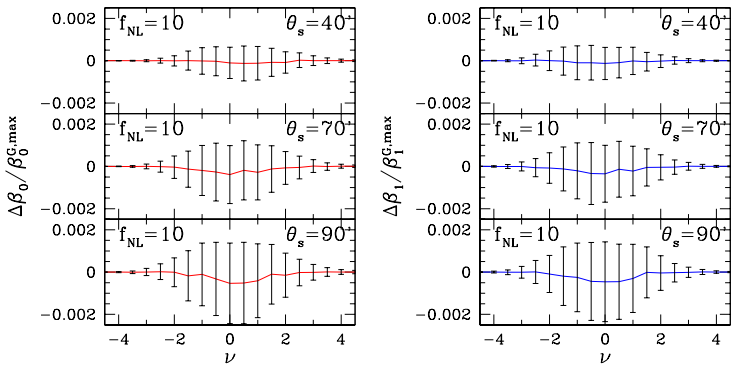

Figure 5.6: Plots show non-Gaussian deviations in Betti numbers with error bars for $\tilde{I}_P$ with the same $f_{\rm NL}$ value and smoothing angles as the middle and right panels of Fig. 5.5, but are shown on a larger scale to show the large size of the error bars. The error bars are obtained from the sample variance of 1000 simulations

where M is the number of threshold levels, O is either V_1, V_2, β_0 or β_1, and $\sigma_s(i)$ is the sample variance at each the threshold level, i.

The Table. 5.1 shows the value of A for the SMFs, V_1 and V_2. The number of threshold levels is $M = 13$ for V_1 and V_2. The values of A for temperature and E mode for these two observables have similar values. This implies that the E mode is capable of constraining primordial local type non-Gaussianity independently same as the temperature field. While the values of A for polarization intensity, $\tilde{I}_P$, is very low and hence it is not a suitable field for such analysis.

5.4 Discussion

We analyzed the non-Gaussian features in the E mode and $\tilde{I}_P$ fields using the SMFs and Betti numbers. The numerical calculations of non-Gaussian deviation in the SMFs and Betti numbers of E mode field showed that they have similar

Field	Smoothing angle (θ_s)	A for V_1	A for V_2
$\Delta T/T$	$40'$	27.3	22.8
	$70'$	21.3	14.5
	$90'$	18.4	26.0
E	$40'$	34.8	26.0
	$70'$	19.4	19.0
	$90'$	14.0	17.0
$\tilde{I}_P$	$40'$	1.2	1.2
	$70'$	1.8	1.6
	$90'$	1.7	1.5

Table 5.1: Table shows the value of A, defined in Eq. (5.3), for the SMFs, V_1 and V_2.

shape, amplitude, and size of error bars to that of the temperature field. We showed that the non-Gaussian deviations of I_P are smaller at small smoothing angles and that it becomes comparable to the temperature at higher smoothing angles. Additionally, their deviation has different shape and has very large error bars. We quantified the statistical sensitivity of each of these polarization fields for the presence of primordial local type non-Gaussianity. We found that the statistical sensitivity of E mode field is comparable to the temperature field while it is very low for the $\tilde{I}_P$ field. Hence from the theoretical point of view, these calculations suggest that the E mode field can provide an independent constraint on $f_{\rm NL}$ similar to that of the temperature field while $\tilde{I}_P$ is not capable of providing an independent constraint. Since we are ignoring the observational effect, this reduces the significance of the above findings. These conclusions are the same as that obtained from the analysis using the PDF of CMB fields. As the $\tilde{I}_P$ has distinct non-Gaussian deviation from that of the temperature and E

mode fields, if all these fields are used in conjunction then they will be useful for distinguishing different types of non-Gaussianity in the observational data. The PLANCK collaboration obtained constraint on local type non-Gaussianity, $f_{\rm NL}$, of 2.7 ± 5.8 using the temperature data alone [75], and later a value of 0.8 ± 5.0 was obtained by including the E mode data [76]. The error bars has shrunk by about 14%. As mentioned in Chapter. 3, here also these results confirms our expectations but it is not as pronounced as our calculations showed due to the higher noise levels in the polarization data.

Chapter 6

Signature of the primordial fluctuations in the Stokes parameters of CMB polarization

6.1 Introduction

We study the theoretical aspects of using the Stokes parameters Q/U for the analysis of CMB maps in this chapter. First, we analytically study the effect of rotation transformations about the line of sight on the SMFs of the Stokes parameter. Then we investigate the effect of the presence of local type primordial non-Gaussianity and tensor perturbation on the SMFs of Q/U. As our focus here is on the theoretical issues, we neglect the observational effects in this analysis.

This chapter is organized as follows. An analytic study of the effect of

rotation transformations about the line of sight on the variance of Stokes parameters and its gradients will be presented in the second section. In the third section, the numerical calculations of the affect on the SMFs due to the global rotations about the line of sight will be given. Further, an analysis of the residual error in the numerical calculation of contour length and genus of the Q/U fields will also be given in the section. Then the calculations and analysis of the non-Gaussian deviation in the Q/U fields will be shown in the fourth section. The effect of the presence of tensor perturbation on the SMFs for Q/U, and the number density of singularities in the polarization intensity will also be presented in the section. These results will be summarized and its implications will be discussed in the fifth section.

6.2 Variance of Stokes parameters and its gradients

We consider the Stokes parameters field, Q, U, and their gradients field, $\nabla Q, \nabla U$. Here, we investigate how the variance of these fields transform under rotations about the line of sight. We denote them as

$$\Sigma_0^X \equiv \langle XX \rangle, \quad \Sigma_1^X \equiv \langle \nabla X \cdot \nabla X \rangle, \tag{6.1}$$

where X is either Q or U and $\langle \dots \rangle$ indicates average over the surface of the sphere.

Let $Q(\theta, \phi)$, $U(\theta, \phi)$ be the Stokes parameters measured by an observer O along each line of sight of the sphere. While an another observer O' makes the measurement at each point, but with the co-ordinate system which is rotated

by the same angle α to that of the observer O at each line of sight. Let the Stokes parameters measured by the observer O' be $Q'(\theta,\phi)$, $U'(\theta,\phi)$, where Q', U' is given by Eq. (2.2).

Consider $Q', U', \nabla Q'$, and $\nabla U'$ along any arbitrary line of sight (θ,ϕ). We express these primed quantities in terms of unprimed quantities using Eq. (2.2). We denote the average over an ensemble of universes as $\langle \dots \rangle_{\rm ens}$. Then the primed quantities are squared and averaged over the ensemble of universes to get

$$\begin{aligned}
\langle Q'Q' \rangle_{\rm ens} &= \cos^2(2\alpha)\,\langle QQ \rangle_{\rm ens} + \sin^2(2\alpha)\,\langle UU \rangle_{\rm ens} \\
&\quad + \sin 4\alpha\ \langle QU \rangle_{\rm ens}, \qquad (6.2) \\
\langle U'U' \rangle_{\rm ens} &= \sin^2(2\alpha)\,\langle QQ \rangle_{\rm ens} + \cos^2(2\alpha)\,\langle UU \rangle_{\rm ens} \\
&\quad - \sin 4\alpha\ \langle QU \rangle_{\rm ens}, \qquad (6.3) \\
\langle \nabla Q' \cdot \nabla Q' \rangle_{\rm ens} &= \cos^2(2\alpha)\,\langle \nabla Q \cdot \nabla Q \rangle_{\rm ens} + \sin^2(2\alpha)\,\langle \nabla U \cdot \nabla U \rangle_{\rm ens} \\
&\quad + \sin 4\alpha\ \langle \nabla Q \cdot \nabla U \rangle_{\rm ens}, \qquad (6.4) \\
\langle \nabla U' \cdot \nabla U' \rangle_{\rm ens} &= \sin^2(2\alpha)\,\langle \nabla Q \cdot \nabla Q \rangle_{\rm ens} + \cos^2(2\alpha)\,\langle \nabla U \cdot \nabla U \rangle_{\rm ens} \\
&\quad - \sin 4\alpha\ \langle \nabla Q \cdot \nabla U \rangle_{\rm ens}. \qquad (6.5)
\end{aligned}$$

The Stokes parameters are expressed in terms of the spherical harmonic coefficients, $a_{E,\ell m}$ and $a_{B,\ell m}$, using Eq. (2.7) and Eq. (2.4), then we get

$$\begin{aligned}
Q &= -\frac{1}{2}\sum_{\ell m}\Big\{ a_{E,\ell m}\,(Y_{2,\ell m} + Y_{-2,\ell m}) \\
&\qquad + i a_{B,\ell m}\,(Y_{2,\ell m} - Y_{-2,\ell m})\Big\}
\end{aligned}$$

$$U = \frac{i}{2}\sum_{\ell m}\Big\{a_{E,\ell m}\left(Y_{2,\ell m}-Y_{-2,\ell m}\right) + ia_{B,\ell m}\left(Y_{2,\ell m}+Y_{-2,\ell m}\right)\Big\}. \quad (6.6)$$

Simplification of $\langle Q'Q'\rangle_{\rm ens}$ given by Eq. 6.2:

$$QU = \frac{i}{4}\sum_{\ell m\ell' m'}\Big\{a_{E,\ell m}a^*_{E,\ell' m'}\left(Y_{2,\ell m}+Y_{-2,\ell m}\right)\times\left(Y^*_{2,\ell' m'}-Y^*_{-2,\ell' m'}\right) + a_{B,\ell m}a^*_{B,\ell' m'}\left(Y_{2,\ell m}-Y_{-2,\ell m}\right)\times\left(Y^*_{2,\ell' m'}+Y^*_{-2,\ell' m'}\right) + \text{cross terms}\Big\}, \quad (6.7)$$

which is obtained by multiplying Q and U from the Eq. (6.6). We assume statistical isotropy of the perturbations,

$$\left\langle a_{E,\ell m}a^*_{E,\ell' m'}\right\rangle_{\rm ens} = \delta_{\ell\ell'}\delta_{mm'}\left\langle|a_{E,\ell m}|^2\right\rangle_{\rm ens} \quad (6.8)$$

$$\left\langle a_{B,\ell m}a^*_{B,\ell' m'}\right\rangle_{\rm ens} = \delta_{\ell\ell'}\delta_{mm'}\left\langle|a_{B,\ell m}|^2\right\rangle_{\rm ens} \quad (6.9)$$

$$\left\langle a_{E,\ell m}a^*_{B,\ell' m'}\right\rangle_{\rm ens} = 0. \quad (6.10)$$

Then the ensemble average of QU is

$$\langle QU\rangle_{\rm ens} = \frac{i}{4}\sum_{\ell m}\Big\{\langle|a_{E,\ell m}|^2\rangle_{\rm ens}\left(Y_{2,\ell m}+Y_{-2,\ell m}\right)\times\left(Y^*_{2,\ell m}-Y^*_{-2,\ell m}\right) + \langle|a_{B,\ell m}|^2\rangle_{\rm ens}\left(Y_{2,\ell m}-Y_{-2,\ell m}\right)\times\left(Y^*_{2,\ell m}+Y^*_{-2,\ell m}\right)\Big\}. \quad (6.11)$$

The coefficient of $|a_{E,\ell m}|^2$ and $|a_{B,\ell m}|^2$ in Eq. (6.11) are complex conjugate of

each other. The coefficient of $|a_{E,\ell m}|^2$ can be simplified as follows

$$\begin{aligned} & \left(Y_{2,\ell m} + Y_{-2,\ell m}\right)\left(Y^*_{2,\ell m} - Y^*_{-2,\ell m}\right) \\ = \;& Y_{2,\ell m}Y^*_{2,\ell m} - Y_{-2,\ell m}Y^*_{-2,\ell m} - Y_{2,\ell m}Y^*_{-2,\ell m} + Y_{-2,\ell m}Y^*_{2,\ell m}. \end{aligned} \tag{6.12}$$

Using the conjugate relation given by $Y^*_{s,\ell m} = (-1)^{s+m}Y_{-s,\ell -m}$, where s is the spin index, in the second term of the RHS of the above equation gives

$$\begin{aligned} Y_{-2,\ell m}Y^*_{-2,\ell m} &= (-1)^{2(m-2)}\, Y^*_{2,\ell -m}\, Y_{2,\ell -m} \\ &= Y^*_{2,\ell -m}\, Y_{2,\ell -m}. \end{aligned} \tag{6.13}$$

Since m in Eq. (6.11) is summed over from $-\ell$ to ℓ, and $a^*_{E,\ell m} = (-1)^m a_{E,\ell -m}$ from the reality condition on E mode field, we can rename $-m$ to m. This leads to the cancellation of the first two terms in Eq. (6.12). The same cancellation happens for the coefficient of $|a_{B,\ell m}|^2$ in Eq. (6.11). Finally we get,

$$\begin{aligned} \langle QU\rangle_{\rm ens} &= \frac{i}{4}\sum_{\ell m}\left\{\langle |a_{E,\ell m}|^2\rangle_{\rm ens} - \langle |a_{B,\ell m}|^2\rangle_{\rm ens}\right\} \\ &\quad \times\big(-Y_{2,\ell m}Y^*_{-2,\ell m} + Y_{-2,\ell m}Y^*_{2,\ell m}\big). \end{aligned} \tag{6.14}$$

The two terms in the second line of the above equation are complex conjugates. Using the conjugate relation we get

$$Y_{2,\ell m}Y^*_{-2,\ell m} = (-1)^{m-2}\, Y_{2,\ell m}Y_{2,\ell -m} \tag{6.15}$$

The spherical harmonic functions are of the form $Y_{2,\ell m} = f(\theta)e^{im\phi}$ and $Y_{2,\ell -m} = g(\theta)e^{-im\phi}$, hence each term in the coefficient of Eq. (6.14) is real. Therefore,

they cancel each other due to their opposites signs. Hence, we get

$$\langle QU \rangle_{\rm ens} = 0, \tag{6.16}$$

which is true at every point, (θ, ϕ), on the sphere. Using Eq. (6.16) in Eq. (6.2) we get

$$\langle Q'Q' \rangle_{\rm ens} = \cos^2(2\alpha) \langle QQ \rangle_{\rm ens} + \sin^2(2\alpha) \langle UU \rangle_{\rm ens}. \tag{6.17}$$

Assuming $\langle QQ \rangle_{\rm ens} = \langle UU \rangle_{\rm ens}$ we get

$$\langle Q'Q' \rangle_{\rm ens} = \langle QQ \rangle_{\rm ens}. \tag{6.18}$$

This relation is true along any arbitrary direction on the sky. Now taking the average $\langle \dots \rangle$ on both sides, we get

$$\langle \langle Q'Q' \rangle_{\rm ens} \rangle = \langle \langle QQ \rangle_{\rm ens} \rangle. \tag{6.19}$$

As the order of the average $\langle \dots \rangle$ and $\langle \dots \rangle_{\rm ens}$ can be reversed, so we have

$$\langle \langle Q'Q' \rangle \rangle_{\rm ens} = \langle \langle QQ \rangle \rangle_{\rm ens} \tag{6.20}$$

$$\left\langle \Sigma_0^{Q'} \right\rangle_{\rm ens} = \left\langle \Sigma_0^{Q} \right\rangle_{\rm ens} \tag{6.21}$$

Simplification of $\langle \nabla Q' \nabla Q' \rangle_{\rm ens}$ in the Eq. 6.4:
Similar to the case of ensemble average on QU, we get for $\langle \nabla Q \cdot \nabla U \rangle_{\rm ens}$ as

$$\langle \nabla Q \cdot \nabla U \rangle_{\rm ens} \;=\; \frac{i}{4} \sum_{\ell m} \Big\{ \langle |a_{E,\ell m}|^2 \rangle_{\rm ens} \nabla \left(Y_{2,\ell m} + Y_{-2,\ell m} \right) \times \nabla \left(Y^*_{2,\ell m} - Y^*_{-2,\ell m} \right)$$

$$+\langle|a_{B,\ell m}|^2\rangle_{\rm ens}\nabla\left(Y_{2,\ell m}-Y_{-2,\ell m}\right)\times\nabla\left(Y^*_{2,\ell m}+Y^*_{-2,\ell m}\right)\Big\}. \tag{6.22}$$

Simplifying the factor containing gradients of the $Y_{\pm2,\ell m}$'s as

$$\begin{aligned}&\nabla\left(Y_{2,\ell m}+Y_{-2,\ell m}\right)\cdot\nabla\left(Y^*_{2,\ell m}-Y^*_{-2,\ell m}\right)\\&=\nabla Y_{2,\ell m}\cdot\nabla Y^*_{2,\ell m}-\nabla Y_{-2,\ell m}\cdot\nabla Y^*_{-2,\ell m}\\&-\nabla Y_{2,\ell m}\cdot\nabla Y^*_{-2,\ell m}+\nabla Y_{-2,\ell m}\cdot\nabla Y^*_{2,\ell m}.\end{aligned} \tag{6.23}$$

Following the same steps as in the case of Eq. (6.12), the first two terms gets canceled when the conjugate relation is used. Further Simplification leads to the conclusion that the remaining terms are real and hence cancel each other out. Therefore,

$$\langle\nabla Q\cdot\nabla U\rangle_{\rm ens}=0. \tag{6.24}$$

Again, this zero correlation is true at every point (θ,ϕ) on the sphere. Using Eq. (6.24) in Eq. (6.4) we get

$$\langle\nabla Q'\cdot\nabla Q'\rangle_{\rm ens}=\cos^2(2\alpha)\,\langle\nabla Q\cdot\nabla Q\rangle_{\rm ens}+\sin^2(2\alpha)\,\langle\nabla U\cdot\nabla U\rangle_{\rm ens} \tag{6.25}$$

Assuming $\langle\nabla Q\cdot\nabla Q\rangle_{\rm ens}=\langle\nabla U\cdot\nabla U\rangle_{\rm ens}$ and taking the average $\langle\dots\rangle$ on both sides, we get

$$\langle\langle\nabla Q'\nabla Q'\rangle_{\rm ens}\rangle=\langle\langle\nabla Q\nabla Q\rangle_{\rm ens}\rangle \tag{6.26}$$

Interchanging the order of the average $\langle\rangle$ and $\langle\rangle_{\rm ens}$, we get

$$\langle\langle\nabla Q'\nabla Q'\rangle\rangle_{\rm ens}=\langle\langle\nabla Q\nabla Q\rangle\rangle_{\rm ens} \tag{6.27}$$

$$\left\langle \Sigma_1^{Q'} \right\rangle_{\rm ens} = \left\langle \Sigma_1^{Q} \right\rangle_{\rm ens} \tag{6.28}$$

We have shown that the variances of Stokes parameters and its gradients are invariant under a global rotation of same angle about each line of sight. For the case when the rotation angle varies for different line of sight, the rotation factors will be part of the integrand. In order to prove the above invariance it is not necessary to carry out the integration explicitly and hence the above proof is applicable for direction dependent rotation also. But this will not hold for the case of incomplete sky due to the masking of Galactic and point sources, as the relations in Eqs. (6.8) and (6.9) are no longer applicable because the statistical isotropy is broken in this case. Therefore in the case of incomplete sky, $\langle \Sigma_0^{Q,U} \rangle_{\rm ens}$ and $\langle \Sigma_1^{Q,U} \rangle_{\rm ens}$ are not invariant under rotations about the line of sight.

6.3 Scalar Minkowski Functionals of Stokes parameters

We investigate the effect on the SMFs of Q and U due to the rotations about the line of sight. We expect the fields Q and U to have Gaussian distribution when the primordial fluctuations, both the scalar and tensor type, are Gaussian. Then their SMFs will be given by Eq. (4.7). We denote $r_c = \dfrac{\sigma_0}{\sigma_1} = \dfrac{\sqrt{\Sigma_0}}{\sqrt{\Sigma_1}}$, which is referred to as the correlation length of the structures of a random field. From the Eq. (4.7), the amplitude of SMFs are dependent on the powers of r_c. As shown in Sec. 6.2, the variance Σ_i^X for $X = Q, U$ and hence r_c are invariant under arbitrary rotation about each line of sight. Therefore, the SMFs must also be invariant. But this does not hold for incomplete sky. In the subsequent

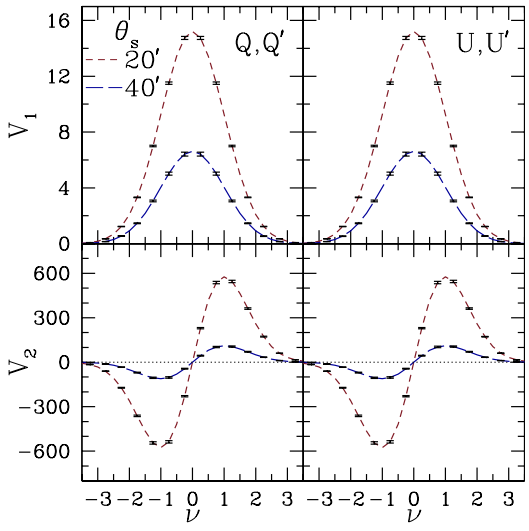

Figure 6.1: The plot of V_1 is shown for Q, Q' (left panel) and U, U' (right panel) for the smoothing angles $\theta_s = 20'$ (small red dashed lines) and $\theta_s = 40'$ (long blue dashed lines). Q', U' are obtained by a global rotation of about $\alpha = 45^\circ$ in each line of sight. The plots corresponding to the primed and unprimed are indistinguishable, and they show that the amplitudes are invariant under global rotation. All these plots are obtained by averaging over 1000 realizations and the error bars are the corresponding sample variance. Similarly, the plots of V_2 are shown in the lower panels.

analysis, we will only focus on the full sky maps.

We consider simulations of Q and U fields using scalar perturbation with Gaussian distribution. The fields Q' and U' are obtained from Q and U by global rotation with an angle of about $\alpha = 45^\circ$ about each line of sight. We use `SG` method for the calculation of `SMF`s. The contour length and genus of all these fields are shown in Fig. 6.1 for smoothing angles $\theta_s = 20', 40'$. The plots show that the contour length and genus are invariant under global rotation. We obtain the same result for different choices of α.

We numerically calculate the residual error defined in Eq. (4.15) for Q and

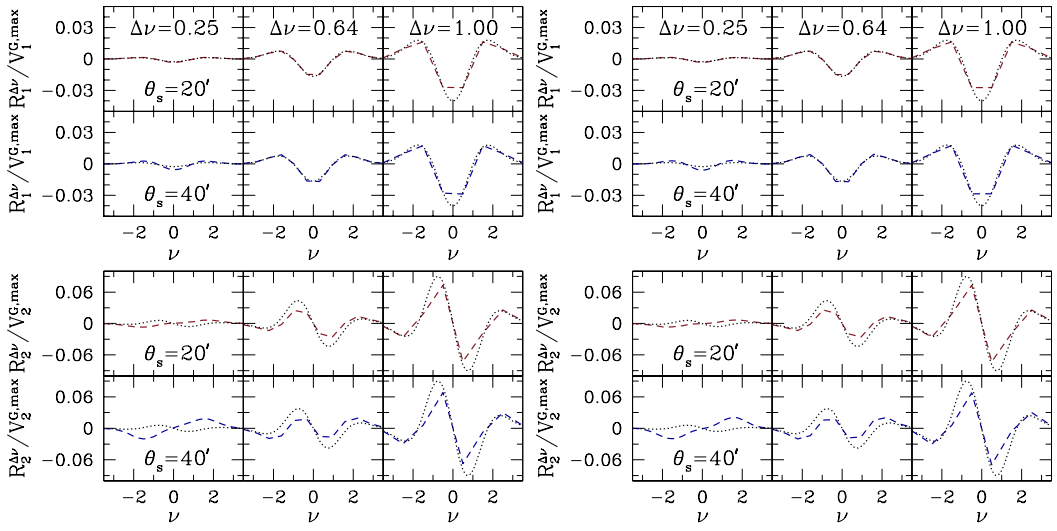

Figure 6.2: Upper panels show the residuals defined in Eq. (4.15) of V_1, for Q (left) and U (right) with the smoothing angles $\theta_s = 20'$ (red dashed lines) and $\theta_s = 40'$ (blue dashed lines) with $\Delta\nu = 0.25, 0.64, 1$. There are average over 1000 maps. The analytic form of residual given by (4.16) for a Gaussian field is shown with black dotted lines. Lower panels show the same but for the residuals of V_2.

U (dashed lines) and the analytic form obtained from Eq. (4.16) for a Gaussian field (black dotted lines), which are shown in Fig. 6.2 for different smoothing angles $\theta_s = 20', 40'$. The calculations for various bin sizes $\Delta\nu = 0.25, 0.65, 1$ are also shown. In the analytic case, the residual increase with larger bin sizes and they are not affected by the variation of smoothing angle. The residual error in the contour length for Q and U are nearly same and appears to agree with the analytic form. When we zoom into the plots, we observe that there is noticeable difference between the dashed and dotted lines at small bin sizes. This difference is more significant at larger smoothing angles. While, they show good agreement at larger bin size, such as, for the case of $\Delta\nu = 1$. Similar

kind of behavior is observed in the genus residuals but the difference between the dashed and dotted lines at small bin sizes are much larger. Further, there is a small difference between the residuals in Q and U.

The residual calculations was repeated for temperature maps and we have reproduced the results in [118]. Therefore, the disagreement between the numerically calculated residual and the analytic form at small bin size is not due to the errors in the numerical calculations. This disagreement may be due to the spin-2 nature of Q and U. Since there is a good agreement in the case of temperature which is a scalar field. In particular during the implementation of the `SG` method, the covariant derivative of a scalar field are used instead of the appropriate covariant derivative of spin-2 fields relevant for Q and U fields, which could be the reason behind the disagreement.

6.4 Aspects of primordial fluctuation in the Stokes parameters of CMB

6.4.1 Primordial non-Gaussianity

We investigate the effect on the `SMF`s of Q and U fields due to the presence of primordial local type non-Gaussianity. Our aim here is to study the non-Gaussian features in these fields, hence we use full sky maps. In this analysis, the tensor-to-scalar ratio, r, is taken to be zero. We use the non-Gaussian E mode simulations provided by Elsner and Wandelt. Then the Gaussian and non-Gaussian Q/U maps are constructed with the chosen $f_{\rm NL}$ values. These maps use `HEALpix` convention described in Sec. 2.1 for defining the $x - y$ coordinates at each line of sight. Hence, we compare maps that uses the same

$x-y$ coordinates at each line of sight. We mainly use the SG method to estimate the SMFs of these fields. Nevertheless, we have repeated the calculations using the CND_REG2D method and the results agree with each other.

The SMFs of Q and their non-Gaussian deviation with $f_{\rm NL} = 1000$ are shown in Fig. 6.3. The calculations of U are the same as Q as expected, hence are not shown. The top panels show SMFs for Gaussian case and non-Gaussian case for $f_{\rm NL} = 1000$ with the smoothing angle $\theta_s = 5'$. The plots corresponding to these two cases are indistinguishable by the eye. The lower panels show the non-Gaussian deviations with error bars for $f_{\rm NL} = 1000$. The non-Gaussian deviations at lower $f_{\rm NL}$ values are statistically noisy. With the main intention to study the shape and amplitude of non-Gaussian deviation in Q, we have chosen unrealistically large values of $f_{\rm NL}$. The amplitude of the non-Gaussian deviations in Q are much smaller than that obtained from the temperature (refer to Fig. 2 of [68]) and E mode (refer to Fig. 5.1). The shape of deviation is different from the temperature and E mode fields. The non-Gaussian deviation in genus is similar to the cubic order primordial non-Gaussianity parametrized by $g_{\rm NL}$ (see Fig. 4 of [105] and Fig. 1 of [69])

In order to apply this non-Gaussian analysis for masked observational data, we need to compute the SMFs of the corresponding Gaussian component. This can be done by calculating the amplitude of SMFs using the Eq. 4.7, which depends on the variances of the field. This method is approximate and is applicable only for the weakly non-Gaussian fields. Then the non-Gaussian deviation can be estimated by subtracting the SMFs of the Gaussian component from that obtained from the observational data. But the comparison between the simulation and observational data is possible only when both the map have the same $x - y$ coordinate choices along each line of sight.

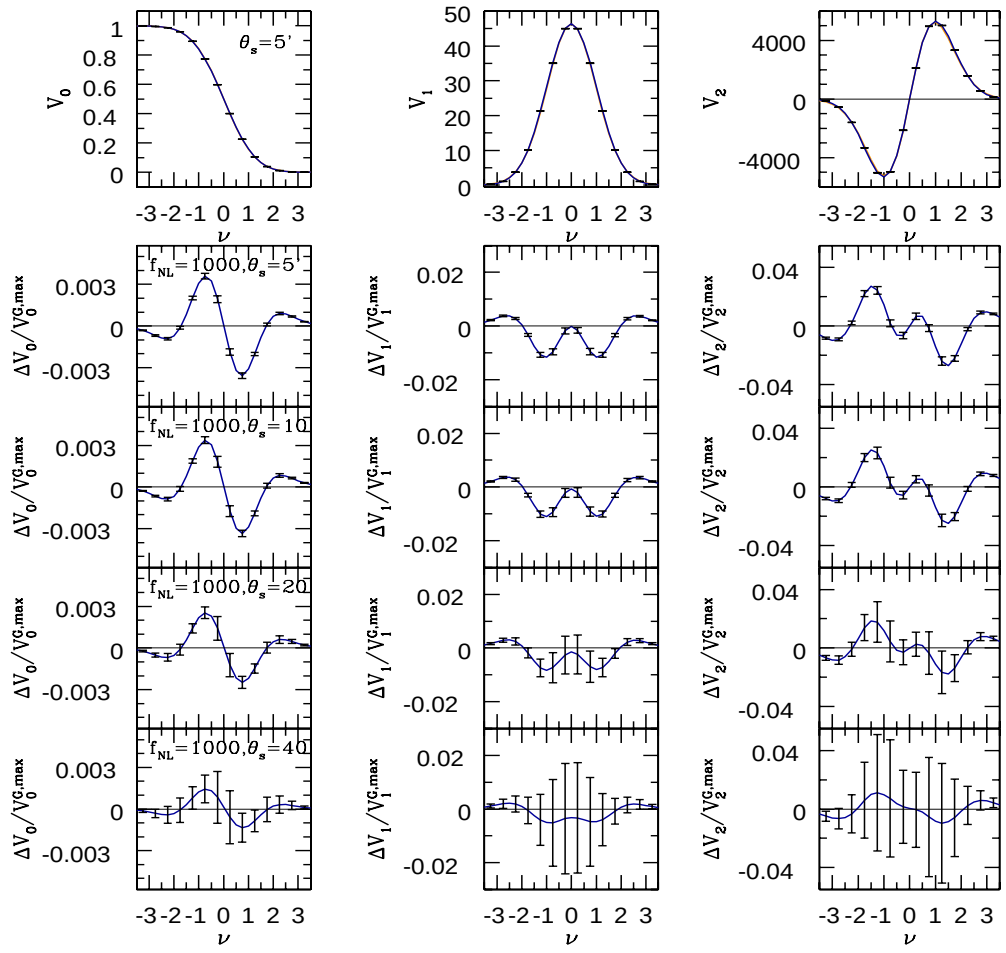

Figure 6.3: The top three panels show the SMFs for Gaussian and non-Gaussian case with $f_{\rm NL} = 1000$. The difference between the Gaussian and non-Gaussian case is small, and it is indistinguishable by the eye. The lower panels shows the corresponding non-Gaussian deviations for different smoothing angles. We have chosen large values of $f_{\rm NL}$ as the deviation becomes statistically noisy at small values. These plots are average over 1000 maps and the error bars are their sample variances.

6.4.2 Primordial tensor perturbations

Here, we investigate the effect of tensor perturbations on the Q and U fields. We use the simulations of E mode and B mode with Gaussian distribution. For

this simulation, we use ΛCDM cosmological parameters: $\Omega_c h^2 = 0.1198,\ \Omega_b h^2 = 0.02225,\ H_0 = 67.27,\ n_s = 0.9645,\ \ell n(10^{10} A_s) = 3.094,\ \tau = 0.079$, taken from the 2015 PLANCK data [51]. These maps have resolution with $N_{\text{side}} = 1024$.

In Sec. 3.2, we showed that the PDF of I_P with a Gaussian Q and U, has Rayleigh distribution. Further in Sec. 3.3, we found that the PDF of I_P varies noticeably with the tensor-to-scalar ratio, r. Since the PDF is completely described by σ_0, the effect on it due to the presence of tensor perturbation can be understood by studying the effect on the σ_0. Here we take this observation further and study the variation of σ_i's and r_c^{-1} with r. Then we discuss its impact on various fields.

The plot showing the variation of σ_0 and σ_1 with r are shown in Fig. 6.4. The chosen r values range from 0.05 to 0.2. In order to see the variation at different scales, two smoothing angles $10'$ and $90'$ are chosen. We observe that σ_0 and σ_1 increases due to the presence of tensor perturbation. The slope of these plots vary with the smoothing scale. On visual inspection these plots appear to be linear, but actually σ_0 and σ_1 are not linear in r which can be noted when we plot r_c versus r.

The plot of r_c^{-1} vs r, for $r = 0.05$ to 0.2 are shown in Fig. 6.5 with different smoothing scales. The presence of tensor perturbation results in the decrease of the value r_c^{-1}. Further, we observe that r_c^{-1} decreases with the increasing r. The amplitude of SMFs are proportional to the power of r_c^{-1}. Hence these observations indicate than the amplitude of SMFs will decrease with r. Since $V_1 \propto r_c^{-1}$ and $V_2 \propto r_c^{-2}$, the genus is more sensitive than the contour length to the presence of tensor perturbation.

For the polarization intensity, it was shown by Naselsky and Novikov [125] that its SMFs, V_i's, are proportional to r_c^{-i}, for $i = 1, 2$. Hence the behavior

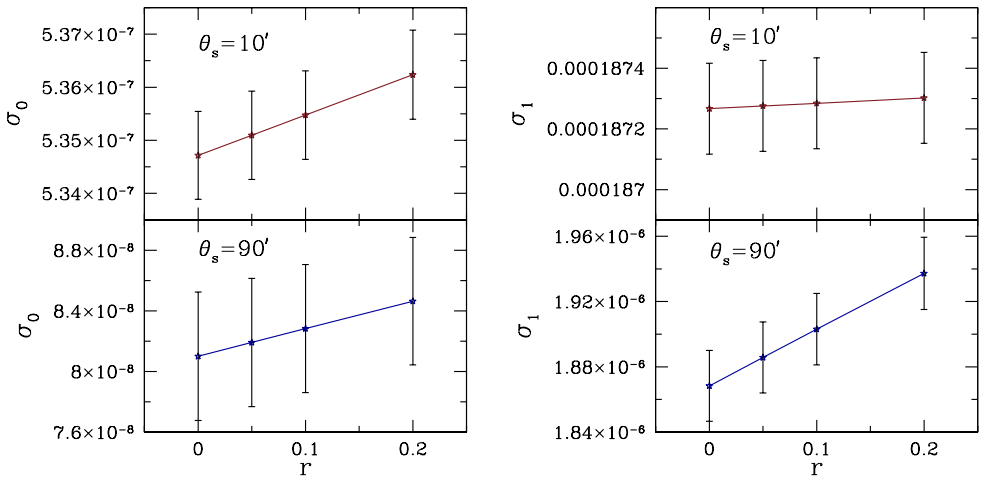

Figure 6.4: The plot showing the variation of σ_0 with r for smoothing angles $\theta_s = 10', 90'$ is shown in the left panel. The corresponding plot of σ_1 is shown in the right panel. The star symbol indicate the r values where the calculations was done. These plots are average over 1000 simulations.

of r_c^{-1} implies that the amplitude of the SMFs for I_P will also decrease with r. The points on the CMB field where $Q = 0 = U$ and hence $I_P = 0$, are referred to as singular points. The number density of singularities in CMB polarization intensity were studied in [126, 127]. Let $N_{\rm sing}$ denote the number density of singularities. In [125], it was also shown that $N_{\rm sing} = 1/4\pi r_c^2$. Therefore, the behavior of r_c^{-1} shows that $N_{\rm sing}$ is sensitive to the presence of tensor perturbation and it decreases with r.

6.5 Discussion

We analyzed the theoretical aspects related to the usage of Q/U fields for the searches of primordial non-Gaussianity using SMFs. We showed analytically

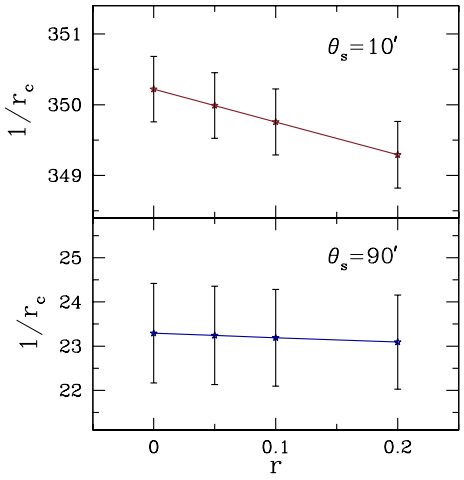

Figure 6.5: The plot of r_c^{-1} versus r with smoothing angles $\theta_s = 10', 90'$. These are average over 1000 simulations. The star symbol indicate the r values where the calculations was done.

that the SMFs of Gaussian Q/U fields are invariant under rotation transformations about the line of sight. This statement holds only for the maps with full sky coverage and hence it will break down for the case of incomplete sky. Then we studied the effect of local type primordial non-Gaussianity on the SMFs of Q/U fields. We found that the amplitude of non-Gaussian deviation is about an order of magnitude lower than that of temperature and E mode, and further their shape is also different. For the analysis of data from the future experiments which are sensitive enough to detect tiny traces of non-Gaussianity in the CMB fields, the above findings will be useful for distinguishing local type non-Gaussianity from different physical sources. We also studied the effect of the presence of tensor perturbation on the morphological properties of polarization fields. We found that the SMFs of Q/U and I_P are sensitive to the presence of tensor perturbations and that their amplitude decreases with r.

Further, we showed that the number density of singularities in the I_P field is also sensitive and it also decreases with r. These findings can be useful for the searches of B mode polarization in the future experiments. As we have neglected the observational effects in the above analysis, this will decrease the statistical significance of these results.

Chapter 7

Application of Tensor Minkowski Functionals to CMB analysis

7.1 Introduction

In this chapter, we introduce Tensor Minkowski Functionals as a new statistical tool for the analysis of CMB maps. Since these are tensor generalization of SMFs, these are capable of capturing more morphological features in the maps. We develop a code to compute TMFs for a random field on a plane. Then we analyze and quantify the inaccuracies in the numerical computation of α and β, defined in Eq. (4.34). Finally, we obtain the theoretical prediction for the value of α and β assuming standard ΛCDM model.

This chapter is organized as follows. In the second section, we describe the algorithm used to compute α and β for a given excursion set on a plane. We

also quantify the numerical errors in these quantities due to pixelization. In the third section, the numerical computation of the variation of α and β with the threshold value is presented for simulated `CMB` fields. We also give an estimate of α and β expected for a Gaussian and isotropic `CMB` fields. A summary of these results and a discussion of its implication will be given in the last section.

7.2 Numerical computation of α and β for an excursion set on a plane

7.2.1 Algorithm to compute α and β

Consider an excursion set on an Euclidean plane. In order to compute α, β, defined in Eq. (4.34), for the excursion set, we first compute $W_2^{1,1}$ given by Eq. (4.29) for each individual structure. For this computation, we follow the algorithm in [123]. The code that we have built based on this algorithm will be referred to as the `TMFCode`. Here, we describe this algorithm.

Consider a planar field which is pixelized with $N_{\rm pix}$x$N_{\rm pix}$ number of pixels. The shape of each pixel is considered to be a square. The index (i, j) labels the pixels, which ranges from 1 to $N_{\rm pix}$ along each dimension. The excursion set, K, picks a finite number of pixels out of these pixels. First, the individual structures in the excursion set are identified and labeled. For a pixel say (i_1, j_1) that belongs to the excursion set, the neighbouring pixels and all the pixels connected to it are labeled as structure 1. Then it scans for a pixel say (i_2, j_2) contained in K but which does not belong to the structure 1, identifies all the pixels connected to it, and labels them as structure 2. This process is repeated until all the structures in the excursion set are identified and labeled.

Next, the line segments which forms the boundaries of the structures needs to be constructed, which uses the marching square algorithm. The entire area of the planar field is divided into square shaped area segments with the pixel centers of the four adjacent pixels as the vertices. Each of these area segments is assigned with none or one or two line segments based on whether the pixel centers at the four adjacent vertices belongs to the excursion set or not. A given pixel center may either belong to the excursion set or not, so it has two possibilities. Therefore, there are in total 16 possibilities for different combinations of four adjacent pixel centers. The area segments for all these different combinations are shown in Fig. 7.1. The black and white circles are the pixel centers. The black circles are the pixel centers which belong to the excursion set while white circles corresponds to those which are not contained in the set. The line segments for each of these area segments are constructed as follows: the point on the edges, which connect black circle and white circle, of the area segment where the field value becomes equal to threshold value is found by linear interpolation, and then the line segments are constructed with these points as the vertices. The direction for these line segments, which is part of a closed polygon, are assigned such that it is counterclockwise for a closed polygon enclosing a connected region and clockwise if it encloses a hole. The line segments for all the combinations of four adjacent pixel centers are also shown in Fig. 7.1. These line segments which form the boundaries of the structures, defines the edges vector, $\vec{e}_{(i,i+1)}$ for $i = 1,\ldots n_v - 1$, in Eq. (4.29).

Finally, the tensor, $W_2^{1,1}$, is computed for each structure using the Eq. (4.29). Then the ratio of eigenvalues, α, β, are computed using two different ways of averaging as shown in Eq. (4.34).

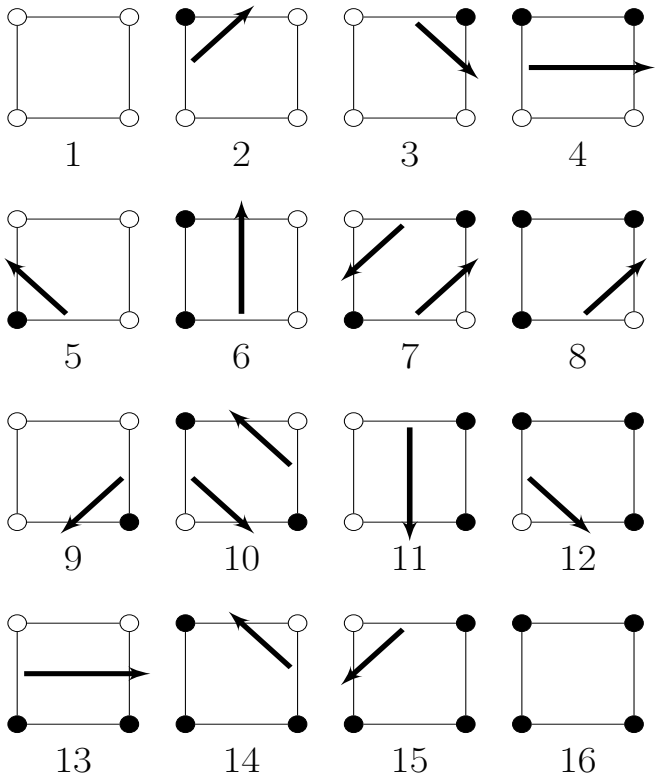

Figure 7.1: The boundary and direction are shown for different configurations of four adjacent pixels. The small black and white circles are pixel centers. The black circles are pixels which belong to the excursion set while white circles are not.

7.2.2 Anisotropy measure of an elliptical structure on a plane

In a pixelized space, a continuous contour is approximated by a polygon which results in numerical inaccuracy in the computation of $W_2^{1,1}$. We consider an excursion set containing an elliptically shaped structure as shown in the Fig. 4.5.

The β value for an ellipse from analytic formula in Eq. (4.26), the value

q/p	β from analytical formula	β from `TMFCode`			% error
		1000^2 pixels	2000^2 pixels	3000^2 pixels	
1.0000	1.0000	1.0000	1.0000	1.0000	0.0
0.8000	0.7154	0.7642	0.7641	0.7641	6.8
0.7346	0.6293	0.6902	0.6901	0.6901	9.7
0.7262	0.6185	0.6790	0.6803	0.6799	9.9
0.6000	0.4638	0.5418	0.5417	0.5418	16.8
0.5000	0.3518	0.4371	0.4370	0.4370	24.2
0.3000	0.1602	0.2432	0.2433	0.2432	51.8
0.1000	0.0274	0.0739	0.0741	0.0741	170.4

Table 7.1: The Column 2 shows the β values obtained from the analytic formula in Eq. (4.26) for different aspect ratios q/p in Column 1. The Column 3 shows the β values from the numerical computation using `TMFCode` for different resolutions. The percentage numerical error in β for 3000^2 pixels are shown in Column 4.

from numerical computation using `TMFCode` and the corresponding numerical error due to pixelization are shown for different aspect ratios in Table. 7.1. This is shown for different resolutions 1000^2, 2000^2, and 3000^2 pixels. In this case, $\alpha = \beta$ since the excursion set consists of a single structure. The β value obtained from numerical computation does not significantly vary with the resolution for a fixed aspect ratio. The numerical error in β increases as the aspect ratio, q/p, is decreased. The continuous contour of the ellipse is approximated with a polygon, hence it fails to capture the true curvature at

every point on the contour. This numerical error is due to the pixelization. The section of the contour with high curvature results in large error in the numerical computation of β. The approximation to polygon systematically over estimates the value of β relative to those from the analytic formula for the continuous ellipse. This observation will be used to approximately correct for the numerical error due to pixelization in β for `CMB` fields.

7.2.3 Orientation measure of two elliptical structure on a plane

We study the numerical error in α due to pixelization. Consider an excursion set with two ellipses with fixed aspect ratio $q/p = 0.5$. Due to pixelization, these ellipses will be approximated as polygons. α of the excursion set using analytic formula in Eq. (4.26), α from numerical computation using `TMFCode` for different resolution, and the numerical error are shown for different relative orientation between the major axes of the two ellipses in Table. 7.2. The Column 1 shows the angle between the major axes of the ellipses. The case where the ellipses are perfectly aligned with each other corresponds to $0°$. While when the major axes of the ellipses are perpendicular to each other, they are completely unoriented with each other. The value of α does not significantly vary with the resolutions for a fixed relative orientation between major axes of the ellipses. The numerical error due to pixelization decreases as the ellipses become more and more unoriented to each other for a fixed resolution. When the major axes of the ellipses gets completely oriented then $\alpha = \beta$. Therefore, when the ellipses are highly aligned then the numerical error in α will become equal to the numerical error in β. As the ellipses become unaligned with each

Angle between major axis of the ellipses	α from analytic formula	α from `TMFCode`			% error
		1000^2 pixels	2000^2 pixels	3000^2 pixels	
0°	0.3518	0.4369	0.4371	0.4369	24.2
20°	0.3787	0.4668	0.4668	0.4674	23.4
45°	0.4936	0.5665	0.5660	0.5661	14.7
60°	0.6132	0.6720	0.6724	0.6727	9.7
90°	1.0000	1.0000	1.0000	1.0000	0.0

Table 7.2: The Column 2 shows α for an excursion set with two ellipses obtained from the analytic formula in Eq. (4.26). α obtained from the numerical computation using `TMFCode` are shown in Column 3 for different resolutions. The percentage numerical errors for the case of 3000^2 pixels are given in Column 4. These are shown for different relative orientation angle between the major axes of the ellipses in Column 1.

other, the α will become close to one irrespective of the value of β. Therefore, the numerical error also decreases. In the application to data whose α is close to one, the numerical error due to pixelization can be neglected. While when the data has α close to β, then the numerical error will no longer be negligible. These results will be used during the analysis of `CMB` fields.

7.3 α and β for an excursion set on a sphere

7.3.1 Stereo-graphic projection and its effect on α and β

In order to compute α and β for an excursion set of a field on a sphere, we use stereo-graphic projection to map the field on a sphere onto a plane. A brief description of stereo-graphic projection was given in the Subsection. 4.2.2. This is a conformal map and hence it preserves the angle and shape of the structures. While the size of the structure will not be preserved. Therefore the structures that lie further from the poles will have same shape but its size will be enlarged. This effect can be observed in Fig. 7.2 where the projection of elliptically shaped structure on the sphere is shown for the ellipse located at different latitude of the sphere. When the structure is enlarged by a then $W_2^{1,1}$ will scale as a. This is because from Eq. 4.17, $\vec{r}$ scales as a, κ scales as a^{-1}, dl scales as a while $\hat{n}$ is invariant. Hence the two structures with the same shape but with different size will have equal β. Therefore, the stereo-graphic projection is a good choice for the computation of β.

Consider a set of structures having a given distribution of shapes. These structures can be arranged with different relative alignment in many ways. The value of α measures the extent of orientation in each of this arrangement of structures. In other words, α measures the net orientation for a given distribution of shapes. In the case of stereo-graphic projection, as the structures away from the poles are scaled, it changes the distribution of shapes in the structures and hence effects the value of α leading to errors. Since the scaling effect is significant for structures close to the equator, these errors can be reduced

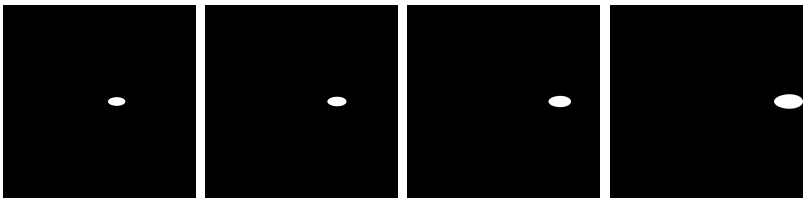

Figure 7.2: Images show the stereo-graphic projection of excursion set with an elliptically shaped structure, with an aspect ratio of 0.5, which is located at different latitude on the sphere. We can observe that the shape of the structure is preserved while the size gets enlarged as it becomes closer to the equator of the sphere.

by removing structures close to the equator from the excursion set. A simple analysis of these errors are presented in the next subsection.

7.3.2 Orientation measure for structures of an excursion set on a sphere

The quantity α is capable of detecting any alignment in the structures on a plane (refer to Subsection. 7.2.3). Here, we extend this study to the case of an excursion set on a sphere. We consider an excursion set with many elliptically shaped structures with fixed aspect ratio of 0.7 on a sphere, whose major axes are all oriented towards the pole. This implies that these structures possess a net orientation. This sphere as seen from two different directions and the corresponding stereo-graphic projection with sheet of the paper as the projection plane are shown in Figs. 7.3 and 7.4.

The value of α (Column 2) and $\mathscr{O}$ (Column 3), defined in Eq. (4.35), for a sphere with elliptically shaped structures with different projection planes (Column 1) are shown in Table. 7.3. A projection plane is specified with the

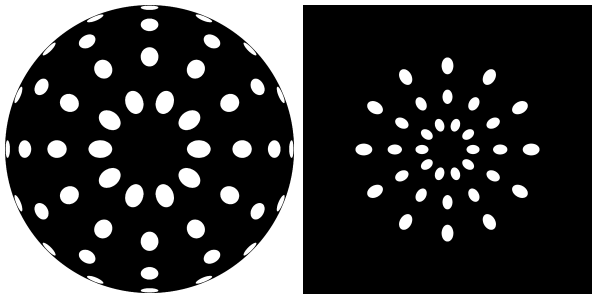

Figure 7.3: Image shows a sphere containing elliptically shaped structures (left image) as seen from above the north pole and the corresponding stereo-graphic projection (right image) with sheet of the paper as projection plane.

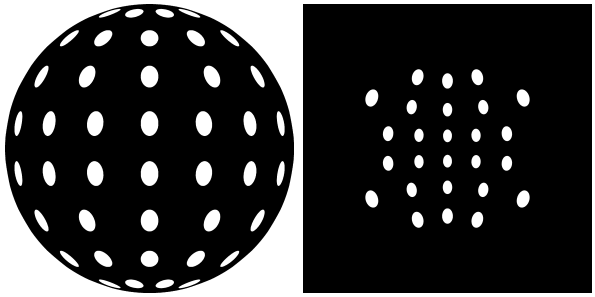

Figure 7.4: Image shows a sphere containing elliptically shaped structures (left image) as seen from any point just above the equator and the corresponding stereo-graphic projection (right image) with sheet of the paper as projection plane.

angle between the equatorial plane and the projection plane, which is represented as δ. The projection images for the case of $\delta = 0°$ is shown in the right image of Figs. 7.3 while for $\delta = 90°$ in Fig. 7.4. For the case of $\delta = 0°$, the structures show negligible orientation. While the structures are highly oriented when $\delta = 90°$. These images show that the orientation of structures depend on the choice of projection plane. We estimate α and $\mathscr{O}$ for these cases. For the case of $\delta = 0°$, the value of α is close to 1 and $\mathscr{O}$ is close to 0, which indicates that the structures have negligible orientation. While for the case of $\delta = 90°$,

Angle b/w equatorial plane and projection plane (δ)	α	$\mathscr{O}$
0°	0.9963	0.0107
45°	0.9322	0.2204
90°	0.7259	0.9259

Table 7.3: The table shows the value of α (column 2) and $\mathscr{O}$ (column 3) which is defined in Eq. 4.35 for different projection planes (column 1). For this calculations, a sphere containing elliptically shaped structures are considered.

we get $\alpha = 0.73$ and $\mathscr{O} = 0.93$ which indicates that the structures possess a net amount of orientation. These calculations show that these quantities are capable of detecting and quantifying any orientation in the structures on a sphere.

In the above example, we considered structures on a sphere which are aligned with each other. For this case, the value of α shows a broad range from 0.73 to 1 for different stereo-graphic projection plane. On the other hand, if the structures on a sphere are randomly oriented. Then the structures on different projection planes will also be randomly oriented. Hence α will be close to 1 for all these projection planes. In this way any alignment in the structures on a sphere can be detected.

Further, we study the elliptically shaped structures on a sphere, whose major axes are aligned towards the pole, which are located far away from the equator and those that are near the equator. We consider the structures that lie in the range of colatitude angle ($0^\circ - 70^\circ$ and $110^\circ - 180^\circ$) and those that lie in the range of colatitude angle ($70^\circ - 110^\circ$). The value of α for these two cases, and the percentage difference between them, for different projection planes are

Angle b/w equatorial plane and projection plane (δ)	α for structures in $0° \leq \theta \leq 70°$ and $110° \leq \theta \leq 180°$	α for structures in $70° \leq \theta \leq 110°$	% difference
0°	0.9963	1.0000	0.37%
45°	0.9322	0.9612	3.11%
90°	0.7259	0.8065	11.10%

Table 7.4: The table shows the value of α for a sphere containing elliptically shaped structures. The Column 2 shows α for the case where the structures fall in the range of colatitude angle $0° \leq \theta \leq 70°$ and $110° \leq \theta \leq 180°$ are considered, with different projection planes given in Column 1. The Column 3 shows the same but for the structures that lie in the range of colatitude angle $70° \leq \theta \leq 110°$. The percentage difference between these two cases are shown in Column 4.

shown in Table. 7.4 . The percentage difference shows that it is small when the structures have negligible orientation. While it increases as the structures becomes more and more aligned with each other. The reason for this error is: even though the given excursion set on the curved surface of a sphere have structures completely aligned with each other, the structures near the equator becomes randomly oriented when it is projected onto a plane. Hence, all the structures that fall in the range of $(70° - 110°)$ will be removed during the analysis of CMB fields.

7.4 Application to simulation of CMB fields with ΛCDM model

7.4.1 α and β for simulated CMB fields

The excursion set of a random field varies systematically with the threshold value. This will have an imprint on the boundaries of the structures in the excursion set. Therefore, the tensor, $W_2^{1,1}$ and hence α and β, will be able to capture this systematic behavior with the threshold value.

We compute α and β for simulated `CMB` temperature and E mode fields, with Gaussian and isotropic distribution. In order to analyze the intrinsic shape and orientation of structures in the excursion set of these fields. The `CMB` fields are used which are scaled by the `RMS` value. Threshold values lying in the range $-6 < \nu < 6$ with 20 bins are chosen. The value of α and β obtained will provide an estimate of their expected values for Gaussian and isotropic random fields.

In the present analysis, we use `CMB` fields with the cosmological parameters obtained from the `PLANCK` data [51]. We use temperature and E mode fields with scalar perturbations. The resolution corresponds to the maximum multipole $\ell_{\rm max} = 2200$ and $N_{\rm side} = 1024$. Gaussian smoothing removes small structures and hence the smoothing angle is chosen such that temperature and E mode field have similar number of structures. We choose the `FWHM`$= 20'$ for temperature, and $50'$ for E mode.

We compute $W_2^{1,1}$ using the algorithm described in the previous section. The projected plane is pixelized with $(3N_{\rm side})$ x $(3N_{\rm side})$ pixels. This was chosen so that the total number of pixels on the projected plane is larger than the total

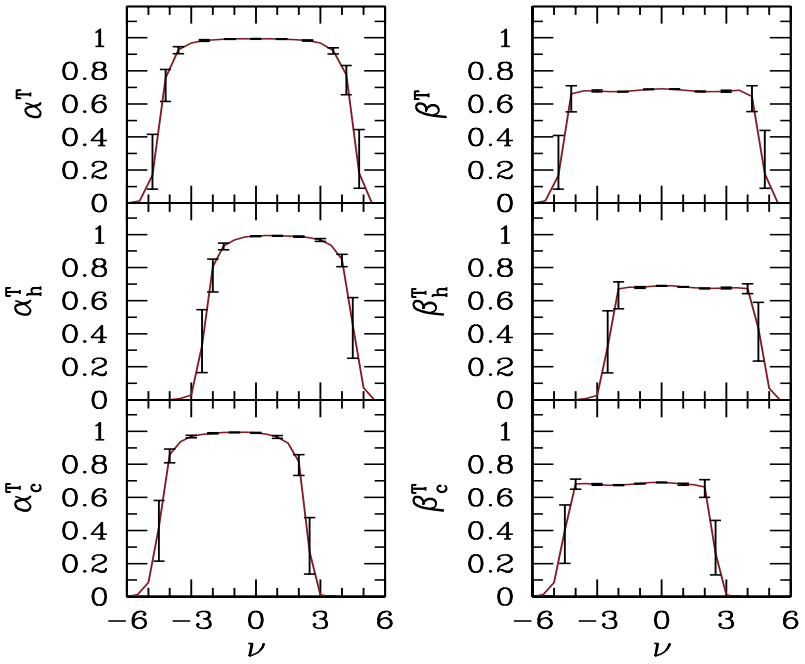

Figure 7.5: The top panels show α^T (left panel) and β^T (right panel) as a function of ν for both hot spots and cold spots of the temperature field (represented with the superscript T). The middle panels show the same for only hot spots (represented with the subscript h). The bottom panels show the same for only cold spots (represented with the subscript c). These are average over 100 simulations of `CMB`. The error bars are the corresponding sample variance.

number of pixels on the sphere. As described in the previous subsection, we remove the structures that fall on the colatitude angle from $\theta = 70^\circ$ to 110° in order to reduce the numerical error. In order to remove these structures, a map marking these pixels is first constructed and then it is stereo-graphically projected onto a plane. Then all of the structures in the excursion set that overlap with these marked pixels are completely removed.

The Fig. 7.5 shows the variation of α^T and β^T as a function of ν for temperature field. The zoomed in version is shown in Fig. 7.6. The top panels

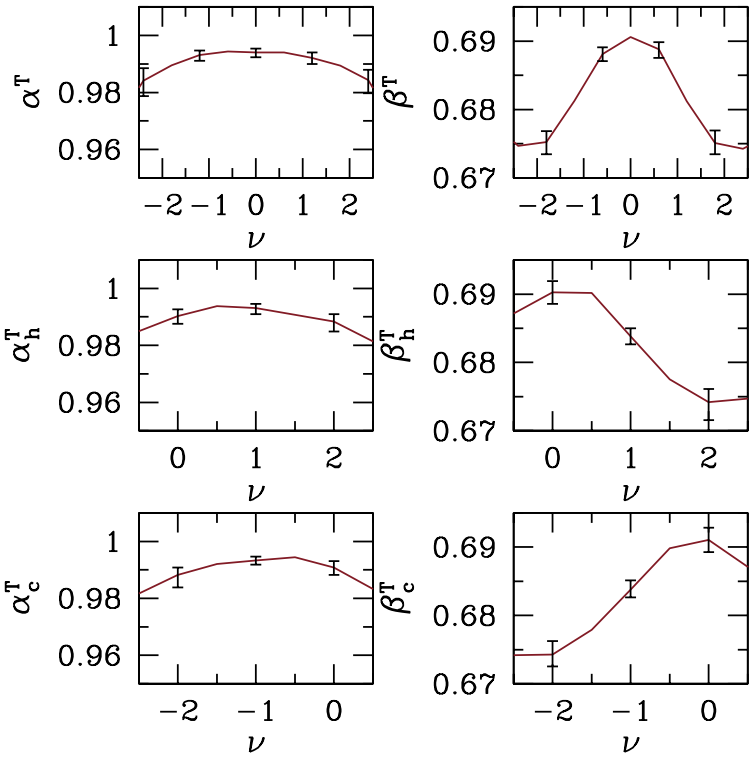

Figure 7.6: The figure is the same as the Fig. 7.5 but where the threshold range is enlarged.

show α^T (left panel) and β^T (right panel) computed using both the structures hot spots and cold spots. These are average over 100 maps and the error bars are the respective sample variance.

The α^T value is close to one when $|\nu| \approx 1$ with small error bars. This indicates that the structures in the CMB temperature maps has no net orientation. Initially we had assumed that the maps are statistically isotropic, hence the above result recovers this input assumption. In this calculation, the galactic plane is chosen as the stereo-graphic projection plane. In order to search for net orientation, the calculations should be repeated for different choices of projection planes whose necessity is described in Appendix. 7.3.2. The figure

shows that the variation of α^T with the threshold is symmetric about $\nu = 0$. At $|\nu| > 1$, the value of α^T is less than one with large error bars. This is because the number of structures at large ν values are very few. This in turn leads to small sample size resulting in net orientation which grows with $|\nu|$.

The Fig. 7.5 shows the variation of β^T as a function of ν and the enlarged version is shown in Fig. 7.6. The β^T vs ν has a characteristic shape. The figure shows that the structures in the temperature field possesses a net intrinsic anisotropy. The net anisotropy at different threshold values is about $\beta^T \simeq 0.68$. Error bars are small at $\nu \approx 1$ where the number of structures are large similar to that of α^T. A lot of sample maps does not contain any structures, hence when the β^T value is averaged over the sample maps it leads to a smaller value and large error bars. Further, the β^T value shows a sharper drop with ν than the α^T value at larger threshold values.

We compute α and β of temperature field for hot spots and cold spots separately. The Fig. 7.5 shows the plots of α (left panel) and β (right panel) for hot spots (with subscript h) in the middle panels. While the bottom panels shows the same for cold spots (with subscript c). The Fig. 7.6 shows the enlarged version of the plots. The plots show that they are symmetric around $\nu = 1$ for hot spots while for cold spots it is around $\nu = -1$. This shift in the center of the plot is because there are more hot spots at positive threshold values and there are more cold spots at negative threshold values. Further, the shapes are not symmetric around the center of the plots. We observe that the shape of α_h^T vs ν and α_c^T vs ν are mirror images of each other. Similarly, the shape of β_h^T and β_c^T are also symmetric. The net intrinsic anisotropy of both the structures, hot spots and cold spots, are equal.

The Fig. 7.7 shows the value of α and β of E mode field (with superscript

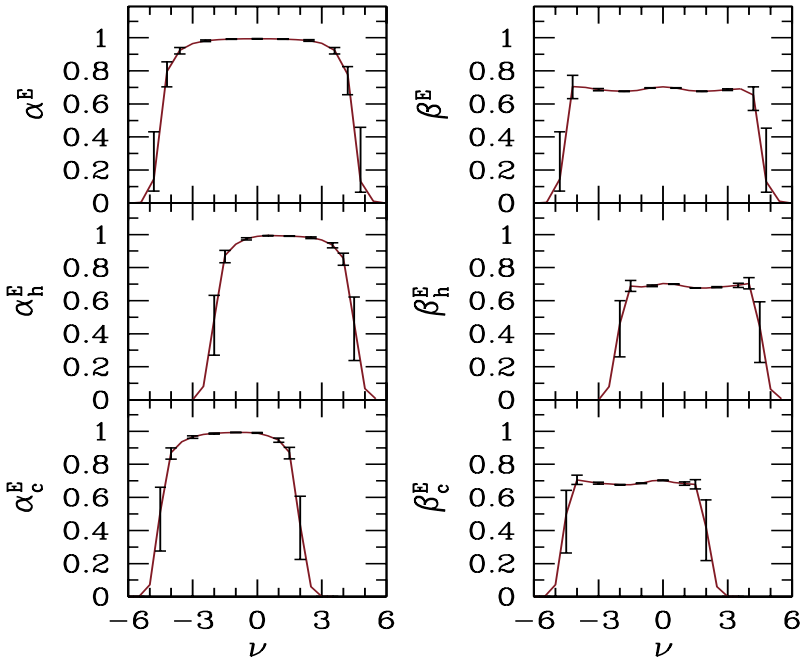

Figure 7.7: The figure is the same as the Fig. 7.5 but for E mode field.

E). The enlarged version of the plots are shown in Fig. 7.8. The net anisotropy of E mode field is close to 0.69 while for the temperature field it is close to 0.68. This implies that the structures in the temperature and E mode fields are slightly different which may have originated due to the different mechanism of evolution in these fields. Other than this point, the plots of E mode field shows similar behavior to that of the temperature field.

7.4.2 Numerical correction for α and β due to pixelization

The structures in the excursion set of `CMB` fields have continuous contour upto quantum level. But the values of α and β computed in the previous subsection

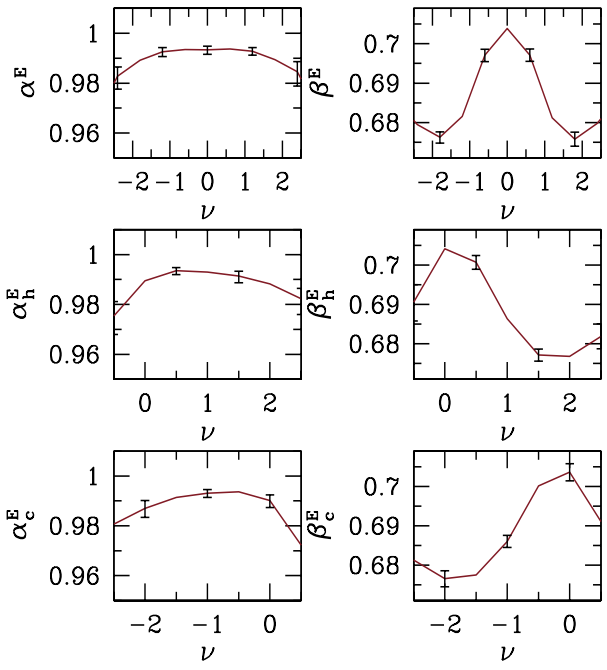

Figure 7.8: The figure is the same as the Fig. 7.7 but where the threshold range is enlarged.

was obtained with polygons on the pixelized space. In Sec. 7.2.2, it was shown that the numerical error in β due to pixelization increases as the aspect ratio of ellipse decreases. We correct for this numerical error by using the following points: structures in the CMB fields with very high curvature are rare and any curved section of the structure can be approximated with a section of an ellipse. Hence an approximate correction for β can be estimated by subtracting the numerical error in elliptic polygon for respective β values, i.e. $\beta = 0.68$ for temperature and 0.69 for E mode, by interpolating the values in Table. 7.1. Correcting for the β values we get $\beta = 0.62$ for temperature field and $\beta = 0.63$ for E mode field. These are the intrinsic anisotropy of structures in the CMB fields predicted by the standard ΛCDM cosmology. This originates from the anisotropy due to the primordial fluctuations and the subsequent evolution

during later epochs, such as the recombination and reionization eras.

In Sec. 7.2.3, it was shown that the numerical error in α due to pixelization is negligible for $\alpha \approx 1$. The value of α for simulated CMB fields was obtained to be one. Hence no correction is required for this case.

7.5 Discussion

We have introduced the TMFs as a new statistical tool for the analysis of CMB data. We have developed a code, referred as TMFCode, for computing α and β of a random field on a plane. The numerical errors in these quantities due to pixelization was analyzed. We found that the pixelization error in net anisotropy increases as the structures become more and more elongated. In the case of net orientation, the error is negligible when the structures are unoriented and it increases as the structures become more and more aligned with each other. Then we computed α and β for Gaussian and isotropic simulations of pure CMB. We found that the net anisotropy in hot spots and cold spots according to the standard ΛCDM model are: $\beta = 0.62$ for temperature and $\beta = 0.63$ for E mode, where the values are corrected for pixelization error. Further, the net orientation, α, for all the structures in the temperature and E mode was found to be one, which is as expected for a Gaussian and isotropic field.

In the earlier works [130, 131, 132], the shape of hot spots and cold spots of CMB maps was used for the analysis. They used ellipticity parameter, ϵ, to measure the anisotropy in the shape, which is defined as the ratio of the distance of farthest and closest point on the contour of the structure from its center. They obtained the value $\epsilon \sim 2.2$. Approximately, ϵ is related to β as $\epsilon \approx 1/\beta$. As the β parameter is capturing the overall shape using the entire

closed contour of a structure, hence the value of ϵ is larger than $1/\beta \sim 1.6$.

Chapter 8

Application of Tensor Minkowski Functionals to the analysis of PLANCK data

8.1 Introduction

In this chapter, we apply Tensor Minkowski Functionals for the analysis of CMB maps obtained by the PLANCK satellite. In the observational data, morphological features are generated due to the instrumental effects. Here, we study its effect on the value of α and β of the CMB maps. Then, we analyze and quantify the consistency of different PLANCK data sets with the theoretical expectation.

This chapter is organized as follows. A description of the PLANCK data is given in the second section. The effect due to the presence of CMB lensing and instrumental effects on α and β is studied in the third section. An analysis and estimate of the level of consistency between different PLANCK data sets and

the prediction from the standard model of cosmology is also presented. These results are summarized and its implications are discussed in the final section.

8.2 PLANCK data

The PLANCK satellite has provided us with the temperature, Q, and U maps. It carried two instruments, namely, L*ow* F*requency* I*nstrument* (LFI) and H*igh* F*requency* I*nstrument* (HFI). The LFI operates in 3 frequency bands, namely, 30GHz, 44GHz, and 70GHz. While the HFI operates in 5 frequency bands, namely, 100GHz, 143GHz, 217GHz, 353GHz, 545GHz, and 857GHz. The temperature was mapped in all the 9 frequency bands while the polarization in the first 7 frequency bands mentioned above.

The PLANCK data release includes 8^{th} generation F*ull* F*ocal* P*lane* simulations, namely, FFP8, for each frequency[1] [128]. These simulations are generated in six different components, namely, lensed scalar perturbation, tensor perturbation, non-Gaussian perturbation, two foreground components with and without bandpass filter, and noise. These components are simulated for each detector, which includes instrumental, scanning and analysis effects. Then a realization of CMB map can be constructed by adding all these components with the weightage of $\sqrt{r}$ for tensor component and f_{NL} for non-Gaussian component. For the subsequent analysis, we only use lensed CMB component with scalar perturbation and the noise component. For masking these simulation maps, we use preferred mask that is provided in the PLANCK data, namely UT78, for temperature and UPB77 for polarization. Both of these have a sky fraction

[1] http://pla.esac.esa.int/pla/

of about 77%.

The CMB maps are produced using the observational map from different frequency channels using the following foreground separation methods: COMMANDER, NILC, SEVEM, and SMICA, which are provided in the PLANCK data [129]. COMMANDER is a PLANCK software code which is implemented in pixel space. The different foreground components like synchrotron, free-free and spinning dust are modeled with a few parameters per pixel. These parameters include the amplitude at the given frequency, a few spectral parameters and instrumental parameters. These are then fitted with the data and the CMB maps are obtained. In NILC or N*eedlet*-ILC, the CMB maps are constructed from frequency maps using internal linear combination in needlet space, where needlet is a construction which is intrinsically spherical but localized in pixel space. These combination weights depends on the frequency, and varies over the sky and with the multipole. The SMICA also uses linear combination of frequency channel maps with weights, which are frequency and multipole dependent. But this uses different parametrizations from the NILC. The SEVEM technique generates clean CMB map at different frequencies by fitting templates. These templates are constructed with the lowest and highest frequency channels, where the foreground component dominates. These are then subtracted from the frequency channels which is dominated by CMB signal to get the clean CMB maps. Each of these data set are further split into five maps, namely, full mission, half mission 1, half mission 2, half ring 1 and half ring 2. The full mission is constructed using the data from full PLANCK mission. In order to construct other maps, the CMB maps are divided into rings of constant latitude. In the case of HFI, these rings are divided into two distinct sets each containing half of the rings, using which the

two half mission maps are constructed. For LFI, half mission 1 map is generated using data from first half of the mission while the half mission 2 map uses the data from the rest of the mission. Half ring 1 and 2 maps are constructed using the first half and second half of each of the rings respectively. In total, there are 20 different maps. Further, note that these polarization maps contain systematics at large angular scales. Hence all the simulation and observational polarization maps are high pass filtered, which means that all the multipoles with $\ell < 30$ are removed.

For masking the Galactic and point sources in the foreground separated maps, confidence masks provided for each of them are used. The mask for temperature map has a sky fraction ranging from 81.9% to 96.4%. While the mask for polarization map ranges from 79.4% to 96.5%. We will also use the preferred masks for consistency check. But we remove the structures that lie within $\pm 20^{\circ}$ from the equator from the CMB maps during the analysis, which corresponds to a sky fraction of about 77%, hence the choice of mask will not have any big impact on the results.

8.3 α and β for masked CMB fields

Since the values of α and β for a CMB map are computed on the pixel space, it is straight forward to calculate these quantities for a masked CMB map. Here, we describe the procedure for the process of smoothing, masking and projecting onto a plane that we follow in order to obtain the final planar CMB map.

The pixels of a given mask map will have the value of either 0, which are masked pixels, or 1, which are trustworthy or uncontaminated pixels. The CMB map is smoothed with appropriate smoothing angle. The mask map is

separately smoothed with the same smoothing angle as the CMB map. Due to smoothing, the uncontaminated pixels close to the contaminated pixels in the mask map also gets contaminated. Hence these new contaminated pixels also needs to be removed. The mask map now will have values ranging from 0 to 1. A cut off value is chosen from this range of values which indicates the extent to which we stay away from the originally contaminated pixels in the mask map. The pixels in the mask map which have value below the cut off value are all masked i.e. its value is set as 0 and otherwise set as 1. Now the CMB map and mask map are projected onto a plane using stereo-graphic projection. Finally, the structures in the projected CMB map are removed, which have one or more pixels in common with the masked pixels in the projected mask map.

8.4 Effect of lensing and systematics of instrument on α and β

Here, we study the impact of lensing and instrumental effects such as beam and noise on the value of α and β. We use the FFP8 simulations of lensed CMB and noise maps of frequencies 44GHz and 70GHz. The values of α and β are obtained by averaging over 100 simulations of [lensed CMB + noise] map. This is then compared with the value obtained from the pure simulations of Gaussian and isotropic CMB maps in Sec. 7.4 (here the maps are masked and the E mode map is high pass filtered).

The percentage difference in the value of α and β due to the presence of CMB lensing and instrumental effects is less than 2%. The effect of CMB lensing and instrumental beam is to change the shape of the structures, which then

	Temperature field				E mode field			
	Hot spots		Cold spots		Hot spots		Cold spots	
	σ_α	σ_β	σ_α	σ_β	σ_α	σ_β	σ_α	σ_β
44GHz	+82.9%	+46.4%	+84.9%	+12.1%	+47.9%	−7.7%	+38.5%	+0.0%
70GHz	+65.9%	+33.9%	+64.0%	+25.9%	+43.7%	+5.8%	+34.6%	+10.9%

Table 8.1: The table shows the percentage difference in σ_α and σ_β due to the CMB lensing and instrumental effects.

broadens the range of shapes in the distribution of structures. This increases the size of the error bars, which are σ_α and σ_β, although the mean value may not be significantly affected. While the effect of noise is to increase the number of structures, which in turn results in a decrease of σ_α and σ_β. The error bar of [lensed CMB + noise] map is due to the combination of these two effects. The Table. 8.1 shows the percentage difference in σ_α and σ_β calculated at $|\nu| = 1$. We observe from the table that it is getting affected significantly. Overall, the calculation of percentage difference at different threshold values, $|\nu| = 0, 1, 2$, shows that the error bars increase due to the presence of CMB lensing and instrumental effects. Further, σ_α and σ_β of 44GHz at different threshold values are larger than that of 70GHz.

In the subsequent subsections, we use $\alpha, \beta, \sigma_\alpha$ and σ_β corresponding to the frequency band of 44GHz for the computation of deviations, defined in Eq. (8.1), for the PLANCK data sets from the theoretical prediction. This will give a more conservative estimate of the deviation in comparison to that of 70GHz.

8.5 Application to PLANCK data

The plots showing α and β vs ν for the temperature field of full mission SMICA map are shown in Fig. 8.1. It is shown for all the structures (top panels), hot spots (middle panels), and cold spots (bottom panels). The enlarged version of these plots are shown in Fig. 8.2. The Figs. 8.3 and 8.4 show the same but for the E mode field. Similar to the Sec. 7.4, we use the superscript T and E to denote temperature and E mode field respectively. While the subscript h and c refers to hot spots and cold spots respectively and those without the subscript indicates that all the structures are being considered.

In the following subsections, we quantify the deviation in the value of α and β of PLANCK data from the standard ΛCDM prediction. In order to make this comparison, we need simulations of CMB map which includes the features due to the PLANCK instruments. Then the values of α and β can be computed from these maps. The PLANCK data includes FFP8 simulations of each frequency band as described in Sec. 7.4. But the co-addition of the frequency maps requires weights which has not been provided. Further the comparison using each of the frequency bands without co addition is computationally costly and hence it is not a practical option. Hence, we use the frequency bands of 44GHz and 70GHz. These frequency maps have lower signal to noise ratio than that of other frequencies. The signal to noise ratio of temperature map is about 2.2 for 44GHz and 2.8 for 77GHz. While for E mode map it is about 0.03 for 44GHz and 0.07 for 77GHz.

In the subsequent analysis, the threshold values of $\nu = 0, 1, 2$ for hot spots and $\nu = 0, -1, -2$ for cold spots will be chosen. This corresponds to the threshold levels where the excursion set contains large number of structures.

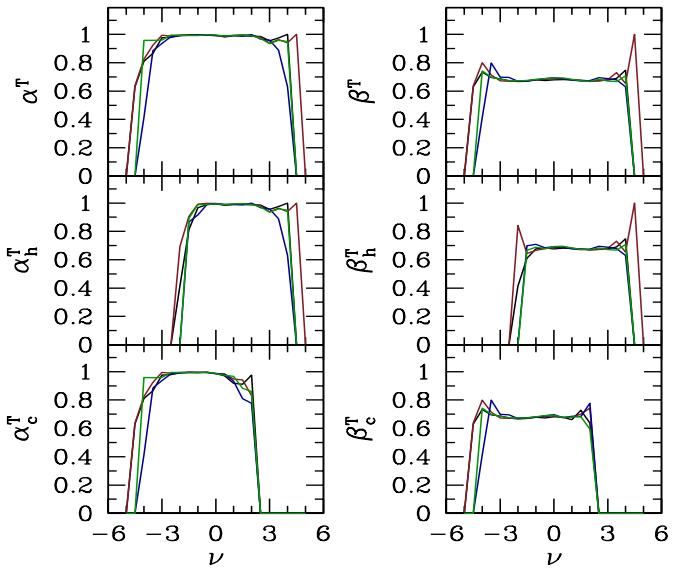

Figure 8.1: The top panels show α and β vs ν computed for all the structures of temperature field of PLANCK full mission map. The plots is shown for maps obtained form different foreground separation method, namely, SMICA (black line), COMMANDER (dark red line), NILC (blue line) and SEVEM (green line). The middle panels show the same as top panels but for the hot spots of temperature field. The bottom panels show the same as top panels but for the cold spots of temperature field.

The temperature field is smoothed with the FWHM of $20'$ and $50'$ for E mode field. This corresponds to about 3500 structures at $|\nu| = 1$ and 1000 structures at $|\nu| = 0, 2$. The extent of deviation in the PLANCK data from the theoretical expectations in the units of $1-\sigma$ error bar is defined using the quantity $\mathscr{D}$ as

$$\mathscr{D}_X = \left| \frac{X^{\rm obs} - \overline{X}^{\rm sim}}{\sigma_X} \right|, \tag{8.1}$$

with $X = \alpha, \beta$. Here the superscripts obs and sim indicates that the X is obtained from the observational data and simulated PLANCK data respectively,

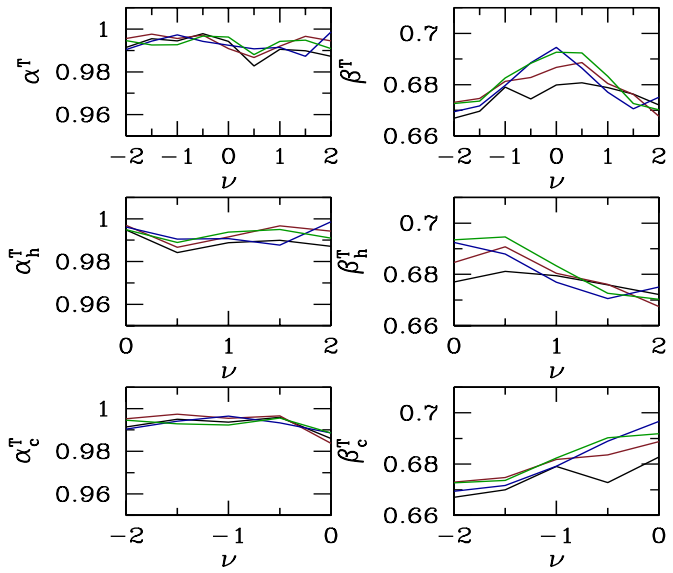

Figure 8.2: The figure is the same as Fig. 8.1 but enlarged in the range $0 \leq \nu \leq 2$ for hot spots and $-2 \geq \nu \geq 0$ for cold spots.

and the σ_X is the average of the upper and lower bounds of the $1-\sigma$ error bar.

8.5.1 Net anisotropy for structures of the PLANCK data

The value of β for temperature and E mode maps corresponding to all the PLANCK data sets is about 0.68. Similar to the case of simulated CMB maps in Sec. 7.4.2, here also we correct the β value for the pixelization error. Then we get $\beta \sim 0.62$.

The deviation, $\mathscr{D}_\beta$, of temperature and E mode maps for each of the PLANCK data sets, for hot spots and cold spots at $\nu = 0$ (top line), $|\nu| = 1$ (middle line), and $|\nu| = 2$ (bottom line), are shown in the Tables. 8.2 and 8.3. In order to do a simple comparison of $\mathscr{D}_\beta$ between different PLANCK data sets, we average

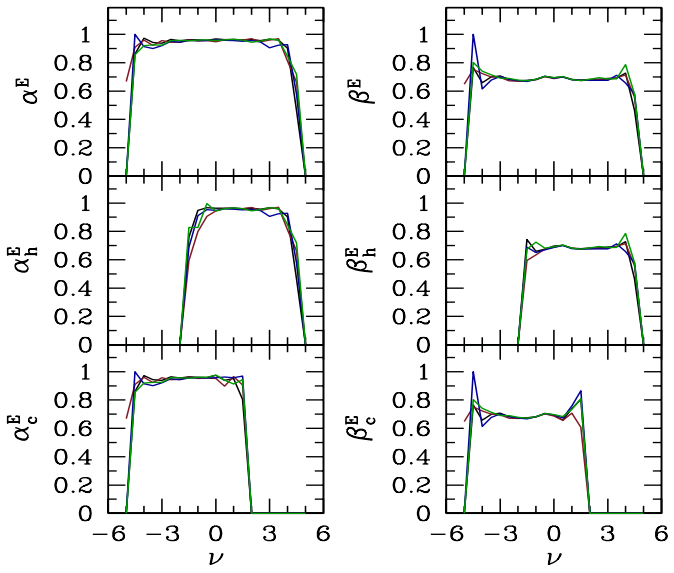

Figure 8.3: The figure is the same as Fig. 8.1 but for E mode field of PLANCK full mission maps.

$\mathscr{D}_\beta$ obtained for hot spots and cold spots corresponding to the threshold values $|\nu| = 0, 1, 2$ (average over six deviation values), for each of the PLANCK data sets. The average $\mathscr{D}_\beta$ of temperature and E mode maps for different PLANCK data sets are given in the Tables. 8.4. The temperature and E mode maps corresponding to all the data sets are consistent with the theoretical predictions within $2-\sigma$, except the NILC half mission 2 data which shows a slightly higher deviation of $2.1-\sigma$.

In the above shown computations of β, uncertainties originate due to the following main sources:

- The uncertainties arising from statistical fluctuations is about 0.4%. This is computed using the simulations of 44GHz described in the Sec. 7.4. This error is used to quantify the extent of agreement between PLANCK

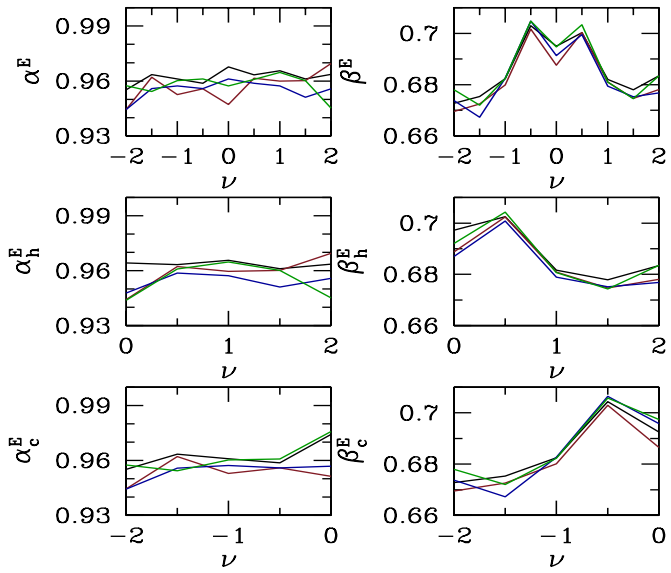

Figure 8.4: The figure is the same as Fig. 8.3 but enlarged in the range $0 \leq \nu \leq 2$ for hot spots and $-2 \geq \nu \geq 0$ for cold spots.

data and simulation, $\mathscr{D}_\beta$, shown in Table. 8.4.

- The numerical error due to pixelization for the β value of 0.68 is about 9.8%. As described in Sec. 7.2.2, this error depends on the value of β. The β value for both simulation and `PLANCK` data is about 0.68. Hence the pixelization errors for both the data are same and so cancels each other out.

The percentage deviation of D_β for both temperature and E mode map corresponding to all the `PLANCK` data sets is about 0.5%.

In the above results, the confidence masks corresponding to `SMICA`, `COMMANDER`, `SEVEM`, and `NILC` were used. The calculations were repeated using the preferred mask. The value of $\mathscr{D}_\beta$ marginally increases in some data sets while it decreases in others. But the main results remain the same. This is because we do an

D_β^T	Full mission	Half mission 1	Half mission 2	Half ring 1	Half ring 2
	0.25, 0.73	0.32, 1.41	1.08, 1.00	0.53, 1.02	0.73, 0.35
SMICA	0.45, 0.63	0.90, 0.40	0.32, 0.70	0.17, 0.17	0.57, 0.30
	0.89, 2.56	0.68,1.61	0.76, 0.44	0.79, 0.28	0.13, 2.31
	1.19, 1.92	0.92, 1.63	1.81, 2.18	0.98, 1.63	0.98, 1.78
COMMANDER	0.67, 1.53	0.02, 1.13	0.10, 1.03	0.00, 1.33	0.02, 1.10
	1.66, 1.08	1.14, 2.59	1.06, 0.23	1.58, 1.41	1.66, 0.67
	2.64, 3.45	1.96, 3.31	2.55, 2.75	2.43, 2.71	2.42, 2.90
SEVEM	0.20, 0.67	0.77, 0.63	0.57, 1.53	0.42, 0.40	0.30, 0.83
	0.44, 1.97	0.24, 1.72	0.45, 0.69	0.13, 0.36	0.63, 1.41
	2.83, 2.53	2.49, 2.84	2.42, 3.06	1.79, 3.12	2.49, 2.86
NILC	1.42, 1.73	1.25, 1.77	2.05, 1.73	1.92, 2.57	0.92, 1.87
	1.19, 1.13	0.97, 0.51	1.31, 1.95	0.44, 1.92	0.76, 0.15

Table 8.2: The table shows the deviation, D_β, of hot spots and cold spots for temperature corresponding to the different PLANCK data sets. In each of the data set, the top line gives the value for the hot spots and cold spots at $\nu = 0$, middle line for $|\nu| = 1$ and bottom line for $|\nu| = 2$.

angular cut of $\pm 20^\circ$ from the equator as mentioned in Sec. 7.4. Further, the numerical computations shown in Table. 8.4 were obtained using the Galactic plane as the stereo-graphic projection plane. Nevertheless, the calculations were repeated for different projection planes and we obtained similar results.

D_β^E	Full mission	Half mission 1	Half mission 2	Half ring 1	Half ring 2
	0.18, 0.79	0.80, 0.02	0.27, 0.22	0.13, 1.29	0.53, 1.76
SMICA	2.61, 3.18	3.13, 3.64	1.22, 2.27	1.96, 2.91	3.09, 1.36
	2.59, 0.55	0.59, 0.14	2.46, 0.44	0.22, 1.25	0.19, 0.30
	1.71, 1.83	0.07, 0.17	1.20, 0.57	0.71, 0.43	0.53, 0.48
COMMANDER	2.26, 2.09	2.56, 0.77	1.87, 0.91	3.00, 2.64	1.30, 0.50
	1.16, 1.47	1.14, 0.03	0.46, 1.08	1.08, 1.44	0.54, 0.80
	2.04, 0.22	2.09, 1.15	0.24, 0.45	2.51, 0.15	0.93, 0.62
SEVEM	1.43, 3.27	1.43, 1.73	2.04, 3.68	1.13, 2.32	2.17, 1.54
	0.81, 0.30	0.05, 0.19	0.73, 1.30	0.62, 0.44	0.38, 0.44
	1.11, 0.05	0.38, 1.02	2.51, 1.26	0.14, 0.93	0.51, 0.29
NILC	2.17, 3.09	1.52, 2.82	0.56, 1.59	1.13, 1.32	2.96, 1.50
	2.62, 0.89	2.08, 0.05	2.89, 2.94	0.92, 1.58	0.27, 1.72

Table 8.3: The table is same as Table. 8.2 but for E mode map.

Average $\mathscr{D}_\beta^T$	Full mission	Half mission 1	Half mission 2	Half ring 1	Half ring 2
SMICA	0.92	0.89	0.72	0.49	0.73
COMMANDER	1.34	1.24	1.07	1.15	1.04
SEVEM	1.56	1.44	1.42	1.07	1.41
NILC	1.81	1.64	2.08	1.96	1.51

Average $\mathscr{D}_\beta^E$	Full mission	Half mission 1	Half mission 2	Half ring 1	Half ring 2
SMICA	1.65	1.39	1.15	1.29	1.20
COMMANDER	1.75	0.79	1.01	1.55	0.69
SEVEM	1.35	1.11	1.41	1.20	1.01
NILC	1.66	1.31	1.96	1.00	1.21

Table 8.4: The tables show the deviation, $\mathscr{D}_\beta$, which is the average of six values obtained for hot spots and cold spots corresponding to the threshold levels $|\nu| = 0, 1, 2$, for temperature (denoted with superscript T) and E mode (denoted with superscript E) maps.

8.5.2 Net orientation for structures of the PLANCK data

The deviation, $\mathscr{D}_\alpha$, of temperature and E mode map for different PLANCK data sets are given in the Tables. 8.5 and 8.6. Similar to the previous subsection, the average $\mathscr{D}_\alpha$ are estimated for temperature and E mode map corresponding to each PLANCK data set which are shown in the Tables. 8.7. We observe that the temperature map of all the PLANCK data sets are in good agreement with the theoretical predictions to within $1.23 - \sigma$.

From the Table. 8.7, we observe that the E mode map of all the data sets show deviations higher than $3 - \sigma$, except the SMICA full mission map which is about $2.29 - \sigma$. The half mission 1 map corresponding to all the foreground separation methods shows slightly higher deviation of $5 - \sigma$. This indicates that the structures in these E mode maps possesses a significant level of alignment.

The above results were obtained using the Galactic plane as the stereographic projection plane. In order to detect the presence of any alignment in the structures which lie on a sphere, the analysis should be done for different stereo-graphic projection planes (described in Subsection. 7.3.2). Hence the above calculations was repeated for SMICA full mission map with different stereo-graphic projection planes and overall they show higher deviations. The possible origin of this alignment are: cosmological source, instrumental characteristics of the frequency channel. The latter reason being more likely because we are comparing the CMB observational map obtained by co-adding all the frequency bands with the simulated map of the specific frequency band of 44GHz. Further, as mentioned earlier that the signal to noise ratio of E mode map of 44GHz is very low and hence it is dominated by noise.

D_α^T	Full mission	Half mission 1	Half mission 2	Half ring 1	Half ring 2
	1.51, 0.49	0.77, 0.34	1.07, 0.92	1.34, 0.44	1.11, 0.26
SMICA	0.45, 1.13	0.50, 1.22	0.90, 0.87	0.67, 1.11	0.59, 0.98
	0.67, 1.11	0.67, 0.78	0.94, 1.53	0.74, 1.50	0.65, 1.18
	1.76, 0.21	1.83, 1.21	1.44, 0.00	1.62, 0.05	1.44, 0.48
COMMANDER	0.79, 1.36	0.29, 1.17	0.49, 1.54	0.65, 1.37	1.09, 1.42
	1.31, 1.44	1.16, 1.37	1.31, 1.65	1.33, 1.28	1.34, 1.23
	1.67, 0.80	1.48, 0.65	1.27, 0.69	1.51, 0.95	1.55, 0.83
SEVEM	0.70, 1.48	0.45, 1.60	0.90, 1.53	0.64, 1.39	0.72, 1.44
	1.71, 1.03	1.38, 1.02	1.44, 0.86	1.70, 0.75	1.55, 1.26
	1.51, 0.80	1.08, 0.82	1.63, 0.40	1.61, 0.00	1.39, 1.00
NILC	1.07, 0.98	0.86, 1.13	0.91, 0.96	0.89, 1.20	0.91, 0.94
	1.02, 1.39	1.23, 1.32	0.71, 0.58	0.76, 1.28	0.70, 1.01

Table 8.5: The table shows the deviation, D_α, of hot spots and cold spots for temperature corresponding to the different PLANCK data sets. In each of the data set, the top line gives the value for the hot spots and cold spots at $\nu = 0$, middle line for $|\nu| = 1$ and bottom line for $|\nu| = 2$.

There are mainly two sources of uncertainties in the calculations of α. These sources are listed below:

- The error due to the statistical fluctuations, which is calculated from the simulations of 44GHz described in Sec. 7.4, is about 0.7%. The extent of consistency between simulation and data, $\mathscr{D}_\alpha$, is quantified using this error, shown in Table. 8.7.

D_α^E	Full mission	Half mission 1	Half mission 2	Half ring 1	Half ring 2
	1.63, 0.40	2.60, 3.23	0.90, 2.30	2.83, 2.46	2.82, 1.63
SMICA	2.82, 3.91	7.41, 4.48	4.00, 5.50	3.49, 6.06	4.47, 4.85
	1.99, 2.99	5.58, 2.77	3.23, 3.47	2.90, 3.84	3.82, 2.89
	4.05, 3.02	3.84, 4.43	3.04, 3.01	0.88, 3.49	2.53, 1.45
COMMANDER	4.04, 5.67	7.41, 5.15	3.53, 6.04	3.76, 6.96	4.45, 3.17
	1.24, 4.43	4.42, 4.80	2.32, 4.80	3.20, 3.80	3.66, 3.64
	3.61, 2.38	4.87, 2.30	1.79, 2.39	1.79, 3.71	2.12, 5.55
SEVEM	4.53, 4.74	9.82, 6.72	5.02, 5.83	7.12, 8.22	5.80, 4.67
	2.97, 4.45	5.38, 2.73	2.53, 2.88	3.49, 4.76	4.63, 3.70
	4.08, 0.22	2.95, 5.40	0.42, 2.48	3.17, 2.70	2.94, 3.54
NILC	3.00, 4.09	7.00, 4.96	3.94, 6.52	3.18, 6.09	4.69, 4.78
	4.32, 2.68	5.38, 2.08	3.76, 2.51	2.61, 3.39	2.86, 2.92

Table 8.6: The table is same as Table. 8.5 but for E mode map.

Average $\mathscr{D}_\alpha^T$	Full mission	Half mission 1	Half mission 2	Half ring 1	Half ring 2
SMICA	0.89	0.72	1.04	0.97	0.79
COMMANDER	1.14	1.17	1.07	1.05	1.17
SEVEM	1.23	1.10	1.12	1.16	1.23
NILC	1.13	1.07	0.87	0.96	0.99

Average $\mathscr{D}_\alpha^E$	Full mission	Half mission 1	Half mission 2	Half ring 1	Half ring 2
SMICA	2.29	4.34	3.23	3.60	3.41
COMMANDER	3.74	5.01	3.79	3.68	3.15
SEVEM	3.78	5.30	3.41	4.85	4.41
NILC	3.06	4.63	3.27	3.52	3.62

Table 8.7: The tables show the deviation, $\mathscr{D}_\alpha$, which is the average of six values obtained for hot spots and cold spots corresponding to the threshold levels $|\nu| = 0, 1, 2$, for temperature (denoted with superscript T) and E mode (denoted with superscript E) maps.

- In Sec. 7.2.3, we showed that pixelization results in error in the calculation of α and the error depends on the value of α. Since the average α obtained from the 44GHz simulations is not the same as that of PLANCK data sets, the pixelization error in these two cases are also different. These errors can be computed by interpolating the values in Table. 7.1. The percentage deviation for $\mathscr{D}_\alpha$ of temperature map is about 0.8%, while for E mode map it is about -3%. When the simulation and observational data are corrected for pixelization error, the percentage deviation of $\mathscr{D}_\alpha$ for temperature becomes 2%, while it becomes -7% for E mode. This indicates that the statistical significance of the net alignment detected in the E mode data increases when the pixelization error is taken into account.

The results shown above were obtained using confidence masks provided for each of foreground separation methods, namely, SMICA, COMMANDER, SEVEM, and NILC. We repeated these calculations with the preferred mask. We find that the deviation, $\mathscr{D}_\alpha$, slightly increases for some data sets while it decreases for others. However, the overall results remain the same. This is as expected since the structures that fall within $\pm 20^\circ$ from the equator are removed as mentioned in Sec. 7.4.

8.6 Discussion

We applied the Tensor Minkowski Functionals for the analysis of PLANCK data. We analyzed the affect of lensing and instrumental systematics on the values of α and β using the simulations of the frequency channel 44GHz and 70GHz included in the PLANCK data. We found that the percentage difference in α and

β due to these effects is less than 2% while their size of error bars significantly increases. Then we tested the consistency of various PLANCK data sets. For this testing, we used the simulations of the frequency channel, namely 44GHz, as the basis and the observational data from different foreground separation methods. These two were then used to estimate the deviation in α and β of observational data from the theoretical prediction. We found the net anisotropy corresponding to all the data sets of temperature and E mode are in good agreement with the theoretical expectations within $2-\sigma$, except temperature map of NILC half mission 2 which showed a slightly larger deviation. The net orientation of temperature map of all data sets was found to agree with the standard model within $1.2-\sigma$. While the E mode maps was found to have deviations higher than $3-\sigma$ for all data sets except the SMICA full mission map. Further, the half mission 1 was found to have consistently higher deviations of about $5-\sigma$. These calculations indicate that the structures in the E mode of PLANCK data sets possesses some alignment. It is very likely that this alignment is caused because we are comparing the simulation of particular frequency 44GHz with the PLANCK data sets obtained by co-adding all the frequency channels, and further due to the low signal to noise ratio of E mode map of 44GHz, which implies that it is dominated by noise.

Chapter 9

Conclusion

9.1 Summary of the results and conclusions from the investigations

Our focus in this thesis was the investigation of the features in the CMB polarization, that were induced due to the primordial fluctuations and the statistical tools. This investigation was conducted along three different lines of thought process. The results and conclusions from each of these investigation are described in the following paragraphs.

In the first part, we studied the local type non-Gaussian features of primordial origin in the CMB polarization fields. We used the PDF of the fields as the statistical observable for this analysis. We obtained the analytic expression for the PDF of a general local type non-Gaussian field, which describes the PDF of CMB fields, namely temperature and E mode. The PDF of polarization intensity field which is constructed from local type non-Gaussian Stokes parameters field, Q/U, was also analytically obtained. From these analytic expressions, we

found that the non-Gaussian deviation for temperature and E mode is of the order $(f_{\rm NL}\sigma)$, while for the polarization intensity it is $(f_{\rm NL}\sigma)^2$. The numerical calculations of non-Gaussian deviation in the E mode field showed that its shape, amplitude and size of error bars are similar to that of the temperature. For the polarization intensity, the non-Gaussian deviation has an amplitude which is about an order of magnitude lower than that of temperature with error bars which are two times larger. Further, the shape of this deviation is distinct from the temperature. These analysis implies that from the theoretical point of view, the E mode field is capable of providing independent constraint on $f_{\rm NL}$ similar to the temperature field. While the polarization intensity field is not capable of providing an independent constraint. But in the realistic situation the statistical significance of these findings will decrease as the observational data contains instrumental systematics.

Then we analyzed the local type non-Gaussian features of polarization fields using the geometrical and topological properties, namely `SMF`s and Betti numbers. The non-Gaussian deviation calculated using these observables also showed the shape, amplitude and size of error bars similar to that of temperature. We found that the non-Gaussian deviation corresponding to the polarization intensity has an amplitude much smaller in comparison to the temperature at lower smoothing angles. While at higher smoothing angles, this amplitude becomes comparable to that of temperature. The shape of its non-Gaussian deviation has different shape in comparison to temperature. But the error bars are very large. These theoretical analysis, similar to the results from the `PDF` analysis, also suggests that the E mode field can give an independent constraint on $f_{\rm NL}$ while the polarization intensity field cannot give an independent constraint. Here also the instrumental systematics in the observational data

will decrease statistical significance of these results.

For the second part, we addressed the theoretical aspects related to the usage of the Stokes parameters Q/U of CMB as a complementary analysis of CMB. We analytically proved that the SMFs of Gaussian Q/U fields are invariant under rotation transformation about the line of sight. This holds only for the full sky coverage and hence it breaks down when the observational data is considered, where the Galactic and point sources needs to be masked leading to the incomplete sky. We studied the local type non-Gaussian features in the Stokes parameters field. We found that the non-Gaussian deviation in the SMFs of Q/U is about an order of magnitude lower than that of temperature. Additionally, their shape is distinct from that of temperature. Then we analyzed the effect on the SMFs of Q, U and I_P, and the number density of singularities in I_P due to the presence of primordial tensor perturbations. We found that all these quantities are sensitive to the presence of primordial tensor perturbations and their amplitudes decrease with the tensor-to-scalar ratio. This finding can be useful in the future experiments for the analysis and the searches of B mode in the polarization data. But the statistical significance of these results will reduce when the observational effects are included.

These kind of studies has become important as the observational polarization data has started to become more and more accurate. The sensitivity of the present CMB experiments is not good enough to detect the primordial non-Gaussianity. We can expect that the future experiments will be capable of detecting it. Since the presence of primordial local type non-Gaussianity results in different morphological features in Q/U and I_P from that of temperature and E mode. Hence all these fields can be used together for the analysis of non-Gaussianity in the observational data and they will be useful

in distinguishing between different sources of local type non-Gaussianity.

As the final part, we introduced TMFs, particularly $W_2^{1,1}$, as new statistical observable for the analysis of CMB data. This quantifies new morphological characteristics of a given field, which are the net anisotropy, β, and the net orientation, α, of the structures in the field. We a developed a code, referred as TMFCode, for numerical computation of α and β for a 2-dimensional field on an Euclidean plane. We analyzed the numerical errors in α and β due to the pixelization of the planar data by using the analytic formula of $W_2^{1,1}$ for an elliptical shaped structure. We found that the error in the net anisotropy increases with the increasing curvature of the boundaries of the structure. In the case of net orientation, the error is negligible for a given distribution of structures which are completely unoriented with other. But as the structures become more and more oriented with each other, the error increases and eventually becomes equal to the error in net anisotropy. Then we applied the TMFCode for computing α and β of CMB fields, where we used stereo-graphic projection to map the field values on a sphere onto a plane. We obtained the theoretical prediction for the values of α and β for simulated Gaussian and isotropic CMB fields according the standard model of cosmology. We found the net anisotropy of hot spots and cold spots to be $\beta = 0.62$ for temperature and 0.63 for E mode, where the values are corrected for the numerical errors due to pixelization. We found the net orientation for both temperature and E mode to be one, which means that there is no net orientation among the structures in the fields. These are the values expected for any general Gaussian and isotropic field.

Then we applied $W_2^{1,1}$ for the analysis of PLANCK data. We studied the effect of gravitational lensing and instrumental systematics on the value of α

and β by using the simulations corresponding to the frequency channels 44GHz and 70GHz containing the gravitational lensing and instrumental effects which are provided in the PLANCK data. These frequency channels have low signal to noise ratio compared to others. We found that the percentage difference in the value of α and β due to the presence of gravitational lensing and instrumental effects is less than 2% but the size of error bars increases significantly. We used the simulations corresponding to the 44GHz frequency channel as the basis for testing the consistency the simulations with the observational data. This will give a conservative estimate of deviations in the value of α and β of PLANCK data from ΛCDM prediction. Then we estimated the deviation α and β for the various PLANCK data sets foreground cleaned CMB maps namely SMICA, COMMANDER, SEVEM and NILC corresponding to full mission, half mission 1, half mission 2, half ring 1 and half ring 2. We found that the value of β is consistent with the standard model within $2-\sigma$ for different PLANCK data sets of temperature and E mode, except the temperature map of NILC half mission 2 which showed slightly higher deviation. For the case of α for temperature map of all the different data sets, we found good agreement with standard model within $1.2-\sigma$. While for the case of α for E mode map, the deviation in all data sets are higher than $3-\sigma$ except the SMICA full mission data. Further, the value of α for E mode map corresponding to the half mission 1 of all data sets showed consistently higher deviation of $5-\sigma$. These calculations indicates that the PLANCK's E mode data has certain level of alignment in its structures. The possible origin of this alignment are: cosmic origin or instrumental systematics. Here, the later reason is more probable as we are comparing the simulations with the instrumental characteristics of a specific frequency channel, namely 44GHz, with that of the PLANCK maps which are obtained by co-adding all

frequency channels. Further, as the signal to noise ratio of E mode map is low for the 44GHz frequency channel, it is mostly dominated by noise.

9.2 Future course of investigation

The investigation conducted so far opens up several lines of thinking. A list of our ongoing and planned research work are as follows:

Our analysis of primordial non-Gaussianity lacks in the analysis of instrumental systematics. Hence we plan to analyze the `CMB` polarization including the instrumental systematics and its effect on our results. Then we plan to analyze the local type non-Gaussianity in the observational data by using all the different fields, namely temperature, E mode, I_P and Q/U, in conjunction. Further, the primordial tensor perturbations can also have non-Gaussian features which will leave an imprint on the B mode field. We plan to extend our study to the non-Gaussian features in the tensor perturbed B mode field.

For the analysis of `CMB` fields using `TMF`s, it is desirable to compute α and β directly on the sphere. Hence, we have generalized the definition of translation-invariant `TMF`s, specifically $W_2^{1,1}$ and $W_2^{0,2}$, to the curved 2-dimensional surface of a sphere. Then these translation-invariant `TMF`s for a general field on a sphere are obtained in terms of the covariant derivatives of the field. Further, analytic expression for the case of isotropic Gaussian and isotropic Rayleigh distributed field was also obtained. In the analysis of `CMB` so far with $W_2^{1,1}$, we had ignored the B mode field originating from the primordial tensor perturbation and gravitational lensing due to the large scale structure. The gravitational lensing will affect the anisotropy in the shape of the structures in the B mode field. Hence we plan to use α and β to study this effect and analyze its usefulness to

distinguish the primordial origin from the gravitational lensing in the B mode field. Further, we plan to study the non-Gaussianity of CMB fields by incorporating not just α and β but also all the components of the tensor $W_2^{1,1}$. The morphological features due to the physical mechanisms during the very early Universe is dominant at angular scales larger than 1°. Therefore, we plan to use this idea to study the prospect of using the TMFs of CMB fields to distinguish morphological features of primordial origin from the late time effects. We also plan to do a detailed study of the effect of different cosmological parameters on the TMFs of the CMB fields. This will result in a better understanding about its sensitivity for different factors and will help us to develop methods for its efficient application to the CMB analysis.

The TMFs are general statistical tool and can be applied to any random field on two or more dimensional space. Our analysis using the TMFs for a 2-dimensional space can be extended for the study of 21cm emissions from the epoch of reionization by using the 2-dimensional redshift slices, which can then be used to probe different models of reionization. Further, we plan to extend the analysis with TMFs to 3-dimensional data [133], in order to constrain cosmological models with 21cm data from future radio interferometers and large scale structure data.

Bibliography

[1] H. Bondi, T. Gold "The Steady-State Theory of the Expanding Universe", Mon. Not. R. Astron. Soc. **108** 3 252-270 (1948).

[2] A. Freidmann, "On the Curvature of Space", Z. Phys. **10** 377 (1922).

[3] E. Hubble, "A Relation Between Distance And Radial Velocity Among Extra-Galactic Nebulae", PNAS **15** 3 168-173 (1929).

[4] G. Gamow, "The Evolution of the Universe", Nature **162** 4122 680-682 (1948).

[5] R. A. Alpher and R. Hermann, "Evolution of the Universe", Nature **162** 4124 774-775 (1948).

[6] R. A. Alpher and R. C. Hermann, "Remarks on the Evolution of the Expanding Universe", Phys. Rev. **75** 1089-1095 (1949).

[7] A. A. Penzias and R. W. Wilson, "A Measurement of Excess Antenna Temperature at 4080 Mc/s", Astrophys. J. **142** 419-421 (1965).

[8] R. Dicke *et al.*, "Cosmic Black-Body Radiation", Astrophys. J. **142** 414-419 (1965).

[9] R. V. Wagoner *et al.*, "On the Synthesis of Elements at Very High Temperatures", Astrophys. J. **148** 3 (1967).

[10] G. Steigman, "Primordial Nucleosynthesis in the Precision Cosmology Era", Annu. Rev. Nucl. Part. Sci. **57** 463 (2007).

[11] D. Larson *et al.*, "Seven-year Wilkinson Microwave Anisotropy Probe (WMAP) Observations:Power Spectra and WMAP-derived Parameters", Astrophys. J., Suppl. Ser. **192** 2 16 (2011).

[12] R. H. Cyburt *et al.*, " Primordial Nucleosynthesis in light of WMAP", Phys. Lett. B. **567** 227 (2003).

[13] R. H. Cyburt, "Primordial Nucleosynthesis for the New Cosmology: Determining Uncertainties and Examining Concordance", Phys. Rev. D. **70** 023505 (2004).

[14] A. Coc *et al.*, "Updated Big Bang Nucleosynthesis Compared with Wilkinson Microwave Anisotropy Probe Observations and the Abundance of Light Elements", Astrophys. J. **600** 544 (2004), arXiv:astro-ph/0309480.

[15] A. Cuoco *et al.*, "Present status of primordial nucleosynthesis after WMAP: results from a new BBN code", Int. J. Mod. Phys. A **19** 4431 (2004), arXiv:astro-ph/0307213.

[16] A. H. Guth, "The Inflationary Universe: A Possible Solution to the Horizon and Flatness Problems", Phys. Rev. D **23** 347 (1981).

[17] A. A. Starobinsky, "Spectrum of relict gravitational radiation and the early state of the universe", Pis'ma Zh. Eksp. Teor. Fiz. **30** 719 (1979) [JETP Lett. **30** 11 682 (1979)].

[18] A. A. Starobinsky, "Dynamics of phase transition in the new inflationary universe scenario and generation of perturbations", Phys. Lett. B **117** 3-4 175 (1982).

[19] A. D. Linde, "A new inflationary universe scenario: A possible solution of the horizon, flatness, homogeneity, isotropy and primordial monopole problems", Phys. Lett. B **108** 6 389 (1982).

[20] A. Albrecht and P. J. Steinhardt, "Cosmology for Grand Unified Theories with Radiatively Induced Symmetry Breaking", Phys. Rev. Lett. **48** 17 1220 (1982).

[21] D. Fixsen *et al.*, "The Cosmic Microwave Background Spectrum from the Full COBE/FIRAS Data Set", Astrophys. J. **473** 576 (1996), arXiv:astro-ph/9605054.

[22] Smoot G F *et al.*, "Structure in the COBE differential microwave radiometer first-year maps", Astrophys. J. **396** L1L5 (1992).

[23] T. J. Sodroski *et al.*, "Large-scale characteristics of interstellar dust from COBE DIRBE observations", Astrophys. J. **428** 2 638 (1994).

[24] J. Kovac *et al.*, "Detection of polarization in the cosmic microwave background using DASI", Nature **420** 772 (2002), arXiv:astro-ph/0209478.

[25] E. M. Leitch *et al.*, "Experiment Design and First Season Observations with the Degree Angular Scale Interferometer", Astrophys. J. **568** 28 (2002), arXiv:astro-ph/0104488.

[26] N. W. Halverson *et al.*, "DASI First Results: A Measurement of the Cosmic Microwave Background Angular Power Spectrum", Astrophys. J. **568** 38 (2002), arXiv:astro-ph/0104489.

[27] C. Pryke *et al.*, "Cosmological Parameter Extraction from the First Season of Observations with DASI", Astrophys. J. **568** 46 (2002), arXiv:astro-ph/0104490.

[28] A. Miller *et al.*, "The QMAP and MAT/TOCO Experiments for Measuring Anisotropy in the Cosmic Microwave Background", Astrophys. J., Suppl. Ser. **140** 115 (2002), arXiv:astro-ph/0108030.

[29] C. B. Netterfield *et al.*, "Angular Power Spectrum of the Cosmic Microwave Background", Astrophys. J. **571** 2 604 (2002).

[30] S. Padin *et al.*, "First intrinsic anisotropy observations with the Cosmic Background Imager", Astrophys. J. **549** 1 L1-L5.

[31] A. C. S. Readhead *et al.*, "Polarization observations with the Cosmic Background Imager ", Science **306** 5697 836 (2004).

[32] D. Hanson *et al.*, "Detection of B-mode Polarization in the Cosmic Microwave Background with Data from the South Pole Telescope", Phys. Rev. Lett. **111** 141301 (2013), arXiv:1307.5830.

[33] P. A. R. Ade *et al.* [Polarbear Collaboration], "A Measurement of the Cosmic Microwave Background B-mode Polarization Power Spectrum

at Sub-Degree Scales with Polarbear", Astrophys. J. **794** 171 (2014), arXiv:1403.2369v2.

[34] P. A. R. Ade *et al.* [Planck Collaboration], "Planck 2015 results. XV. Gravitational lensing", Astron. Astrophys. **594** A15 (2016), arXiv:1502.01591v3.

[35] P. A. R. Ade *et al.*, "BICEP2 / Keck Array VIII: Measurement of gravitational lensing from large-scale B-mode polarization", Astrophys. J. **833** 2 (2016), arXiv:1606.01968v2.

[36] C. L. Bennett *et al.*, "First-Year Wilkinson Microwave Anisotropy Probe (WMAP) Observations: Preliminary Maps and Basic Results", Astrophys. J. Suppl. Ser. **148** 1 (2003).

[37] P. A. R. Ade *et al.* [Planck Collaboration], "Planck 2013 results. XII. Diffuse component separation", Astronom. and Astrophys. **571** A12 31 (2014).

[38] P. A. R. Ade *et al.* [Planck Collaboration], "Planck 2015 results. XVI. Isotropy and statistics of the CMB", Astronom. and Astrophys. **594** A16 (2016), arXiv:1506.07135.

[39] M. J. Rees, "Polarization and Spectrum of the Primeval Radiation in an Anisotropic Universe", Astrophys. J. **153** L1 (1968).

[40] J.R. Bond and G. Efstathiou, "The statistics of cosmic background radiation fluctuations", Mon. Not. Roy. Astron. Soc. **226** 655 (1987).

[41] R. Crittenden, R.L. Davis and P.J. Steinhardt, "Polarization of the microwave background due to primordial gravitational waves", Astrophys. J. **417** L13 (1993), astro-ph/9306027.

[42] R.A. Frewin, A.G. Polnarev and P. Coles, "Gravitational waves and the polarization of the cosmic microwave background", Mon. Not. Roy. Astron. Soc. **266** L21 (1994), astro-ph/9310045.

[43] D. Coulson, R.G. Crittenden and N.G. Turok, "Polarization and anisotropy of the microwave sky", Phys. Rev. Lett. **73** 2390 (1994), astro-ph/9406046.

[44] R.G. Crittenden, D. Coulson and N.G. Turok, "Temperature-polarization correlations from tensor fluctuations", Phys. Rev. D **52** 5402 (1995), astro-ph/9411107.

[45] G. P. Nanos Jr., "Polarization of the blackbody radiation at 3.2 centimeters", Astrophys. J. **232** 341 (1979).

[46] N. Caderni *et al.*, "Polarization of the microwave background radiation. I - Anisotropic cosmological expansion and evolution of the polarization states. II - an infrared survey of the sky", Phys. Rev. D **17** 1901 (1978).

[47] P. M. Lubin and G. F. Smoot, "Polarization of the cosmic background radiation", Astrophys. J. **245** 1 (1981).

[48] E. J. Wollack *et al.*, "A Measurement of the Anisotropy in the Cosmic Microwave Background Radiation at Degree Angular Scales", Astrophys. J. **419** L49 (1993).

[49] C. B. Netterfield *et al.*, "A Measurement of the Angular Power Spectrum of the Anisotropy in the Cosmic Microwave Background", Astrophys. J. **474** 1 47 (1997).

[50] A. de Oliveira-Costa *et al.*, "Large-scale polarization of the microwave background and foreground", Phys. Rev. D **68** 8 083003 (2003), arXiv:astro-ph/0212419.

[51] P. A. R. Ade *et al.* [Planck Collaboration], "Planck 2015 results. XIII. Cosmological parameters", Astronom. and Astrophys. **594** A13 (2016), arXiv:1502.01589.

[52] P. A. R. Ade *et al.*, "BICEP2 I: Detection of B-mode Polarization at Degree Angular Scales", Phys. Rev. Lett. **112** 241101 (2014), arXiv:1403.3985v3.

[53] P. A. R. Ade *et al.*, "A Joint Analysis of BICEP2/Keck Array and Planck Data", Phys. Rev. Lett. **114** 101301 (2015), arXiv:1502.00612.

[54] J. R. Gott III, M. Dickinson and A. L. Melott, "The sponge-like topology of large-scale structure in the universe", Astrophys. J. **306** 341 (1986).

[55] J.R. Gott *et al.*, "Topology of microwave background fluctuations-theory", Astrophys. J. **352** 1 (1990).

[56] M. S. Vogeley *et al.*, "Topological analysis of the CfA redshift survey", Astrophys. J. **420** 525 (1994).

[57] A. Canavezes *et al.*, "The topology of the IRAS Point Source Catalogue Redshift Survey", Mon. Not. Roy. Astron. Soc. **297** 3 777 (1998), arXiv:astro-ph/9712228.

[58] C. Hikage *et al.*, "Minkowski Functionals of SDSS Galaxies I: Analysis of Excursion Sets", Publ. Astron. Soc. Jap. **55** 911 (2003), arXiv:astro-ph/0304455.

[59] C. Park *et al.*, "Topology Analysis of the Sloan Digital Sky Survey. I. Scale and Luminosity Dependence", Astrophys. J. **633** 11 (2005), arXiv:astro-ph/0507059.

[60] K. R. Mecke, T. Buchert and H. Wagner, "Robust morphological measures for large-scale structure in the Universe", Astron. Astrophys. **288** 697 (1994), arXiv:astro-ph/9312028.

[61] M. Kerscher *et al.*, "Minkowski Functionals of Abell/ACO Clusters", Mon. Not. Roy. Astron. Soc. **284** 73 (1997), arXiv:astro-ph/9606133.

[62] J. Schmalzing and T. Buchert, "Beyond genus statistics: a unifying approach to the morphology of cosmic structure", Astrophys. J. **482** L1-L4 (1997), arXiv:astro-ph/9702130.

[63] M. Kerscher, J. Schmalzing, T. Buchert and H. Wagner, "Fluctuations in the IRAS 1.2Jy Catalogue", Astron. Astrophys. **333** 1 (1998), arXiv:astro-ph/9704028.

[64] L. A. Santaló, "Integral geometry and geometric probability", Addison-Wesley, Reading, MA (1976).

[65] J. Schmalzing and K. M. Gorski, "Minkowski functionals used in the morphological analysis of cosmic microwave background anistropy maps", Mon. Not. Roy. Astron. Soc. **297** 355 (1998), arXiv:astro-ph/9710185.

[66] S. Winitzki and A. Kosowsky, "Minkowski functional description of microwave background Gaussianity", New Astron. **3** 75 (1998), arXiv:astro-ph/9710164.

[67] T. Matsubara, "Statistics of smoothed cosmic fields in perturbation theory. I. Formulation and useful formulae in second-order perturbation theory", Astrophys. J. **584** 1 (2003), arXiv:astro-ph/0006269.

[68] C. Hikage, E. Komatsu and T. Matsubara, "Primordial non-Gaussianity and analytical formula for Minkowski functionals of the cosmic microwave background and large-scale structure", Astrophys. J. **653** 11 (2006), arXiv:astro-ph/0607284.

[69] T. Matsubara, "Analytic Minkowski Functionals of the Cosmic Microwave Background: Second-order Non-Gaussianity with Bispectrum and Trispectrum", Phys. Rev. D **81** 083505 (2010), arXiv:1001.2321.

[70] D. Novikov, J. Schmalzing and V. F. Mukhanov, "On Non-Gaussianity in the Cosmic Microwave Background", Astron. Astrophys. **364** 17 (2000), arXiv:astro-ph/0006097v3.

[71] J. H. P. Wu *et al.*, "Tests for Gaussianity of the MAXIMA-1 CMB Map", Phys. Rev. Lett. **87** 251303 (2001), arXiv:astro-ph/0104248v1.

[72] S. F. Shandarin, H. A. Feldman, Y. Xu and M. Tegmark, "Morphological Measures of non-Gaussianity in CMB Maps", Astrophys. J. Suppl. Ser. **141** 1 (2002), arXiv:astro-ph/0107136v2.

[73] C. Hikage *et al.*, "Limits on primordial non-Gaussianity from Minkowski Functionals of the WMAP temperature anisotropies", Mon. Not. Roy. Astron. Soc. **389** 1439 (2008), arXiv:0802.3677.

[74] P. Natoli *et al.*, "Boomerang Constraints on Primordial non-Gaussianity from analytical Minkowski Functionals", Mon. Not. Roy. Astron. Soc. **408** 1658 (2010), arXiv:0905.4301v1.

[75] P.A.R. Ade *et al.* [Planck collaboration], "Planck 2013 Results. XXIV. Constraints on primordial non-Gaussianity", Astron. Astrophys. **571** A24 (2014), arXiv:1303.5084.

[76] P. A. R. Ade *et al.* [Planck Collaboration], "Planck 2015 results. XVII. Constraints on primordial non-Gaussianity", Astronom. and Astrophys. **594** A17 (2016), arXiv:1502.01592

[77] P. Chingangbam and C. Park, "Residual foreground contamination in the WMAP data and bias in non-Gaussianity estimation", JCAP *02* 031 (2013), arXiv:1210.2250.

[78] L. Santos, K. Wang and W. Zhao, "Probing the statistical properties of CMB B-mode polarization through Minkowski functionals", JCAP *07* 029 (2016), arXiv:1510.07779.

[79] W. Zhao, "Probing CMB cold spot through local Minkowski functionals", Res. Astron. Astrophys. **14** 625 (2014), arXiv:1209.4021.

[80] D. Munshi *et al.*, "Lensing-induced morphology changes in CMB temperature maps in modified gravity theories", JCAP **04** 056 (2016), arXiv:1602.00965v1.

[81] van de Weygaert R. *et al.*, "Alpha, Betti and the Megaparsec Universe: On the Topology of the Cosmic Web", Transactions on Computationals Science XIV **60**, arXiv:1206.3640.

[82] T. Sousbie, "The persistent cosmic web and its filamentary structure I: Theory and implementation", Mon. Not. Roy. Astron. Soc. **414** 1 350 (2011), arXiv:1009.4015.

[83] T. Sousbie, "The persistent cosmic web and its filamentary structure II: Illustrations", Mon. Not. Roy. Astron. Soc. **414** 1 384 (2011), arXiv:1009.4014.

[84] P. Chingangbam *et al.*, "Hot and cold spot counts as probes of non-Gaussianity in the cosmic microwave background", Astrophys. J. **755** 122 (2012), arXiv:1206.0436.

[85] C. Park et al., "Betti numbers of Gaussian fields", JKAS **46** 125 (2013), arXiv:1307.2384.

[86] S. Alesker, "Description of continuous isometry covariant valuations on convex sets", Geom. Dedicata **74** 241-248 (1999).

[87] D. Hug, R. Schneider and R. Schuster, "The space of isometry covariant tensor valuations", St. Petersburg Math. J. **19** 137-158 (2008).

[88] C. Beisbart, M. S. Barbosa, H. Wagner and L. da F. Costa, "Extended morphometric analysis of neuronal cells with Minkowski valuations", Eur. Phys. J. B **52** 531-546, arXiv:cond-mat/0507648.

[89] G. Durand, F. Graner and J. Weiss, "Deformation of grain boundaries in polar ice", Europhy. Lett. **67** 1038-1044, arXiv:cond-mat/0309081.

[90] C. Beisbart, R. Dahlke, K. Mecke and H. Wagner, "Vector- and tensor-valued descriptors for spacial patterns", Morphology of Condensed Matter - Physics and Geometry of Spatially Complex Systems (ed. by K. Meche and D. Stoyan) **600** 249-271, arXiv:physics/0203072.

[91] A. Lewis A. Challinor and A. Lasenby, "Efficient Computation of Cosmic Microwave Background Anisotropies in Closed Friedmann-Robertson-Walker Models", Astrophys. J. **538** 473 (2000), arXiv:astro-ph/9911177.

[92] J. M. Bardeen, P. J. Steinhardt and M. S. Turner, "Spontaneous creation of almost scale-free density perturbations in an inflationary universe", Phys. Rev. D **28** 679 (1983).

[93] A. Linde, "Chaotic inflation", Phys. Lett. B **129** 177 (1983).

[94] V. F. Mukhanov, H. A. Feldman and R. H. Brandenberger, "Theory of cosmological perturbations", Phys. Rep. **215** 203 (1992).

[95] H. V. Peiris *et al.*, "First Year Wilkinson Microwave Anisotropy Probe (WMAP) Observations: Implications for Inflation", Astrophys. J. Suppl. **148** 213 (2003), arXiv:astro-ph/0302225.

[96] P. A. R. Ade *et al.* [Planck Collaboration], "Planck 2015 results. XX. Constraints on inflation", Astronom. and Astrophys. **594** A20 (2016), arXiv:1502.02114.

[97] K. Enqvist and M. S. Sloth, "Adiabatic CMB perturbations in pre-Big-Bang string cosmology", Nucl. Phys. B **626** 395 (2002), arXiv:hep-ph/0109214.

[98] D. H. Lyth, C. Ungarelli and D. Wands, "Primordial density perturbation in the curvaton scenario", Phys. Rev. D **67** 023503 (2003), arXiv:astro-ph/0208055.

[99] J. L. Lehners and P. J. Steinhardt, "Non-Gaussian density fluctuations from entropically generated curvature perturbations in ekpyrotic models", Phys. Rev. D **77** 063533 (2008), arXiv:0712.3779.

[100] D.S. Salopek and J.R. Bond, "Nonlinear evolution of long wavelength metric fluctuations in inflationary models", Phys. Rev. D **42** (1990) 3936.

[101] T. Falk, R. Rangarajan and M. Srednicki, "The angular dependence of the three point correlation function of the cosmic microwave background radiation as predicted by inflationary cosmologies", Astrophys. J. **403** (1993) L1, astro-ph/9208001.

[102] V. Acquaviva, N. Bartolo, S. Matarrese and A. Riotto, "Second order cosmological perturbations from inflation", Nucl. Phys. B **667** (2003) 119, astro-ph/0209156.

[103] J. M. Maldacena, "Non-Gaussian features of primordial fluctuations in single field inflationary models", JHEP **05** (2003) 013, astro-ph/0210603.

[104] M. Liguori, S. Matarrese, and L. Moscardini, "High-Resolution Simulations of Non-Gaussian Cosmic Microwave Background Maps in Spherical Coordinate", Astophys. J. **597** 1 p57 (2003), arXiv:astro-ph/0306248.

[105] P. Chingangbam, and C. Park, "Statistical nature of non-Gaussianity from cubic order primordial perturbations: CMB map simulations and genus statistic", J. Cosmol. Astropart. Phys. **0912** 019 (2009), arXiv:0908.1696.

[106] F. Elsner and B. D. Wandelt, "Improved simulation of non-Gaussian temperature and polarization CMB maps", Astophys. J. Suppl. **184** 264 (2009), arXiv:0909.0009.

[107] K. M. Gorski *et al.*, "HEALPix: A Framework for High-Resolution Discretization, and Fast Analysis of Data Distributed on the Sphere", Astrophys. J. **622**, 759 (2005), arXiv:astro-ph/0409513.

[108] C. Hikage and T. Matsubara, "Limits on Second-Order Non-Gaussianity from Minkowski Functionals of WMAP Data", Mon. Not. Roy. Astron. Soc. **425** 2187 (2012), arXiv:1207.1183.

[109] E. Komatsu *et al.* [WMAP collaboration], "Seven-Year Wilkinson Microwave Anisotropy Probe (WMAP) Observations: Cosmological Interpretation", Astrophys. J. Suppl. **192** 18 (2011), arXiv:1001.4538.

[110] S. Galli *et al.*, "CMB polarization can constrain cosmology better than CMB temperature", Phys. Rev. D. **90** 063504 (2014), arXiv:1403.5271.

[111] P. A. R. Ade *et al.* [Planck Collaboration], "Planck 2013 results. XVI. Cosmological parameters", Astronom. and Astrophys. **571** A16 (2014), arXiv:1303.5076.

[112] L. Euler, "Solutio problematis ad geometriam situs pertinentis", Commentarii academiae scientiarum Petropolitanae **8** 128-140 (1741).

[113] H. Hadwiger, "Vorlesungen ber Inhalt, Oberflche und Isoperimetrie", Springer Verlag, Berlin (1957).

[114] B. Chen, "A Simplified Elementary Proof of Hadwigers Volume Theorem", Geometriae Dedicata **105** 1 107 (2004).

[115] A. G. Doroshkevich, "Spatial structure of perturbations and origin of galactic rotation in fluctuation theory", Astrophysics **6** 4 p320 (1970).

[116] R. J. Adler, "The Geometry of Random Fields", SIAM ed. (1981).

[117] H. Tomita, "Curvature invariants of random interface generated by Gaussian fields", Prog. Theor. Phys. **76** 952 (1986).

[118] E. A. Lim and D. Simon, "Can we detect hot or cold spots in the CMB with Minkowski Functionals?", J. Cosmol. Astropart. Phys. **1** 48 (2012), arXiv:1103.4300.

[119] C. Gay, C. Pichon and D. Pogosyan, "Non-Gaussian statistics of critical sets in 2 and 3D: Peaks, voids, saddles, genus and skeleton", Phys. Rev. D. **85** 023011 (2012), arXiv:1110.0261.

[120] A. Ducout *et al.*, "Non Gaussianity and Minkowski Functionals: forecasts for Planck", Mon. Not. Roy. Astron. Soc. **429** 2104 (2013), arXiv:1209.1223.

[121] H. Müller, "Über Momente ersten und zweiten Grades in der Integralgeometrie", Rend. Circ. Palermo (II. Ser.) **2** 119-140 (1953).

[122] P. McMullen, "Isometry covariant valuations on convex bodies", Rend. Circ. Palermo. **50** 259-271 (1997).

[123] G.E. Schröder-Turk *et al.*, "Tensorial Minkowski functionals and anisotropy measures for planar patterns", J. Microsc. **238** 57 (2010).

[124] C. G. Park and C. Park, "Simulation of Cosmic Microwave Background Polarization fields for AMiBA experiment", J. Korean. Astrophs. Soc. **35** 67 (2002), arXiv:astro-ph/0203322.

[125] P. D. Naselsky and D. I. Novikov, "General Statistical properties of the CMB polarization field", Astrophys. J. **507** 31 (1998), arXiv:astro-ph/9801285.

[126] A. D. Dolgov, A. G. Doroshkevich, D. I. Novikov and I. D. Novikov, "Geometry and statistics of cosmic microwave polarization", Int. J. Mod. Phys. D **8** 189 (1999), arXiv:astro-ph/9901399.

[127] D. Huterer and T. Vachaspati, "Distribution of singularities in the cosmic microwave background polarization", Phys. Rev. D **72** 043004 (2005), arXiv:astro-ph/0405474.

[128] P. A. R. Ade *et al.* [Planck Collaboration], "Planck 2015 results. XII. Full Focal Plane simulations", Astronom. and Astrophys. **594** A12 (2016), arXiv:1509.06348.

[129] R. Adam *et al.* [Planck Collaboration], "Planck 2015 results. IX. Diffuse component separation: CMB maps", Astronom. and Astrophys. **594** A9 (2016), arXiv:1502.05956.

[130] V. G. Gurzadyan *et al.*, "Ellipticity analysis of the BOOMERanG CMB maps", Int. J. Mod. Phys. **D12** 1859 (2003), arXiv:astro-ph/0210021v3.

[131] V. G. Gurzadyan *et al.*, "Elliptic CMB Sky", Mod. Phys. Lett. **A20** 813 (2005), arXiv:astro-ph/0503103v2.

[132] E. Berntsen and F. K. Hansen, "Excess ellipticity of hot and cold spots in the WMAP data?", Astrophys. J. **779** 1 (2013), arXiv:1211.5275v1.

[133] G.E. Schröder-Turk *et al.*, "Minkowski Tensors of Anisotropic Spatial Structure", New J. Phys. **15** 083028 (2013), arXiv:1009.2340.